

In Search of Mg Battery Cathode Materials – A Migration Energy High-throughput Screening Machinery

by
Ziqin Rong

Submitted to the Department of Materials Science and Engineering in Partial Fulfillment of the Requirements for the Degree of Ph.D. in Materials Science and Engineering


at the
Massachusetts Institute of Technology

September 2017

© 2017 Massachusetts Institute of Technology. All Rights Reserved

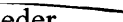
Signature of
Author.....

Signature redacted

 Ziqin Rong
Department of Materials Science and Engineering
May 19, 2017

Certified
by

Signature redacted

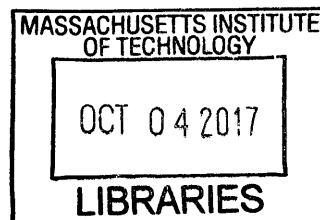

Gerbrand Ceder
Visiting Professor of Materials Science and Engineering
Thesis Supervisor

Accepted
by

Signature redacted


Donald Sadoway
Professor of Materials Science and Engineering
Chair, Materials Science & Engineering Committee on Graduate Studies

ARCHIVES



In Search of Mg Battery Cathode Materials – A Migration Energy High-throughput Screening Machinery

by
Ziqin Rong

Submitted to the Department of Materials Science and Engineering and in Partial
Fulfillment of the Requirement for the Degree of
Ph.D. in Materials Science and Engineering

Abstract:

In this thesis, we demonstrate the results and progress of developing a high-throughput migration energy calculation machinery and applying it in search for Mg battery cathode materials. We discuss the key challenge of developing functional Mg battery cathode, and propose to use NEB algorithm in high-throughput calculations to screen for materials with good Mg^{2+} diffusivity. However, though NEB algorithm performs quite well on individual systems, due to its very long run-time, it is difficult to be scaled up in high-throughput applications. Therefore, new algorithms are developed and implanted, and 17 potential Mg cathode materials are selected by the new high-throughput system. The main contributions of this thesis are: (1) developed new algorithms for NEB calculations in high-throughput environments; (2) implemented a functional software system for conducting high-throughput migration energy calculations, which can be further applied in other research areas like Ca batteries, Zn batteries, solid state conductors, etc.; (3) proposed new Mg cathode materials.

Acknowledgements

I would like to acknowledge and thank my advisor, Prof. Gerbrand Ceder. He offered me with the opportunity and support for a fantastic project. I have learned so much from discussing science with him.

I also want to give my deep appreciation for Prof. Patrick Winston in CSAIL. He was my Master degree supervisor at MIT CSAIL and taught me a lot of knowledge in algorithms and software system design, which is later applied to this project.

I want to thank my collaborator Daniil Kitchaev. His work in PathFinder algorithm is the foundation of the ApproxNEB method. I would also like to thank my lab mates Wenxuan Huang, Miao Liu, Penghao Xiao, Daniel Hannah, Rahul Malik and Piero Canepa, who have leveraged their individual expertise to help develop the theory part of this thesis.

Anubhav Jain from LBNL has been a constant source of generous help in implementing the high-throughput ApproxNEB system with Fireworks system, to which I own great gratitude.

Last but not least, I want thank my parents and my girlfriend Xinyi, for their support, love and everything.

Contents

Acknowledgements.....	3
Chapter 1 Introduction and Background	5
1.1 Why Multi-valent batteries	5
1.2 Mg rechargeable batteries and its challenges.....	8
1.3 Status-of-quo on Mg cathodes: Chevrel Phases and Thiospinel.....	12
1.4 High-throughput Calculations.....	23
Chapter 2 Methodology	24
2.1 Migration State Calculation	24
2.2 Threshold for Cation Mobility in MV Cathode	25
2.3 NEB method.....	26
Chapter 3 – Spinel Compounds as Multi-valent Battery Cathodes	29
3.1 Motivation for Looking into Spinel Structures	29
3.2 Computational Methods	31
3.3 Voltages, Capacities, Stabilities, Safety and Diffusivities	34
3.3 Discussion	46
Chapter 4. Evaluation of sulfur spinel compounds for multivalent battery cathode applications	49
4.1 Motivation	49
4.2 Structure, Voltages, Capacities, NEBs, etc.	51
4.3 Discussion	60
Chapter 5 Materials Design Rules for Multivalent Ion Mobility in Intercalation Structures	65
5.1 Motivation	65
5.2 Discussions.....	66
Chapter 6. High-throughput NEB	77
6.1 Framework	77
5.2 Obstacles	80
Chapter 7. PathFinder and ApproxNEB Algorithms	81
7.1 Methods.....	81
7.2 Error Metric Definition	84
7.3 PathFinder v.s. Linear Interpolation on Error Metric.....	85
7.4 PathFinder v.s. Linear Interpolation on Computational Resource Cost.....	87
7.5 PathFinder v.s. Linear Interpolation on CaMoO ₃ example.....	88
7.6 ApproxNEB Method	89

7.7 ApproxNEB v.s. NEB on Barrier Estimation	91
7.8 ApproxNEB v.s. NEB on Computational Resource Cost	92
7.9 ApproxNEB Implementation	94
Chapter 8 High-throughput ApproxNEB and results.....	95
8.1 Error Handling.....	95
8.2 EndPointFinder	97
8.3 Data Generation.....	101
8.4 Workflow	103
8.5 Code Implementation and Dependencies.....	107
8.6 Data Structure.....	107
8.7 Results	108
8.8 Recheck Coordination Number Rules.....	110
8.9 HT ApproxNEB errors.....	112
Chapter 9 Case Study: Fast Mg ²⁺ Diffusion in Mo ₃ (PO ₄) ₃ O for Mg Batteries	113
9.1 Voltages and Diffusivity, etc.....	114
9.2 Verification of the Migration Barrier	118
Conclusion	121
Reference	121

Chapter 1 Introduction and Background

1.1 Why Multi-valent batteries

Secondary (i.e., rechargeable) intercalation batteries convert chemical energy into electricity via three main components: the cathode where the working ion is inserted/extracted, an electrolyte transporting working ions between anode and cathode, and the anode. During the battery discharge, working ions are released at the anode and migrate to the cathode through the electrolyte, producing an electrical current in the external circuit to power a load. The battery recharges by applying an external electrical

potential. Figure 1 depicts a schematic representation of these three components in the current and longstanding industry workhorse^{1,2}, i.e., Li-ion batteries.

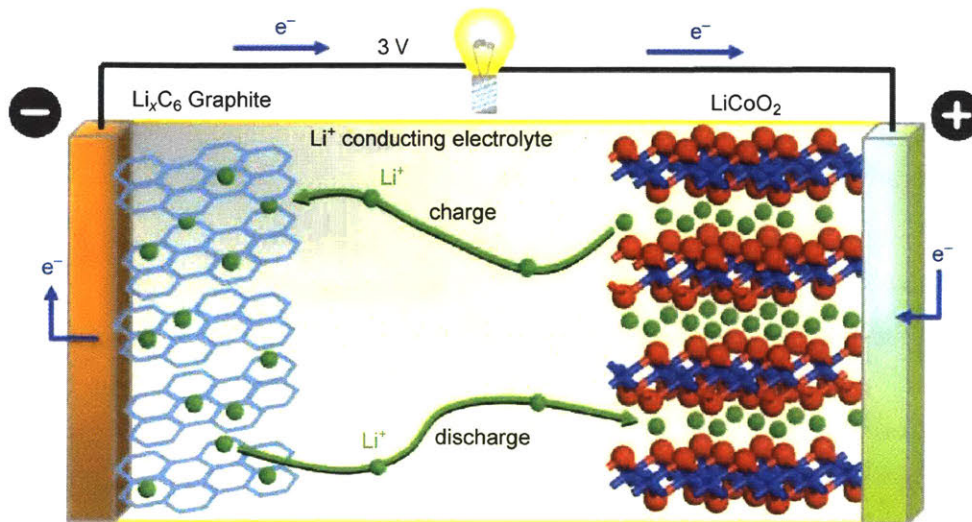


Fig. 1 Representative schematic of a discharging Lithium-ion battery utilizing a Li graphite anode, electrolyte, and an intercalation LiCoO_2 cathode.

While early battery technology used aqueous electrolytes, Li-technology with non-aqueous electrolytes has now largely outpaced (in terms of market share) all aqueous chemistries except for Pb-acid. After the rapid expansion of Li-ion in the portable electronics industry over the past decade, Li-ion batteries have now made commercial deployment of electric vehicles (EV) an imminent reality. Since 2007, leading manufacturers have achieved ~8% annual reduction in pack level costs, reaching approximately US \$300/kWh in 2014.³ The source of these cost reductions is primarily attributed to the economies of scale associated with increased production volumes and engineering advances at the cell and pack scale.^{3,4}

The cost of input materials contributes significantly to the overall total, and to continue the path toward cost parity with conventional gasoline powered vehicles, scientists⁵ and industrialists⁶ alike concede non-incremental improvements in battery technology must be made at the active material level, specifically by developing electrode chemistries that can support both increased gravimetric and volumetric energy densities while maintaining (and improving) the safety, power, lifetime, and cost of state-of-the-art Li-ion batteries. Since advancements at the materials level are approaching a fundamental limit in Li-ion batteries,^{1, 5-7} achieving even higher energy densities has spurred on investigation into the so-called “beyond Li-ion” technologies, such as Li-O₂ and Li-S.⁸⁻¹²

The most appealing “beyond Li-ion” technology for EVs (and portable electronics) will not only offer a significant energy density improvement and cost reduction but will also be compatible with existing, highly optimized Li-ion battery architecture (and fabrication) to take advantage of the knowledge accrued over the past 20 years of Li-ion battery manufacturing. From this perspective, intercalation batteries based on new multivalent (MV) chemistries, such as Mg²⁺, Ca²⁺, Zn²⁺, etc., are especially interesting because they have the potential to meet the aforementioned criteria. While current commercial Li-ion batteries operate with a graphitic anode and an intercalation transition-metal oxide cathode separated by a non-aqueous electrolyte, an analogous MV cell can be envisioned with each component now based on a MV chemistry. MV batteries will be able to electrochemically store energy through its three main components: the intercalation cathode where MV ions are inserted/extracted, a metal anode (e.g., Mg), and an electrolyte transporting MV-ions between anode and cathode.

A MV chemistry can offer significant improvement in volumetric energy density simply by using a metallic anode (~ 3833 mAh/cm³ theoretical volumetric energy density for Mg compared to ~ 2046 mAh/cm³ for Li metal). This is feasible because early evidence indicates that the metallic form of common MV intercalation ions (Mg, Ca) deposits more uniformly than metallic Li during electrochemical cycling.¹³⁻¹⁶ The surface area of lithium metal anodes grows substantially upon cycling, leading to an increase in the surface reactions with the electrolyte. The instability of this surface layer with increased temperature, accelerates thermal runaway, and can even lead to fire.^{15, 17-19} While Li metal anodes are frequently used in lab-made Li-cell prototypes, they so far have been practically unusable in commercial batteries because of lack of cycle life and safety concerns. As a result, current Li-ion batteries operate with lower volumetric energy density graphite anodes (~ 800 mAh/cm³). Several attempts at development and commercialization of full electrochemical cells with lithium metal as the anode and a liquid electrolyte have often led to disastrous results.^{15, 17-19}

1.2 Mg rechargeable batteries and its challenges

Although MV cells can potentially achieve high-energy densities using metallic anodes,¹³⁻¹⁶ discovering electrolytes capable of reversible MV metal plating/stripping at the anode and supporting reversible intercalation against a high voltage cathode remains a significant and fundamental scientific challenge. The development of versatile MV electrolytes has been curbed by a multitude of factors such as limited chemical and electrochemical compatibility with the electrodes (i.e., narrow electrochemical stability window), lack of reversible MV metal stripping and plating, instability against current

collectors, low MV (Mg) mobility leading to the formation of ionic couples (i.e., low MV transference number),²⁰ and low Coulombic Efficiency (CE). While a detailed analysis of the challenges and accomplishments associated with MV electrolyte development is beyond the scope of this thesis, several comprehensive reports exist in the literature^{14, 16, 21-46} and we summarize the major advancements in MV electrolytes below.

The peculiar electrochemistry of Mg imposes nontrivial limitations on electrolytes, such as being compatible with high-voltage cathode materials and simultaneously achieving reversible Mg deposition at the metal anode. Indeed, Mg electrolytes that are analogous to their Li-ion counterparts (e.g., LiPF₆ in PC/DMC solutions) tend to decompose irreversibly at the Mg metal, producing passivating layers resistant to Mg ion conduction.^{25, 47} However, Keyzer et al.⁴³ recently showed reversible Mg stripping and deposition at the metal anode using a solution of Mg(PF₆)₂·(CH₃CN)₆ in CH₃CN and CH₃CN/tetrahydrofuran (THF) mixtures, with conductivities up to 28 mS/cm and an anodic stability of ~4 V vs Mg on Al electrodes.

Historically, Gregory and collaborators⁴⁸ at Dow Chemical made a breakthrough in showing quasi-reversible Mg-plating from Grignard's reagents in 1990. It took more than ten years of methodical refinements by Aurbach and co-workers to increase the Coulombic efficiency as well as the anodic stability of the Grignard's electrolytes, leading to the ethereal solutions of organic magnesium aluminum chloride salts (or organomagnesium-chloride complexes), namely the "dichloro complex" DCC⁴⁹ and the "all phenyl complex" APC.^{21, 49} Subsequently, Doe²⁸ and collaborators at Pellion Technology studied the electrochemistry of a much simpler combination, the magnesium

aluminum chloride complex (MACC), formed from a mixture of AlCl_3 and MgCl_2 in ethereal solvents. The MACC electrolyte exhibits a similar anodic stability (~ 3.1 V) to its predecessors (i.e., DCC and APC) and with a high degree of reversible Mg deposition/stripping. In parallel, Kim and coworkers at Toyota R&D²⁴ developed a non-nucleophilic electrolyte, radically different from the chloride complexes, which was composed of a mixture of hexamethyldisilazide magnesium chloride (HMDSMgCl) and AlCl_3 and primarily targeted usage in high-energy density Mg–S batteries. Although the DCC, APC, and MACC electrolytes can be utilized in state-of-the-art Mg-battery prototypes,¹³ they are known to corrode various metals, including stainless steels and common current collectors.

The limitation of chloride electrolytes fueled interest in alternative chemistries. For example, Shao et al.⁵⁰ demonstrated reversible magnesium deposition from a diglyme solution of LiBH_4 and $\text{Mg}(\text{BH}_4)_2$, albeit with poor anodic stability (~ 1.8 V). Meanwhile, Mohtadi, Carter, Tutusaus, and co-workers at Toyota R&D discovered a series of promising halogen-free electrolytes,^{33, 51, 52} such as Mg boron-clusters and carboranes, which are less corrosive against current collectors and show the highest anodic-stability windows (~ 3.8 – 4.0 V) reported so far.²⁰ Also, the increasing attention for MV chemistries has stimulated research toward the search of electrolytes capable of reversible Ca-stripping and deposition.^{16, 53, 54}

While the last 20 years have witnessed an increasing focus in the development of new Mg electrolytes, the array of electrolytes compatible with high voltage Mg-cathodes is rather limited,^{14, 25, 38, 39} with researchers normally employing the usual suspects of

Mg(ClO₄)₂, Mg(NO₃)₂, or Mg(TFSI)₂ dissolved in acetonitrile (ACN), THF, or glymes (with water inclusion in a few cases). As such, experiments on high-voltage cathodes rely on complex 3-electrode setups that can separate the incompatible chemistries of Mg metal deposition (and stripping) and Mg intercalation in the cathode, leading to the lack of routine protocols to prepare Mg cells. Moreover, Lipson et al.²⁰ have clearly demonstrated that the anodic stability reported for some Mg electrolytes aforementioned largely depends on the nature of the working electrode, suggesting that particular care is required while performing and reporting new experiments. Additionally, the literature on the passivation of MV cathodes is particularly scarce,^{35, 55-57} despite a few studies attempting to unravel the complex interactions of Mg²⁺ and a few cathode materials with electrolyte salts and solvents,^{20, 31, 32, 46, 57-63} emphasizing the need for more systematic studies of the cathode-electrolyte interfacial processes.

In this thesis, we focus on understanding and charting the challenge posed by creating cathode host structures with sufficient MV cation mobility required for reversible intercalation at reasonable rates. Indeed, the expectation is that the higher charge of MV cations will polarize a host's environment, thereby reducing mobility and rate capability of MV chemistries. This is a very critical issue because with low mobility (we also use diffusivity in this thesis for the same meaning), even though we are able to identify a MV cathode material with high energy density, we will still be unable to charge or discharge the battery because the moving rates of cations in cathode are so low. While for Li⁺ intercalation both extensive experimental⁶⁴⁻⁶⁶ and theoretical⁶⁷⁻⁷² Li mobility data are readily available, the lack of reliable electrochemical MV test vehicles^{14, 25} and limited

exploration of MV chemistries have made it difficult to understand what controls MV ion mobility.

1.3 Status-of-quo on Mg cathodes: Chevrel Phases and Thiospinel

Although the concept of a rechargeable magnesium battery was proposed as early as 1990,⁴⁸ the first working demonstration of a prototype Mg full cell battery was achieved in 2000 by Aurbach et al.¹³ using a magnesium metal anode, an electrolyte based on a solution of Mg organo-halo-aluminate salts in tetrahydrofuran (THF), and a Chevrel $\text{Mg}_x\text{Mo}_6\text{S}_8$ cathode ($0 < x \leq 2$). With these innovations at the electrolyte and cathode, they were able to achieve ~ 1.4 V vs. Mg metal and ~ 80 mAh/g (128.8 mAh/g theoretical capacity), with good kinetics and cycle life (> 2000 cycles). On the process of discovering the Chevrel phase as a Mg intercalation host, we remarked that it was the result of “a lot of unsuccessful experiments of Mg ions insertion into well-known host for Li^+ ions insertion, as well as from the thorough literature analysis concerning the possibility of divalent ions intercalation into inorganic materials.”⁷³ Of note, batteries based on Chevrel compounds were proposed and demonstrated to function for Li-ion as early as 1985.⁷⁴

Unlike today’s commercialized Li-ion cathode materials, which are almost entirely structures with close-packed oxygen anion sub-lattices (e.g., layered, spinel, olivine), the Chevrel phase has a unique “cluster” structure shown below in Figure 2. The Chevrel structure is comprised of Mo_6T_8 (T = S, Se, Te) blocks (gray cubes in Figure 2a), with 6 Mo forming an octahedron on the faces and 8 T anions occupying the corners.^{75, 76} The Mo_6S_8 blocks are arranged such that they are separated by three types of “cavities” as illustrated

in Figure 2b, and the intercalation sites are contained within cavities of type 1 and 2. The site position within each cavity varies with cation species,⁷⁷ but for small ions (such as Li^+ , Mg^{2+} , or $\text{Cu}^{1+/2+}$ compared to Pb^{2+} or Sn^{2+}) there are multiple intercalation sites available within each cavity as shown in the inset of Figure 2b, with a ring of “inner sites” within cavity 1 and two “outer sites” in cavity 2. Considering the topology of Mo_6S_8 blocks, there are twelve possible sites (6 inner and 6 outer) between each block where the intercalating ion can reside as seen in Figure 2.⁷⁸ The Mo octahedral clusters exhibit metallic bonding and are each capable of accommodating a total of 4 electrons.⁷⁹ Accordingly, two Mg^{2+} ions can be inserted per Mo_6S_8 block with the first ion accommodated preferentially in the inner sites and the second in the outer sites. This is reflected in the voltage curve, voltage plateaus that occur at ~ 1.4 V and ~ 1.1 V, respectively, in Fig 3.⁸⁰

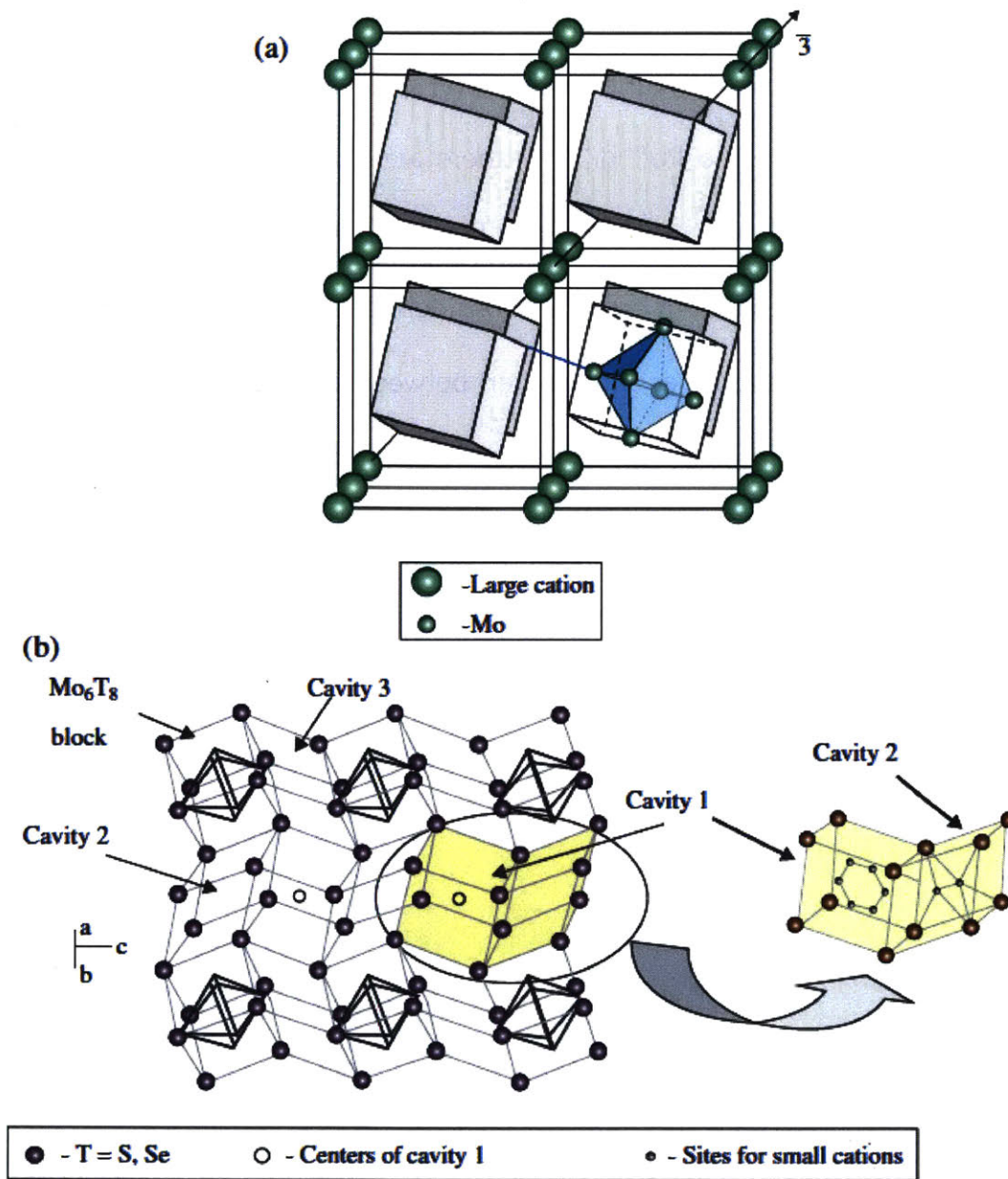


Fig. 2 Chevrel Crystal Structure⁷⁷

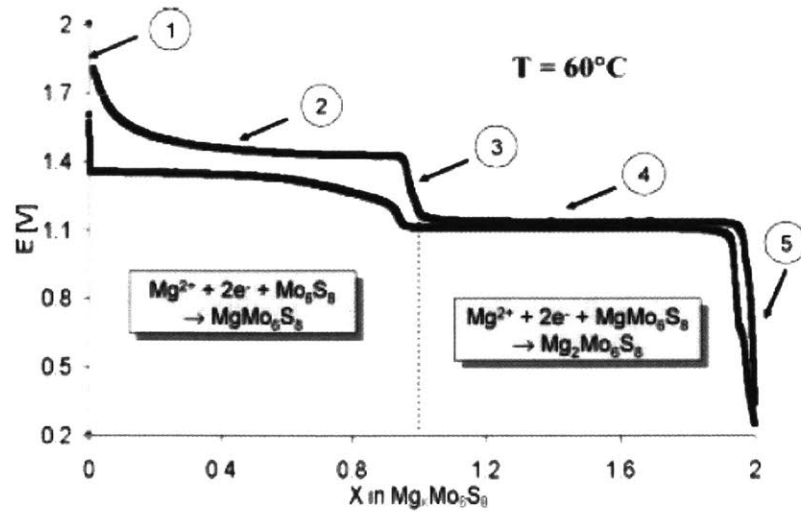


Fig. 3 Voltage-capacity curve of Mg insertion into Mo₆S₈

The un-intercalated Chevrel Mo₆S₈ structure is thermodynamically unstable, but can be obtained metastably by first synthesizing CuMo₆S₈ commonly through element solid-state reaction (or alternatively through lower temperature precipitation methods),⁸¹ followed by acid leaching Cu from the synthesized phase.⁸²⁻⁸⁴

Several different monovalent, divalent, and recently trivalent cations⁴⁵ have shown mobility within the Chevrel structure.⁸⁵ For example, the electrochemically extracted diffusivities for Co²⁺, Ni²⁺, Fe²⁺, Cd²⁺, Zn²⁺, and Mn²⁺ are quite high in Mo₆S₈, ~10⁻⁹ cm²/s,⁴⁷ compared to ~10⁻¹¹–10⁻¹³ cm²/s for Mg²⁺.⁸⁶ As mentioned earlier, different cations occupy different sites within Cavity 1 and Cavity 2, which contributes to the complex mobility behavior observed across varying cation species.⁸⁵ For example, poor mobility is observed for large cations such as Pb²⁺, Sn²⁺, and Ag⁺ compared to smaller cations such as Ni²⁺, Zn²⁺, and Li⁺ in the ternary structure (e.g. MMo₆T₈), but in mixed cation systems (e.g. M'MMo₆T₈) coupled diffusion of small and large cations is possible as

observed in insertion-displacement reactions.^{79, 87} Notably, the presence of Cu in the host structure has a beneficial effect on the Mg^{2+} intercalation kinetics.^{87, 88}

Mg intercalation in Chevrel structures represents state-of-the-art performance in MV batteries, displaying excellent reversibility and intercalation kinetics. As a matter of fact, it has been the only workable cathode materials for Mg batteries till now, though great effort has been spent to look into similar open structures to Chevrel phases.

The second ever functional cathode materials for Mg battery is TiS_2 spinel. And the thesis author is part of the theoretical work to make that discovery.⁸⁹ Fig. 4 shows the resulting discharge and charge profiles of the cells comprised of C- Ti_2S_4 at different rates. Cells run in APC/THF (Fig. 4a) show that at C/20 ($1\text{C} = 1 \text{ Mg}^{2+}/\text{C-Ti}_2\text{S}_4$, black curve), an initial discharge capacity of 200 mA h g^{-1} – corresponding to $\text{Mg}_{0.84}\text{Ti}_2\text{S}_4$ – was achieved with an over-potential of only 50 mV from equilibrium. The sloping curve between 1.5 V to 1 V demonstrates a solid-solution Mg^{2+} insertion mechanism, as previously predicted by theory.⁹⁰ As the cycling rates increased to C/10 and C/5, the discharge capacity dropped to 195 mA h g^{-1} and 190 mA h g^{-1} , respectively, demonstrating the surprisingly good rate capability of the material. At all three rates, the first charge shows minor irreversible capacity (10% at C/5), which disappears on the 2nd cycle (Fig. 4a inset). Long term cycling was examined in APC/tetraglyme (APC/G4), an electrolyte whose higher boiling point ($275 \text{ }^\circ\text{C}$) supports longer term cycling. Similar capacities of 195 mA h g^{-1} at C/20, dropping to 175 mA h g^{-1} at C/5, were observed. From cycle 2 onward (Fig. 4b), the drop levels off, and a capacity of 140 mA h g^{-1} is attained after 40 cycles at C/10. The origin of

the cycling fade might be due to the micron-sized active material particles that are large enough to kinetically trap Mg^{2+} during charge, which will be the subject of future studies. The present communication aims to report the overall new features and electrochemistry of cubic $\text{Mg}_x\text{Ti}_2\text{S}_4$.

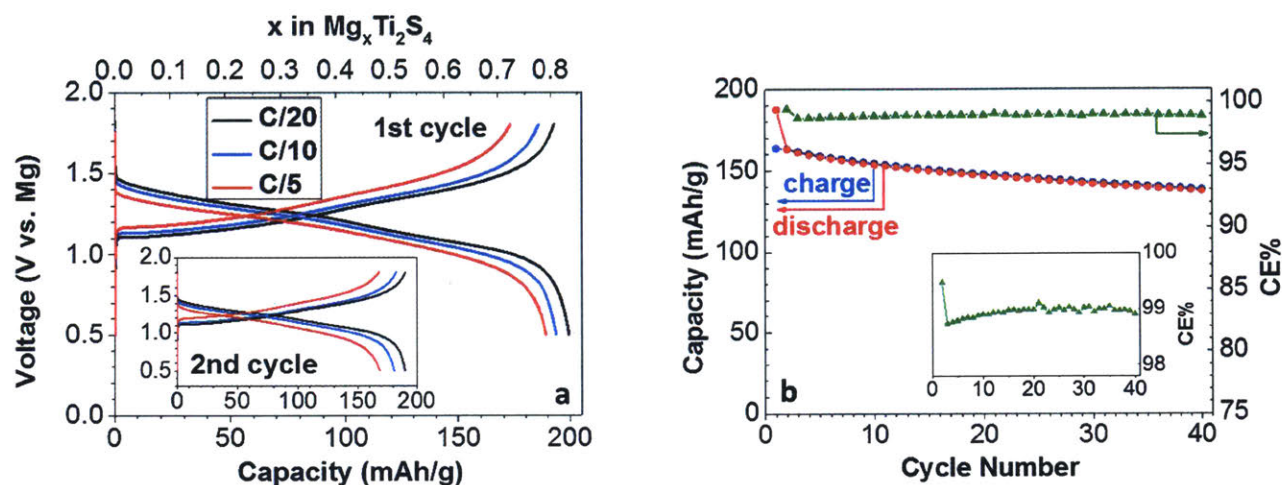


Fig. 4 Electrochemistry of C- Ti_2S_4 coin cells with an APC electrolyte and a Mg negative electrode at 60 °C. (a) Discharge and charge curves of the first and second (inset) cycles at various rates in APC/THF electrolyte. (b) Capacity and coulombic efficiency (CE) evolution at a C/10 rate in APC/G4 electrolyte (inset showing 99% CE).

The reversible intercalation of Mg^{2+} into C- Ti_2S_4 was confirmed by X-ray diffraction (XRD) as shown in Fig. 5a, and by energy dispersive X-ray analysis. Rietveld⁹¹ refinement of the discharged XRD pattern (Fig. 5b) indicated the preservation of the $Fd\bar{3}m$ cubic spinel phase, with lattice parameters expanded to 10.097 Å from their pristine values (9.776 Å) on electrochemical magnesiation of 0.8 Mg. Fourier mapping carried out with Cu, Ti, and S occupying their normal sites revealed electron density on both the tetrahedral (8a) and octahedral (16c sites). Mg was placed on both these sites in the

subsequent refinements of Mg occupancy, resulting in ~30% occupation of the octahedral 16c site and ~20% on the tetrahedral 8a site. The corresponding composition $\text{Mg}[\text{oct}]_{0.59(1)}\text{Mg}[\text{tet}]_{0.189(7)}\text{Cu}_{0.1}\text{Ti}_2\text{S}_4$ is in excellent agreement with the electrochemical capacity ($\text{Mg}_{0.84}\text{Ti}_2\text{S}_4$) and the EDX data. Only relatively minor shifts in the atomic positions occur on magnesiation. Along with the moderate volume expansion on full insertion (10%), this confirms that the structure of the Ti_2S_4 thiospinel exhibits little distortion on Mg cycling, which promotes good capacity retention. Upon charging the material, the XRD pattern (red) reverts to the pristine composition with a cell parameter of $a = 9.806 \text{ \AA}$. EDX and XRD confirm that Mg^{2+} is essentially removed from the C- Ti_2S_4 . The composition of $\text{Mg}_{0.08}\text{Ti}_2\text{S}_4$ determined by EDX and the tiny increase in the lattice parameter (*vis a vis* 9.776 \AA) are in accord with a trace of Mg remaining on the 16c site. Overall, the data unequivocally show that the electrochemical activity of the material is due to reversible (de)intercalation of Mg^{2+} into the spinel structure.

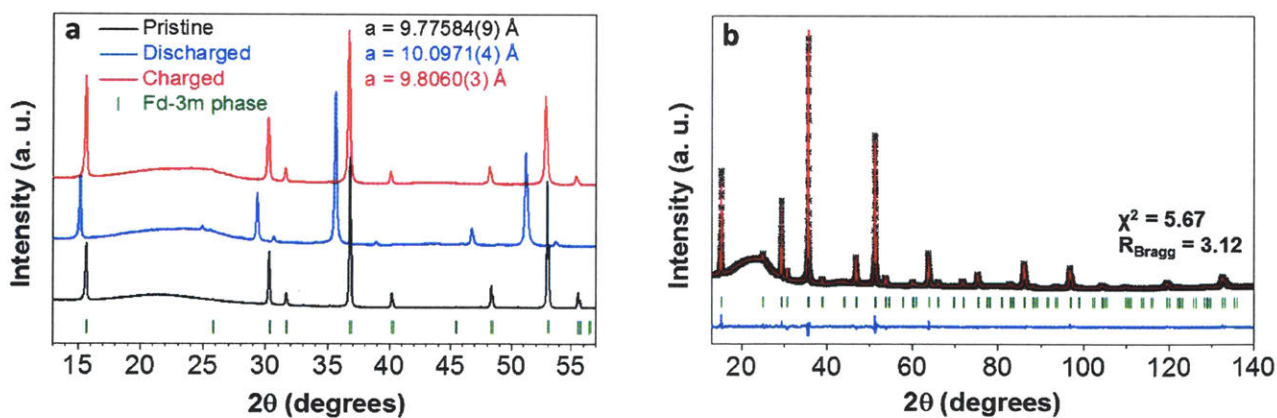


Fig. 5 XRD patterns of $\text{Mg}_x\text{Ti}_2\text{S}_4$. (a) Comparison of the XRD pattern of the initial C- Ti_2S_4 spinel (black), with the discharged (blue) and charged (red) states. The electrodes were cycled in APC/THF electrolyte with a Mg anode at $60 \text{ }^\circ\text{C}$ and a C/20 rate. (b)

Rietveld refinement fit of the discharged sample, $\text{Mg}_{0.8}\text{Ti}_2\text{S}_4$. Black crosses – experimental data, red lines – fitted data, blue line – difference curve between observed and calculated data, green ticks – the Bragg peak positions. The broad hump is a background signal from the X-ray capillary.

The above findings are consistent with the measurements of the self-diffusion coefficient of Mg^{2+} (D_{Mg}) using the galvanostatic intermittent titration technique (GITT)⁹² at 60 °C. The resulting D_{Mg} values, shown in Fig. 6a, were converted to activation energies (E_a) using the typical Arrhenius-type relation and are shown in Fig. 6a as a function of state-of-discharge (x). First principles calculations of E_m in the thiospinel are shown in Fig. 6b at both the dilute (Ti_2S_4) and concentrated ($\text{Mg}_{7/8}\text{Ti}_2\text{S}_4$) limits. The barriers are lower than those reported in other work⁹⁰ due to the difference in lattice parameters used in the calculations; we used lattice parameters of 9.78 Å (the experimental value) for the dilute limit cubic Ti_2S_4 , and 10.05 Å for the concentrated limit. The average calculated barrier height of about 550 meV agrees very well with the average experimentally determined E_a . In Fig. 6a, the increase in the barrier height to Mg^{2+} diffusion at $x > 0.6$ results in a kinetic limitation, explaining why we do not achieve $x = 1$ during discharge. Cycling $\text{Mg}_x\text{Ti}_2\text{S}_4$ at 25 °C further slows down diffusion, which causes the potential to drop more quickly, yielding a capacity of about 130 mA h g^{-1} . At the end of discharge the experimental activation energy for Mg diffusion increases sharply. Calculations considering only a tri-vacancy diffusion mechanism⁶⁷ cannot explain this increase in E_a , as demonstrated by the lower diffusion barrier height in Fig. 6b at the concentrated limit. Instead, the reduced

Mg²⁺ mobility near the end of discharge indicates the important role of site-disorder and/or Mg–Mg interaction in determining Mg²⁺ diffusivity. For example, at high Mg²⁺ concentration the number of possible tri-vacancy hops likely decreases, replaced by di-vacancy hops. A di-vacancy means that one of the three octahedral sites adjacent to the intermediate tetrahedral site is occupied, which increases the migration barrier.

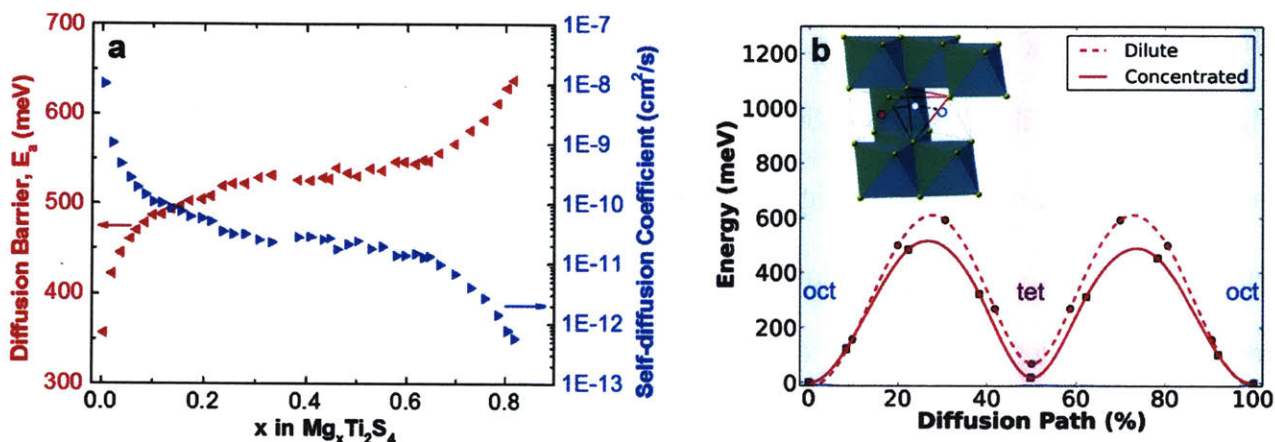


Fig. 6 (a) Mg self-diffusion coefficients and corresponding energy barriers of $C-Ti_2S_4$ determined by galvanostatic intermittent titration technique (GITT) at 60 °C; (b) energy barriers for Mg-ion migration in Ti_2S_4 , calculated in the dilute and concentrated limits. Barriers are for migration through a tri-vacancy mechanism.

Since Mg²⁺ occupation on the tetrahedral site was not identified in early studies of chemical magnesianation (albeit limited to $Mg_xTi_2S_4$ where $x < 0.5$ ⁹³) we carried out first principles calculations to explore the relative energy of compositions with various site occupations. Fig. 7a shows the formation energy of $Mg_xTi_2S_4$ configurations with Mg²⁺ cations in either tetrahedral sites (magenta squares), octahedral sites (blue circles), or mixed tetrahedral-octahedral (green triangles) configurations. While the lowest energy

states clearly have Mg^{2+} in octahedral sites, the energy difference with tetrahedral and mixed occupancy states is rather small, making disorder across octahedral and tetrahedral sites likely. Note that because the energy in Fig. 7a is normalized per unit of Ti_2S_4 , the increasing energy difference between structures with octahedral and tetrahedral occupancy with x is simply a reflection of the increased Mg^{2+} concentration in the structure, not necessarily of a change in site energy difference.

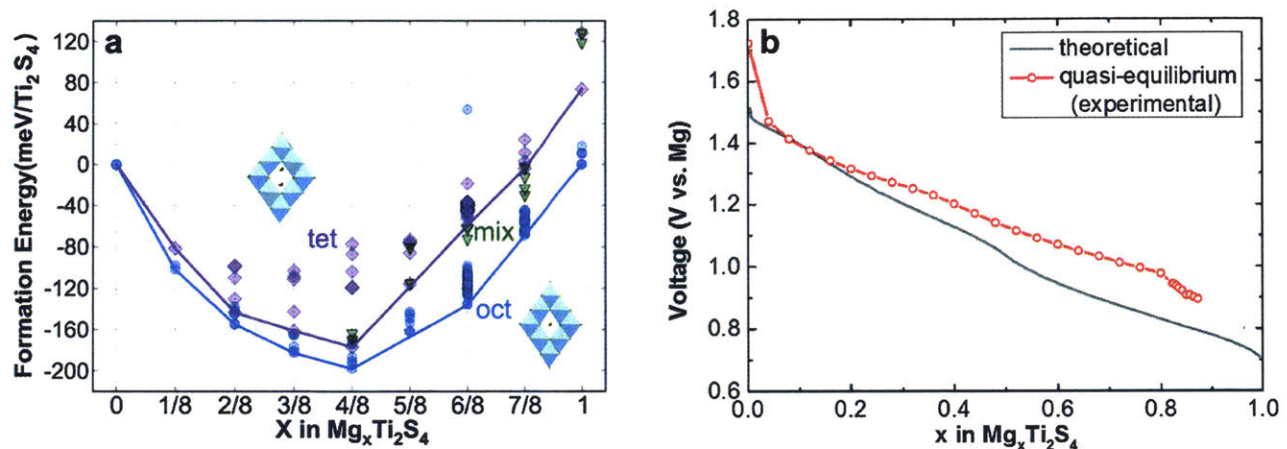


Fig. 7 (a) Calculated formation energies for different Mg occupancy orderings in Ti_2S_4 spinel. Three types of scenarios are considered: Mg occupying tetrahedral sites (magenta color, square markers), Mg occupying octahedral sites (blue color, round markers), and the co-existence of both tet. and oct. site-occupancies (green), (b) comparison of an experimental (grey) and theoretical (red) equilibrium voltage curve for $Mg_xTi_2S_4$. The theoretical curve was calculated by Emly *et al.*⁹⁰. The experimental curve was collected using a GITT experiment at 60 °C. The slight difference in the degree of the slope resulted from factors such as residual Cu in the structure, which was not included in the calculation.

These findings shed light on the observed mixed site occupation at higher Mg content that we observed experimentally, with about 30% occupancy on octahedral sites (16c) and about 20% on tetrahedral sites (8a). A closer examination of partially discharged C-Ti₂S₄ materials (0.4 and 0.6 Mg/C-Ti₂S₄) reveals that Mg²⁺ only occupies octahedral sites at this intercalation limit. Such preferential Mg²⁺ occupation on the octahedral site at low content was also observed by Bruce *et al.* in the entire range of their studies (0.07–0.5 Mg/Ti₂S₄).⁹³ A somewhat stepwise Mg²⁺ insertion behavior is therefore suggested by our findings, with the 16c site being filled first, followed by population of the 8a site that is driven by subtle thermodynamic and kinetic factors. The solid solution-like nature of the discharge/charge curves suggests that at the cross-over point, the energetics for occupation of either site are similar and the system lowers its (electrostatic) energy by distributing Mg²⁺ over both tetrahedral and octahedral sites. We propose that upon Mg²⁺ insertion beyond $x = 0.5$, energetics that result in coulombic repulsion favor redistribution amongst the possible sites. Based on our experimental results, this limitation occurs at about 0.6 Mg²⁺/Cu_{0.1}Ti₂S₄. The Mg²⁺ diffusion pathways thus become partially hindered, which could be the reason behind the increase in E_a above about $x = 0.6$, explaining the deviation of our equilibrium electrochemical profile – obtained by the galvanostatic intermittent titration technique (GITT) – from that predicted for Mg occupation on the 16c octahedral site based on previously reported first principles calculations⁹⁰ (Fig. 7b). Thus, both thermodynamics (population of mixed oct-tet sites) and kinetics could, and probably do, contribute to the voltage drop at the end of discharge. Further detailed studies are

underway in order to understand this complex behavior and its influence on the electrochemistry.

1.4 High-throughput Calculations

Materials discovery today involves significant trial-and-error. It can require decades of research to identify a suitable material for a technological application, and longer still to optimize that material for commercialization. A principal reason for this long discovery process is that materials design is a complex, multi-dimensional optimization problem, and the data needed to make informed choices about which materials to focus on and what experiments to perform usually does not exist.

What is needed is a scalable approach that leverages the talent and efforts of the entire materials community. The Materials Genome Initiative, launched in 2011 in the United States, is a large-scale collaboration between materials scientists (both experimentalists and theorists) and computer scientists to deploy proven computational methodologies to predict, screen, and optimize materials at an unparalleled scale and rate. Many research groups have already employed this high-throughput computational approach to screen up to tens of thousands of compounds for potential new technological materials. Examples include solar water splitters,^{94, 95} solar photovoltaics,⁹⁶ topological insulators,⁹⁷ scintillators,^{98,99} CO₂ capture materials,¹⁰⁰ piezoelectrics,¹⁰¹ and thermoelectrics,^{102, 103} with each study suggesting several new promising compounds for experimental follow-up. In the fields of catalysis,¹⁰⁴ hydrogen storage materials,^{105, 106} and Li-ion batteries,¹⁰⁷⁻¹¹¹ experimental “hits” from high-throughput computations have already been reported.

Applying similar ideas from the Materials Genome Initiative project, if we can find whether one structure is good for being a Mg battery cathode materials by doing one calculation, in principle if we build up a system where we can calculate the Mg diffusivity over thousands of different materials, then we can pick the good one from the high-throughput (HT) calculation results. And that is the idea behind this thesis.

Chapter 2 Methodology

2.1 Migration State Calculation

There are two main classes of methods to calculate diffusivity from first-principles, i.e., the Transition State Theory (TST)^{112, 113} and Molecule Dynamics simulation (MD)^{114, 115}, where the saddle point is strictly sought and calculated in TST but not in MD. Both these methods are computationally expensive and thus pose a challenge for scaling up to HT calculation. The computational runtime to converge an Ab-initio MD simulation follows the Arrhenius equation¹¹⁶ and therefore is limited to small materials systems where the diffusion barrier is relatively low. Most often, the diffusion events of interest have high migration barriers and are many orders of magnitude slower than the vibrations of the atoms. Therefore, scaling MD into HT environment is not feasible. In TST, the minimum-energy path (MEP) between initial and final states is calculated and then the results are used for estimating transition rates within the harmonic transition state theory (hTST) approximation^{117, 118}. Many different methods have been presented for finding MEPs and saddle points¹¹⁹⁻¹²¹, among them the nudged elastic band (NEB)^{122, 123} method have been widely used due to its efficiency and relative robustness given that the initial and final

states of the diffusion are known. In NEB calculations, a set of images (replicas) of the system is interpolated between the initial and final states. A spring force between adjacent images is added to ensure the continuity of the path, thus mimicking an elastic band. An optimization of the band, involving minimizing of the force acting on images, relaxes the band to the MEP.

The key information both TST and MD seek after is the migration barrier for the diffusion, defined as the energy difference between saddle point and the initial state. Because the diffusivity scales as the inverse exponential of the barrier, it is the controlling factor for diffusion events and an increase of 60meV in the migration barrier corresponds to a decrease of one order of magnitude in the diffusivity at room temperature¹²⁴.

2.2 Threshold for Cation Mobility in MV Cathode

An upper bound for the MV migration barrier E_m can be established from reasonable battery performance criteria: a 2 hours (dis)charge time t (or $C/2$ rate) for a 1 μm active particle size suggests a minimum diffusivity $D \sim 10^{-12} \text{ cm}^2\text{s}^{-1}$ given the diffusion length scales as \sqrt{Dt} . Using a random walk for diffusion sets a maximum $E_m \sim 525 \text{ meV}$ that can be tolerated, assuming $D \approx \nu \cdot a^2 \cdot \exp(-E_m/kT)$ with atomic jump frequency $\nu \approx 10^{12} \text{ s}^{-1}$ and atomic jump distance $a \approx 3 \text{ \AA}$, the length of a typical lattice parameter. For every order of magnitude particle size reduction this tolerance increases by $\sim 125 \text{ meV}$. Hence, 100 nm crystallites could be charged and discharged in 2 hours when barriers are less than $\sim 650 \text{ meV}$. Note that reasonable ion diffusion is a required condition for cathode materials, but it is by no means sufficient as other phenomena, either in the cathode (e.g.

phase transformations, conductivity) or in the cell, can be rate limiting. Nonetheless, solid-state diffusion is widely seen as the most challenging design problem for MV-cathode materials.

To accommodate the fact that some materials can be engineered into nano-particles and therefore pose a less strict requirement on Mg diffusion barrier, we use 600meV as a hard criterion for screening and selecting materials.

2.3 NEB method

The nudged elastic band (NEB) method is an efficient method for finding the minimum energy path (MEP) between a given initial and final state of a transition.^{122, 123, 125} It has become widely used for estimating transition rates within the harmonic transition state theory (hTST) approximation. The method has been used both in conjunction with electronic structure calculations, in particular plane wave based density-functional theory (DFT) calculations¹²⁶⁻¹²⁹, and in combination with empirical potentials.¹³⁰⁻¹³² Studies of very large systems, including over a million atoms in the calculation, have been conducted.¹³³ The MEP is found by constructing a set of images (replicas) of the system, typically on the order of 4–20, between the initial and final state. A spring interaction between adjacent images is added to ensure continuity of the path, thus mimicking an elastic band. An optimization of the band, involving the minimization of the force acting on the images, brings the band to the MEP. An essential feature of the method, which distinguishes it from other elastic band methods,^{134, 135} is a force projection which ensures that the spring forces do not interfere with the convergence of the elastic band to the MEP, as well as ensuring that the true force does not affect the distribution of images along the MEP. It is necessary

to estimate the tangent to the path at each image and every iteration during the minimization, in order to decompose the true force and the spring force into components parallel and perpendicular to the path. Only the perpendicular component of the true force is included, and only the parallel component of the spring force. This force projection is referred to as “nudging.” The spring forces then only control the spacing of the images along the band. When this projection scheme is not used, the spring forces tend to prevent the band from following a curved MEP because of “corner-cutting”, and the true force along the path causes the images to slide away from the high-energy regions towards the minima, thereby reducing the density of images where they are most needed (the “sliding-down” problem). In the NEB method, there is no such competition between the true forces and the spring forces; the strength of the spring forces can be varied by several orders of magnitude without effecting the equilibrium position of the band.

The MEP can be used to estimate the activation energy barrier for transitions between the initial and final states. Like the Fig. 8 below is a demonstration of NEB calculations, which characterizes the system energy when cations (Li^+ , Mg^{2+} , Zn^{2+} , Ca^{2+} , Al^{3+}) migrate from one stable position to the nearest stable position in TiS_2 layer host structure. From the MEP, we can obtain the activation energy, which is the peak energy point on the curve (saddle point).

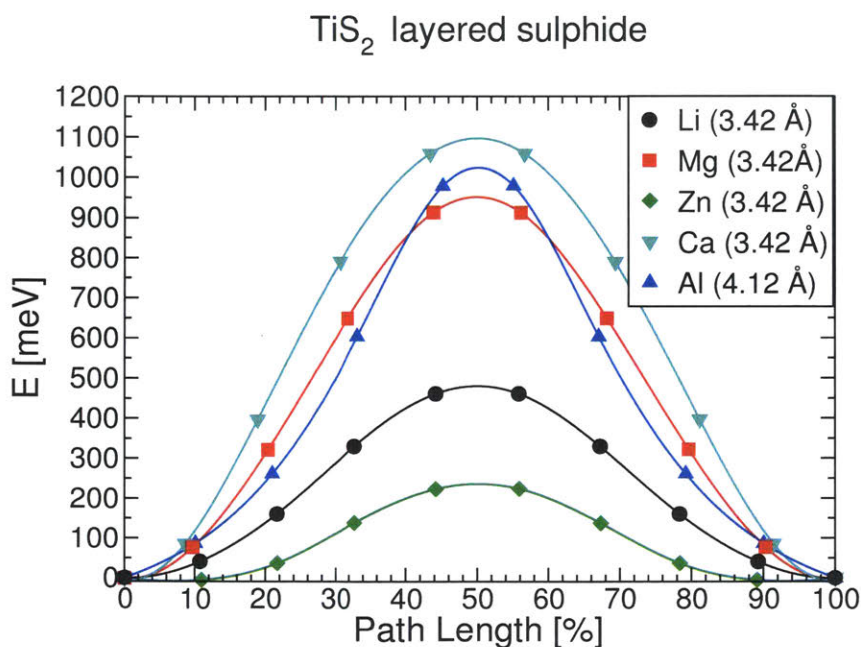


Fig. 8 NEB calculation example, in TiS₂ layer host structure

Over the past two decades, a number of algorithmic improvements have been introduced to increase stability and accuracy. Henkelman *et al.* proposed the climbing image method¹³⁶ and the improved tangent estimate,¹³⁷ which are available as part of the open-source VTST [Vienna *Ab Initio* Simulation Package (VASP) Transition State Tools] code. Maragakis *et al.*¹³⁸ presented the adaptive nudged elastic band method, where NEBs are iteratively calculated to move the initial and final states closer to the saddle point. More recently, Sheppard *et al.*¹³⁹ generalized the NEB method to address solid-solid phase transitions. Crehuet and Field¹⁴⁰ expanded the NEB formalism to account for finite temperature effects. These efforts are accompanied by other work focusing on computational details to accelerate the optimization methods of finding the MEP.^{141, 142}

To put NEB calculations into HT environment, we start by calculating NEBs manually for selected systems (Ch3, Ch4, Ch5). We realize that traditional NEB

calculation scheme is not suitable for high-throughput calculation applications as it is too time-consuming and not stable enough (Ch6). We thus develop the HT version of NEB algorithms, i.e., the PathFinder algorithm and ApproxNEB method (Ch7), and then put these algorithms to HT framework (Ch8). The results of the HT machinery is presented in Ch9 and Ch10.

Chapter 3 – Spinel Compounds as Multi-valent Battery Cathodes

3.1 Motivation for Looking into Spinel Structures

In this chapter, I present a systematic computational study of multivalent intercalation within a fixed spinel-based host structure, using a set of seven redox-active cations and spanning size and valence differences between a set of intercalating Ca, Zn, Mg, Al and Y cations to establish design trends and guidelines for future experimental work.

The spinel (prototype MgAl_2O_4 , space group $Fd\bar{3}m$) structure provides an excellent candidate for this study, encompassing a family of materials with the general formula AB_2O_4 . The A and B ions are tetrahedrally and octahedrally coordinated by oxygen, respectively (Fig. 8). The B octahedrons form a network with percolating empty sites interconnecting in three directions. Spinel LiMn_2O_4 was first prepared by Thackeray *et al.*¹⁴³ and exhibits excellent performance as a cathode for Li intercalation with a voltage of 3–4 V *versus* Li metal.¹⁴⁴ The properties of the spinel structure are tunable, for example it

has been observed that partially replacing Mn with Ni increases the voltage to 4.7 V,^{145,}
¹⁴⁶ and mixing Mn with Co and/or Cr increases the voltage even higher to ~5 V.^{145, 147, 148}

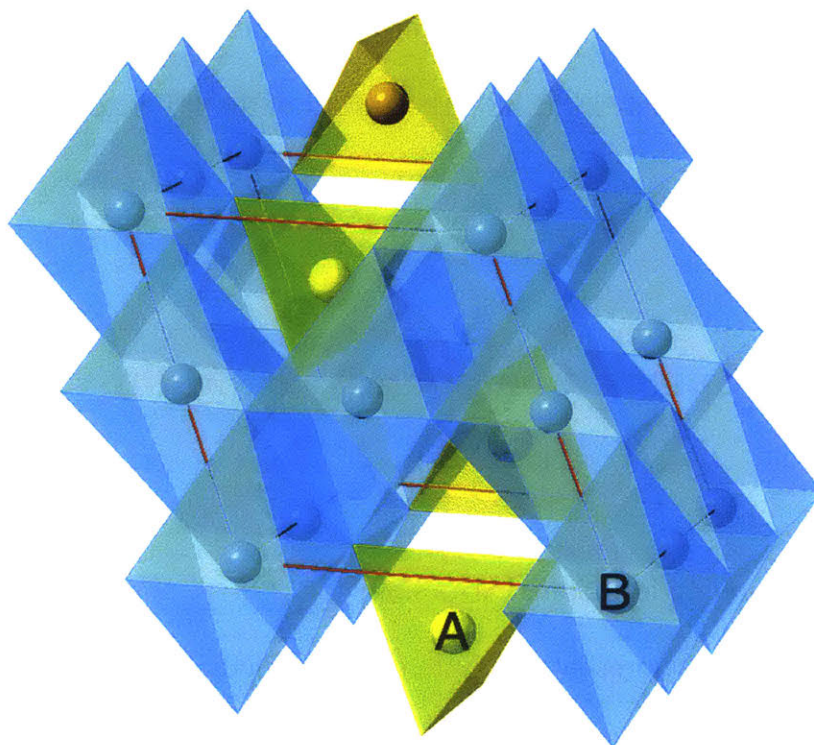


Fig. 8 The spinel crystal structure where the 'A' atoms occupy the tetrahedral sites, and the 'B' atoms occupy the octahedral site. Throughout this paper, the 'A' atoms are multivalent intercalating ions selected from the set Mg^{2+} , Ca^{2+} , Zn^{2+} , Y^{3+} , Al^{3+} , and the 'B' atoms are transition redox-active ions, selected from the set Ti, V, Cr, Mn, Fe, Co, Ni.

Experiment shows that spinel LiMn_2O_4 can be electrochemically converted to MgMn_2O_4 in aqueous $\text{Mg}(\text{NO}_3)_2$ electrolyte, and exhibits Mg^{2+} reversible intercalation/deintercalation.¹⁴⁹ Spinel ZnMnO_2 has also demonstrated Zn^{2+} insertion/deinsertion, providing a capacity of 210 mA h g^{-1} for 50 cycles.¹⁵⁰ Recently, it was shown that Mg^{2+} can intercalate/deintercalate into spinel-type Mn_2O_4 with a retained capacity of $155.6 \text{ mA h g}^{-1}$ after 300 cycles in $1 \text{ mol dm}^{-3} \text{ MgCl}_2$ aqueous

electrolyte,¹⁵¹ suggesting that further development could lead to a viable cathode with good energy density. Against this background, it is intriguing to broadly consider a multivalent spinel cathode with possible intercalating cations $A = \{\text{Mg, Ca, Zn, Al, Y}\}$ that could theoretically produce a higher capacity than its Li counterpart due to the greater charge carried by each ion. Hence, in this paper, our aim is to evaluate the cathode performance of spinel phases for multivalent intercalation; we computationally evaluate the feasibility of a matrix of spinel compounds with different redox ion species and intercalating cation species. The redox ion was selected from the set $\{\text{Ti, V, Cr, Mn, Fe, Co, Ni}\}$, and the intercalating cation was selected from the set $\{\text{Mg, Ca, Zn, Al, Y}\}$. By substituting the cations in the A and B sites, respectively, we created 35 charged/discharged topotactic pairs and performed first-principles density functional theory (DFT) calculations for each of these pairs. We evaluate cathode performance through such quantities as the capacity, average voltage, energy density, and intercalating cation mobility. We also evaluate the thermodynamic structural and thermal stability. The detailed methodology can be found in previous literature.¹⁵²

3.2 Computational Methods

We use the Vienna *ab initio* software package (VASP)¹⁵³ to perform the density functional theory calculations, with the projector augmented-wave method¹⁵⁴ to describe the ion–electron interactions and the generalized gradient approximation (GGA)¹⁵⁵ within the Perdew–Burke–Ernzerhof (PBE) framework¹⁵⁶ as the exchange–correlation functional. The calculation parameters are the same as those adopted by the Materials Project¹⁵⁷ and as implemented in the pymatgen software package,¹⁵⁸ which have been previously tested to be appropriate to study Li-intercalation cathode materials.¹⁵² In the calculations, the U – J parameters to correct for non-cancellation of the

self-interaction error in the d orbitals of the redox active species are set to $U_V = 3.25$ eV, $U_{Cr} = 3.7$ eV, $U_{Mn} = 3.9$ eV, $U_{Fe} = 5.3$ eV, $U_{Co} = 3.32$ eV, and $U_{Ni} = 6.45$ eV.¹⁵⁹ The primitive spinel unit cell as illustrated in Fig. 8 is used for voltage and stability calculations. Brillouin zone sampling is performed on a $5 \times 5 \times 5$ grid in k -space. Throughout this work, the cell shape, volume and atomic positions are relaxed, unless otherwise stated. All magnetic ions are initialized ferromagnetically.

All calculations in this paper assume that the transition metal host framework 'B₂O₄' remains structurally invariant during the operation of the battery (*i.e.*, during intercalation and de-intercalation of 'A' cations). Additionally, we assume that the host can be synthesized with little/no disorder and remains that way during the operation of the cell. We acknowledge that spinels are well known to show varying degrees of cation disorder that may impact important material properties relevant for battery operation such as the activation energies and voltages reported herein. However, in the interest of providing a preliminary view of what is possible in multivalent systems, we have simplified our calculations and analysis.

The voltages of the compounds can be obtained from the difference in the total energy between the charged and discharged phases following Aydinol *et al.*^{160, 161} The average voltage can be calculated as $\bar{V} = \Delta E/nz$, where $\Delta E = (E_{\text{charge}} + E_{\text{MV}} - E_{\text{discharge}})$ denotes the total energy change in the reaction, E_{charge} and $E_{\text{discharge}}$ are the energy of the charged and discharged compounds respectively; E_{MV} is the energy of multivalent intercalating species in metal form; n is number of intercalating atoms participating in the reaction; and the z represents the oxidation state of the intercalant. We adopt the units of eV and e for ΔE and nz , respectively, so that no normalization factor (*i.e.*, Faraday's constant) needs to be introduced into the equation. We estimate the thermodynamic stability of the phases by the energy above the convex hull of stable phases, which is the energy released by decomposing the compound to the most stable combination of

compounds at the same overall composition.^{162, 163} The energy above the hull is always a non-negative number with the unit of eV per atom. The detailed procedure for the computation of the energy above the hull can be found in previous literature.^{162, 163} As explained later in this paper, the thermal stability was determined by evaluating the critical chemical potential at which O₂ gas becomes favorable according to the methodology presented in Ong *et al.*¹⁶⁴ Since the entropy of a reaction is dominated by the gas entropy and the entropy of the solid phase at room temperature,¹⁵⁹ for the any reactions containing molecular O₂, we use the corrected O₂ chemical potential to include the well-known O₂ DFT calculation error¹⁵⁹ as well as the $P\Delta V$ contribution to the oxygen enthalpy¹⁶⁴ by comparing with the experimental thermodynamic data for O₂ at 0.1 MPa at 298 K throughout the paper. For the thermal stability calculation, the temperature effect has been taken into account by adjusting the entropy term ($-T\Delta S$) of the O₂ chemical potential at given temperature.¹⁶⁵

The calculations were automatically executed and analyzed using the *FireWorks* software package. In this work, hundreds of DFT calculations are performed across 70 compounds to generate the thermodynamic stability and thermal stability data.^{162, 163}

Activation barriers were calculated with the nudged elastic band (NEB) method¹³⁶ using the GGA-PBE functional.^{156, 166} A U term was not included in these calculations as NEB is difficult to converge with GGA+ U due to pronounced metastability of electronic states along the ion migration path. Furthermore, while GGA+ U clearly improves the accuracy of redox reactions,¹⁵² there is no conclusive evidence that GGA+ U performs better in predicting cation migration.^{70, 167-170} The minimum energy paths (MEP) in the NEB procedure were initialized by linear interpolation of 8 images between the two fully relaxed end-point geometries, and each image is converged to $<1 \times 10^{-4}$ eV per super cell. The MEPs were obtained in both the high vacancy limit and dilute vacancy limit, *i.e.* one mobile species per unit cell or one vacancy per

unit cell. To ensure that fictitious interactions between the diffusing species are removed, a $2 \times 2 \times 2$ supercell of the primitive cell was used, for which the inter-image distance is never less than 8 Å.

3.3 Voltages, Capacities, Stabilities, Safety and Diffusivities

The average intercalation voltage was calculated from the reaction energy $B_2O_4 + A \rightarrow AB_2O_4$ for the matrix of intercalating $A = \{Mg, Ca, Zn, Y, Al\}$ ions and redox active transition $B = \{Ti, V, Cr, Mn, Fe, Co, Ni\}$ metal cations. Fig. 9 shows the resulting voltage vs. the gravimetric capacity, where the color and shape of a data point indicate the intercalating ion, and the redox-active transition metal is given next to each data point. Voltages are referenced to the bulk metal of the intercalating ion, e.g., Mg metal for $MgMn_2O_4$ and Zn metal for $ZnMn_2O_4$.

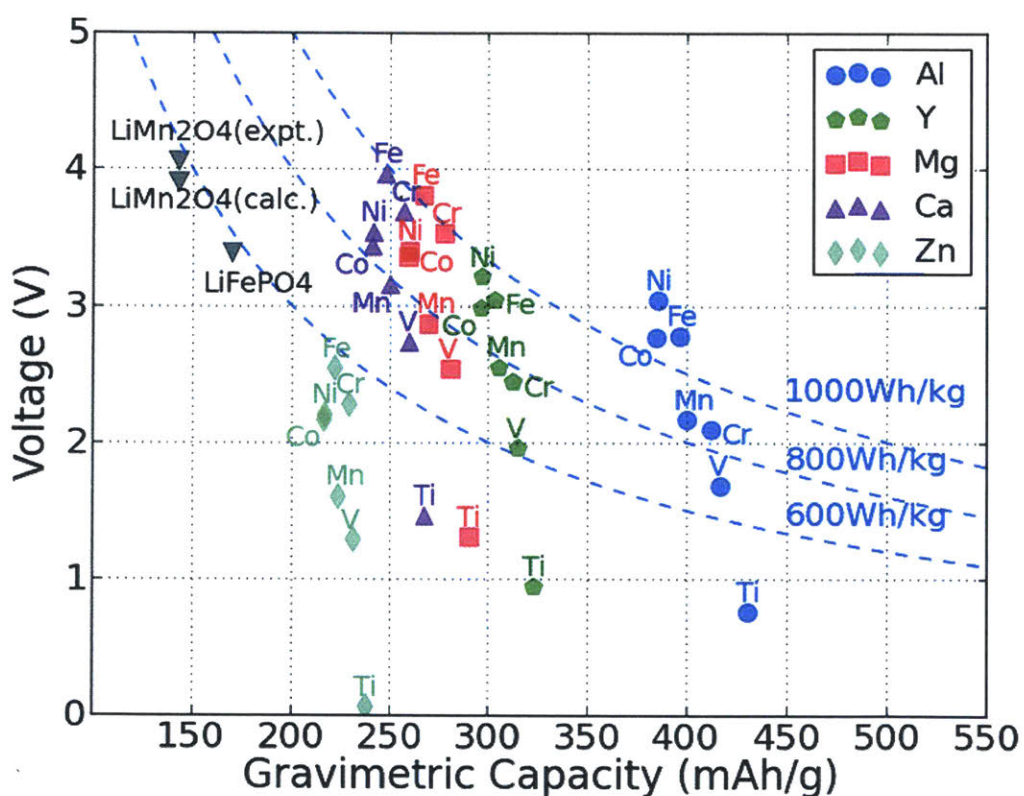


Fig. 9 The computed average voltage vs. gravimetric capacity for intercalation of $A = Zn, Ca, Mg, Y$ and Al in various M_2O_4 spinels up to composition AM_2O_4 . The redox-active metal is marked next to each point. Dashed curves show the specific energy of 600 W h kg^{-1} , 800 W h kg^{-1} and 1000

W h kg^{-1} , respectively. The spinel LiMn_2O_4 and olivine LiFePO_4 data points are also marked on the plot for comparison.^{143, 157, 164}

As expected from the electrochemical series, and evidenced in Fig. 9, multivalent compounds have lower voltages than Li cathodes. The Li spinel usually exhibits a voltage between 4 and 5 V,^{143, 147, 171} whereas we find that for multivalent spinel cathodes, the voltage is always less than 4 V *versus* the corresponding metal. Most Mg and Ca intercalation voltages vary between 2 and 4 V, which is lower than the values for Li (e.g., calculated voltage of LiMn_2O_4 is ~ 0.7 V higher than CaMn_2O_4);^{143, 172} however, considering the additional charge carried by multivalent cations, a multivalent spinel cathode can still exhibit a significantly higher energy density than the corresponding Li version. For example, the gravimetric capacity of LiMn_2O_4 is 143 mA h g^{-1} ,^{143, 157} whereas the gravimetric capacity of MgMn_2O_4 is almost double $\sim 270 \text{ mA h g}^{-1}$, which more than makes up for the slightly lower voltage. Hence, of the considered intercalating ions, Al, Y, Ca and Mg are all viable candidates from the perspective of energy density. However, the voltage of the Zn spinel compounds ranges between 1.3 V and 2.5 V, which even in the best case scenario amounts to approximately 600 W h kg^{-1} , about equal to the specific energy of LiFePO_4 .^{157, 164}

The voltage for each multivalent intercalant is plotted as a function of the active redox metal in Fig. 10(a): the bi-valent ions Ca, Mg, and Zn follow a common trend as the redox couple is varied, different from the voltage trend of the tri-valent intercalants Al and Y. The difference originates largely from the different valence state of the transition metal in the discharged state. Insertion of the bi-valent cations induces a change in redox state from 4+ to 3+, whereas the tri-valent cation corresponds to a redox change from 4+ to 2.5+ for insertion into AB_2O_4 .

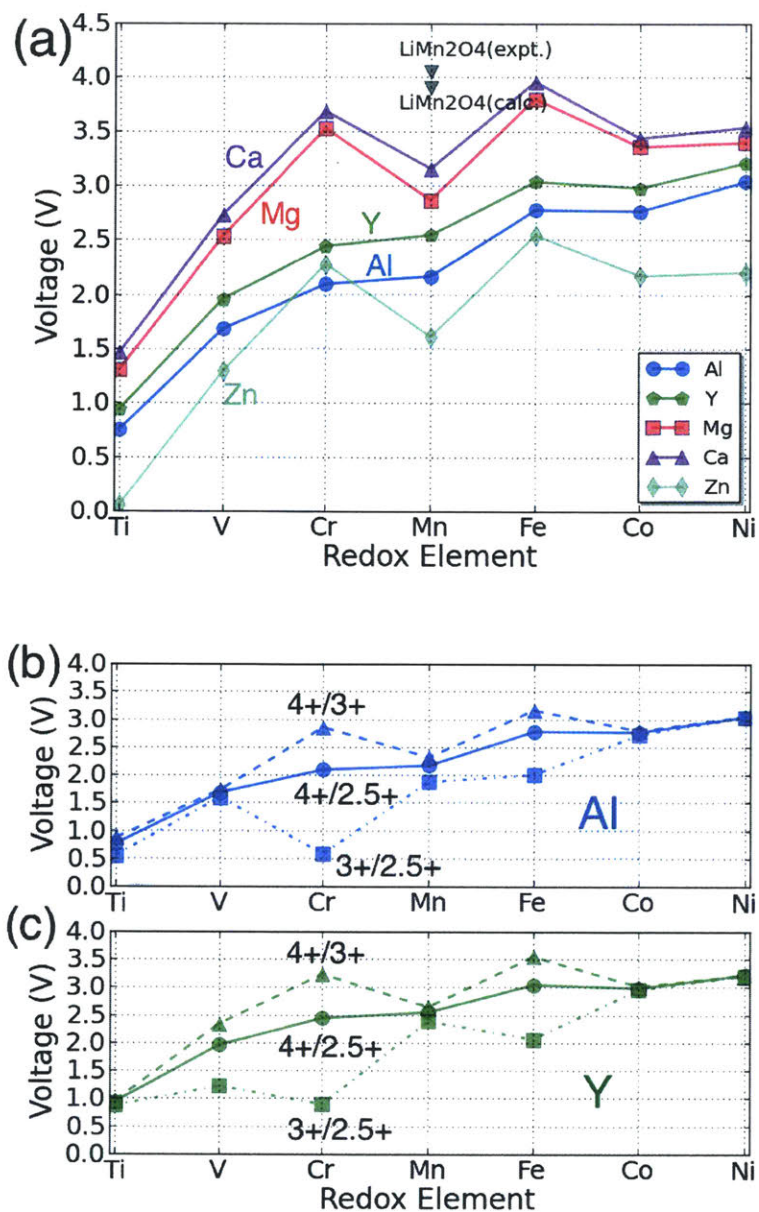


Fig. 10 (a) The calculated voltage of each spinel phase for the reaction $\text{B}_2\text{O}_4 + \text{A} \rightarrow \text{AB}_2\text{O}_4$ as a function of the redox-active transition metal and intercalating cation. The different colors denote different intercalating species as specified by the legend. The black triangle point indicates the data corresponding to the spinel LiMn_2O_4 ^{143, 157} (b) and (c): for Y and Al the voltage for separate 3+/2.5+ and 4+/3+ redox reactions is compared to the overall voltage for the 4+/2.5+ redox change corresponding to the full intercalation range, as in (a).

In general, the Ca spinel has the highest voltage, followed by the Mg spinel compounds, Y compounds, Al compounds, and Zn compounds, in that order. For all the redox active cations {B = Ti, V, Cr, Mn and Ni} the voltage of the Mg compounds is lower than that of the Ca compounds by ~0.2 V, and the voltages of Mg compounds are ~1.4 V higher than Zn compounds. The three bi-valent intercalants show the same trend of voltage versus redox active metal: Ti_2O_4 always has the lowest voltage among the transition metals considered. V_2O_4 is the second lowest one but ~1.2 V higher than Ti_2O_4 . Mn_2O_4 is ~0.3 V higher than V_2O_4 , Co_2O_4 is ~0.6 V higher than Mn_2O_4 , and Ni_2O_4 is slightly higher than Co_2O_4 by ~0.1 V. The Cr_2O_4 and Fe_2O_4 spinels have the highest voltage, respectively ~0.6 V and ~0.9 V higher than Mn_2O_4 . Bhattacharya *et al.* found a similar trend for the Li insertion voltage in spinels.⁵⁴ We find that Li insertion¹⁷² occurs on average at about ~0.7 V higher voltage than Ca insertion and ~0.9 V higher than Mg insertion. Comparing this with the aqueous electrochemical series ($E^0_{Li} = -3.04$, $E^0_{Ca} = -2.86$, $E^0_{Mg} = -2.37$, $E^0_{Zn} = -0.76$) we find that the voltages are ordered according to the electrochemical series of the intercalating metal ion. However, while the voltage shift between Li and Mg is close to what is expected, the voltage reduction in moving from Li to Ca in the solid state is considerably larger than expected from the electrochemical series. This is likely due to the fact that the intercalant enters a tetrahedral site in the spinel, which for Ca is not nearly as favorable as for Mg and Li, and thus reduces the Ca intercalation voltage from what one would expect from the electrochemical series. Experimentally, Li has indeed been found to exhibit a higher voltage than Mg. In the Chevrel phase Mo_6S_8 , the voltage difference between Li and Mg insertion is ~1.0–1.2 V.^{13, 74, 173} For V_2O_5 , the Li voltage is usually ~0.2 V higher than that of Mg.¹⁷⁴⁻¹⁷⁶

Because the data in Fig. 10(a) for trivalent cations averages the voltage over both the 3+/2.5+ and 4+/3+ redox couples, the intermediate 3+ states of the transition metals were calculated for the trivalent intercalants to investigate the impact of different redox states. Fig. 10(b)

and (c) show the calculated voltage of the different redox pairs for the Al and Y spinel compounds, respectively. As expected, the 3+/2.5+ redox pairs exhibit a lower voltage compared to the 4+/3+ reactions, in good agreement with existing literature.¹⁷⁶ In particular, when restricting focus to the 4+/3+ redox reaction, the Al and Y spinel compounds follow largely the same trend as Ca, Mg and Zn as shown in Fig. 10(a).

The capacity of cathode materials is important as it strongly influences the overall energy density of a cell. Fig. 11(a) shows the volumetric capacity of each AB₂O₄ spinel as a function of the redox-active species and intercalating cation. The volumetric capacity of all the cathodes is higher than that of a Li spinel cathode at the same cation concentration due to the extra charge carried by each of the multivalent intercalants. Not surprisingly, Al³⁺ leads to the highest capacity density, while Ca²⁺ has the lowest. For a fixed valence of the intercalant, the volumetric capacity follows the ionic size of the intercalating cation. Hence, the volumetric capacities of Al³⁺ compounds are higher than Y³⁺ compounds by approximately 300 A h L⁻¹. For bi-valent cations, the capacities of Mg and Zn compounds are almost the same, consistent with the similar ionic size of Mg²⁺ or Zn²⁺.

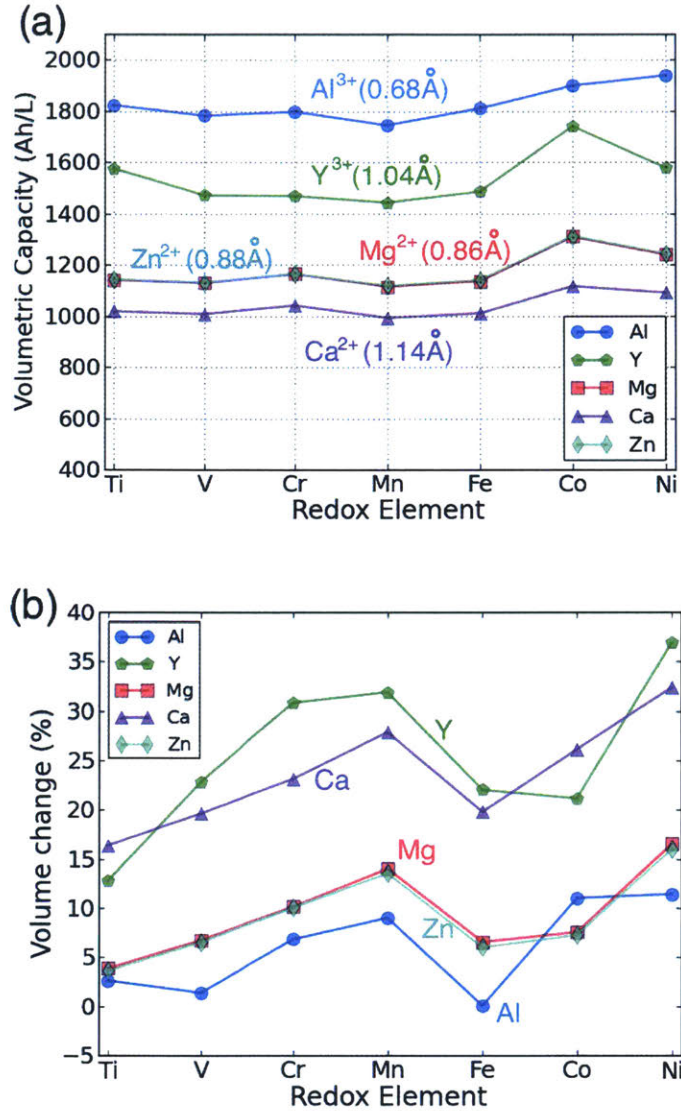


Fig. 11 The calculated (a) volumetric multivalent capacity and (b) volume change of the spinel structure as a function of the redox-active cation, assuming intercalation to composition AB_2O_4 .

Fig. 11(b) presents the volume expansion associated with the intercalation of each multivalent ion as function of the redox metal. Volume change is an important parameter as it needs to be accommodated at the particle, electrode and cell level. At the particle level, large volume changes can lead to particle fracture and loss of contact. The total volume change associated with intercalation is the combined result of the intercalant insertion and the transition

metal reduction, and can be very small for some Li-insertion systems.^{177, 178} The contribution from the intercalating ion will depend on its size and charge. For example, Y^{3+} leads to larger volume increase than Al^{3+} as the ion is much larger. The effect of charge cannot as easily be extracted from Fig. 11(b) as the +3 cations also cause a larger reduction of the transition metal than the 2+ cations. Reduction of the transition metals generally leads to an increase in volume, although the magnitude of the change depends on the nature of the metal-d orbital that is being filled. Filling of t_{2g} orbitals, which are to first order non-bonding,¹⁷⁸ tends to cause only a small increase in volume, while the anti-bonding e_g orbitals lead to a larger volume change.¹⁷⁷ This explains why in general the early transition metals, such as Ti and V exhibit lower volume changes. They have several unoccupied t_{2g} orbitals, which are available for reduction. On the other hand, Mn and Ni-based spinels show the largest volume changes as their reduction occurs by filling one or more e_g orbitals. For both Mn^{3+} and Ni^{3+} this volume increase is compounded by the fact that these ions are Jahn–Teller active which, in its anharmonic form, leads to additional volume increase.¹⁷⁹ The combined small size and high charge of Al^{3+} lead to almost zero volume change for several spinels.

For Mg, Zn and Al insertion, the magnitude of the volume change normalized by the capacity is very similar to the volume changes observed for Li insertion compounds, and hence is not likely to lead to any practical design problems. For Ca and Y the volume change is larger – up to 30% increase in some cases.

The thermodynamic stabilities of the charged and discharged state are important considerations for possible cathode materials, as they may influence the cycle life as well as the synthesizability of the compounds. Thermodynamic stability can be measured by the driving force for a compound to separate into its most stable combination of compounds. From first principles, this is determined by comparing the energy of the compound with the convex energy hull of all ground states in the relevant phase diagram. Fig. 12(a) and (b) provide this energy above the hull

of each compound. The ground state hulls were determined from all the calculated compounds in the Materials Project database.¹⁵⁷ A smaller energy above the hull implies that the material has a greater chance of being stable,¹⁸⁰ e.g. at synthesis and upon cycling.

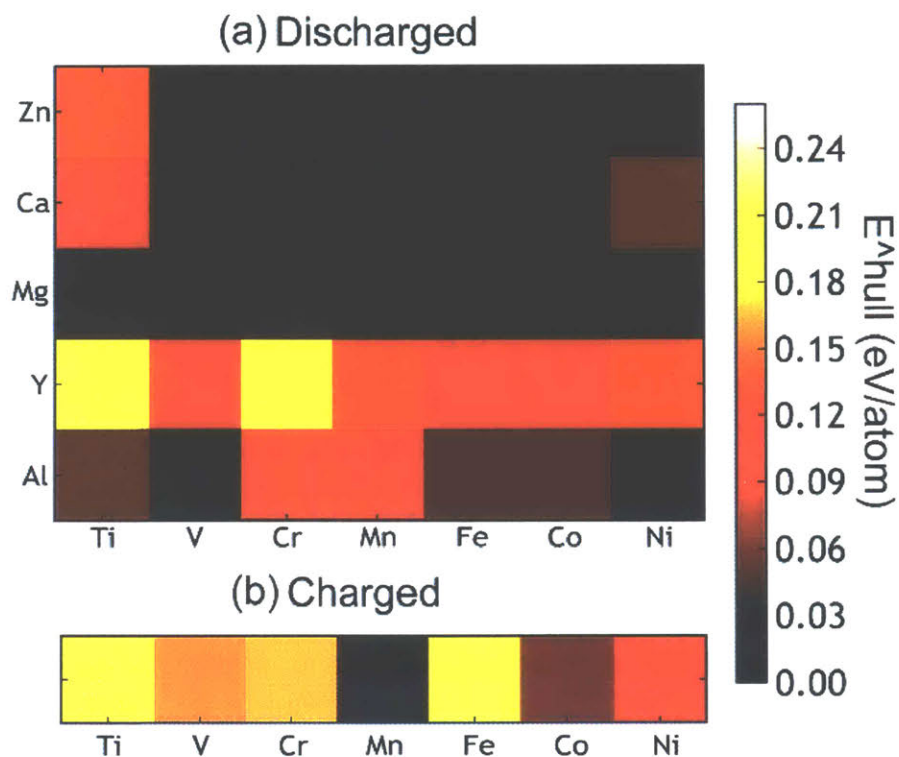


Fig. 12 (a) The calculated thermodynamic stability of the AB_2O_4 spinel compounds as a function of the intercalating ion (vertical axis) and redox metal (horizontal axis). (b) The energy above hull of the charged state which is calculated as the formation energy difference between a compound and the convex hull.

The Mg and Zn spinel phases (except $ZnTi_2O_4$) are all quite stable, exhibiting an energy above hull less than 0.011 eV per atom. Such a small value of the decomposition energy falls well within the accuracy of our calculations¹⁸⁰ or within relative changes between competing phases due to finite temperature effects. The Ca spinel structures are more thermodynamically unstable compared to the equivalent Mg and Zn compounds. This is consistent with Ca^{2+} normally

preferring coordination environments larger than tetrahedral, though it is not excluded that this coordination can be achieved through electrochemical intercalation. The Y spinel compounds are the most unstable phases among all the candidates, due to the large ionic size of Y^{3+} . The Al^{3+} spinels are also relatively unstable in the discharged state. Among the chemistries of the charged host spinel, Mn_2O_4 forms the most stable structure. The high energy above hull for Fe_2O_4 suggests the difficulty to synthesize such a phase. Indeed, Fe^{4+} is only known to exist in ternary and higher component compounds¹⁸¹ where the formation energy is lowered by the interaction with other cations. In terms of phase stability across both charged and discharged states, we conclude that $MgMn_2O_4$, $CaMn_2O_4$ and $ZnMn_2O_4$ provide the best opportunities.

A way to gauge the intrinsic safety of a potential cathode material is by the thermal stability of the compound against O_2 release. The thermal stability can be estimated by calculating the temperature at which O_2 gas release is predicted thermodynamically.¹⁶⁴ Fig. 13 shows the calculated O_2 amount released as a function of temperature for the charged spinel compounds (e.g. for B_2O_4), determined by the equilibrium chemical potentials at which O_2 release can be expected. At low temperature, the oxygen release is likely limited by kinetics and the decomposition temperatures should only be used to rank compounds relative to their oxidation strength. Clearly, the data in Fig. 13 indicates that Fe_2O_4 and Ni_2O_4 are highly oxidizing, and are unlikely to be stable in their stoichiometric configuration at room temperature. Co_2O_4 decomposes to $2/3(Co_3O_4 + O_2)$ at a temperature slightly above 100 °C. The Cr_2O_4 and Mn_2O_4 spinels are predicted to decompose to $Cr_2O_3 + 1/2O_2$ and $Mn_2O_3 + 1/2O_2$ at 285 °C and 342 °C, respectively. Since the Mn spinel exists as a metastable phase in some Li batteries, the Cr and Mn spinel phases should operate well at room temperature. Finally, the V_2O_4 and Ti_2O_4 spinels are predicted as fairly stable against O_2 release as indicated by their higher decomposition temperatures; 876 °C and 1646 °C, respectively. In summary, Ti_2O_4 , V_2O_4 , Cr_2O_4 and Mn_2O_4 are expected to exhibit superior

thermal stability against O₂ release among the considered spinel compounds. Comparing the calculated voltage (Fig. 10) and thermodynamic stability (Fig. 12), a stable discharged phase and unstable charged phase naturally lead to higher voltage, and *vice versa* (as expected). For example, fairly unstable Fe₂O₄ and Ni₂O₄ result in a higher voltage, while Mn₂O₄ generally results in lower voltages.

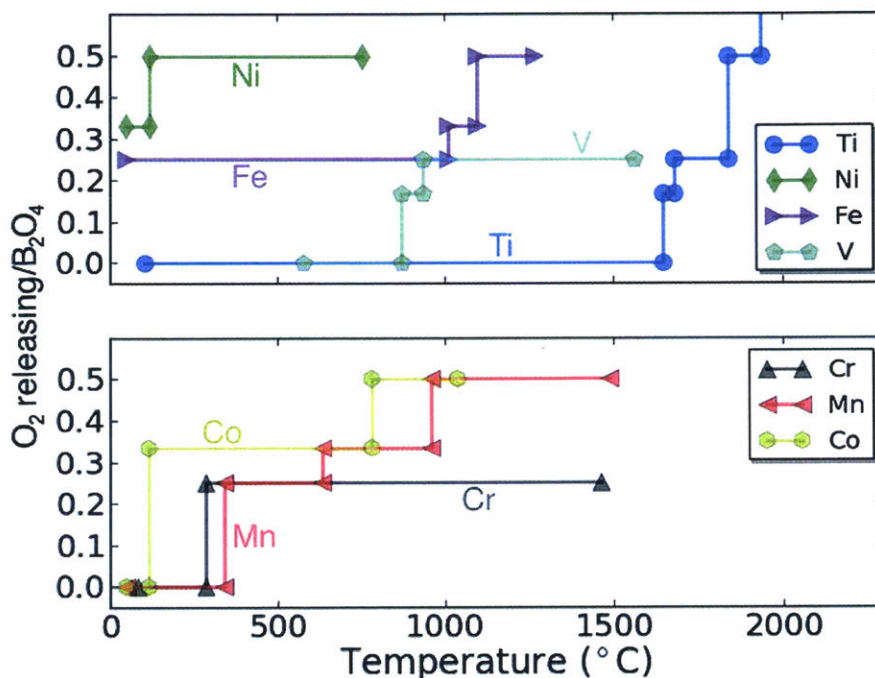


Fig. 13 The calculated thermodynamic O₂ evolution diagram of charged host spinel compounds as a function of temperature. The vertical axis denotes how much O₂ is predicted to be released from the compound per formula unit of B₂O₄ as the material decomposes.

The previous voltage, capacity and stability results for multivalent cathode materials show great potential to go beyond current Li-ion. However, a major remaining challenge is overcoming the sluggish diffusion expected for multivalent-ions. The slower diffusion of high-valent cations has been attributed to the stronger cation–anion interaction, which makes migrating 2+ or 3+ ions more difficult than moving 1+ ions, though no quantitative information is available on multi-valent

ion diffusion.¹⁶⁴ Hence, we calculate the migration energy barriers of the various multivalent ions ($A = \text{Mg}^{2+}$, Zn^{2+} , Ca^{2+} , Al^{3+} , and also Li^+ for comparison) in the spinel structure AB_2O_4 ($B = \text{Mn}$, Co , Ni , Cr) from first-principles as shown in Fig. 14. The Nudged Elastic Band method was used in both high vacancy limit and dilute vacancy limit corresponding a single migrating intercalant or a vacancy in an empty host or fully intercalated structure, showing the upper and lower limit of the intercalant migration activation barrier.

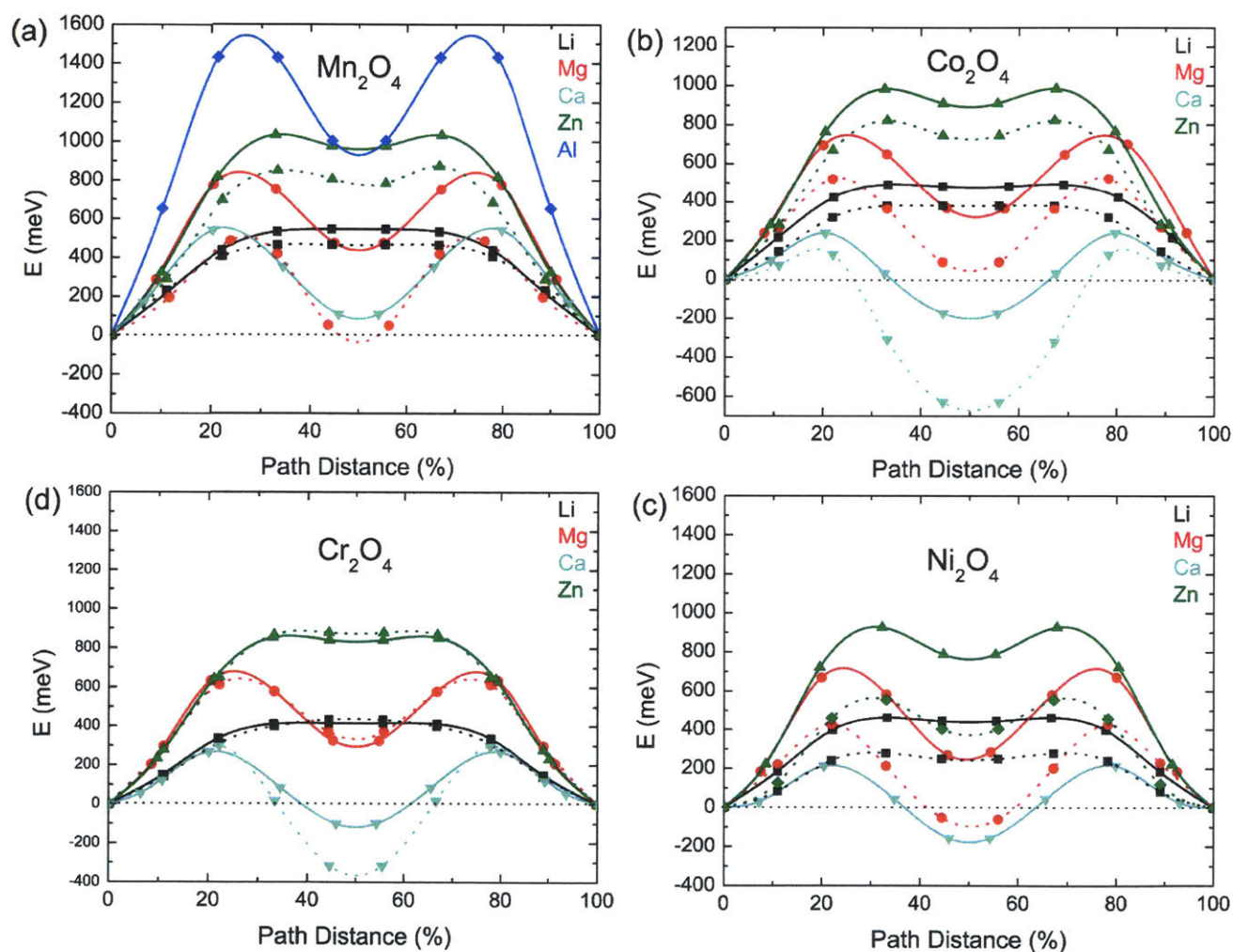


Fig. 14 Computed minimum energy paths for migration of different intercalants between the tetrahedral sites in the spinel B_2O_4 ($B = \text{Mn}$, Co , Ni , Cr) at the high vacancy limit (solid line) and dilute vacancy limit (dotted line), *i.e.* one mobile specie per supercell ($2 \times 2 \times 1$ of primitive cell).

In spinel Mn_2O_4 , which has been successfully commercialized for use in Li-ion batteries, Al^{3+} displays the highest diffusion barrier of ~ 1400 meV. Among the divalent cations, Zn^{2+} (~ 850 – 1000 meV) and Mg^{2+} (~ 600 – 800 meV) have the highest barriers, while Ca^{2+} is comparable to Li^+ (~ 400 – 600 meV). The migration barriers obtained for Li^+ in M_2O_4 ($\text{M} = \text{Mn}, \text{Co}, \text{Ni}, \text{Cr}$) all lie within ~ 400 to 600 meV in the empty lattice limit, in good agreement with first-principles Li mobility calculations performed by Bhattacharya *et al.* in the spinel $\text{Li}_{1+x}\text{Ti}_2\text{O}_4$ system ($-1 < x < 1$).¹⁸² Excluding the CrO_2 spinels and some of Ca-containing spinels, the migration barrier at high vacancy limit is always higher compared to the dilute vacancy limit, agreeing with Bhattacharya *et al.* that migration barrier is reduced by nearly 300 meV as Li is intercalated from the Li-deficient to the Li-rich limit (from ~ 600 meV for Li migration in Ti_2O_4 to ~ 300 meV for vacancy migration in LiTi_2O_4).¹⁸² From kinetic Monte Carlo simulations, the room temperature self-diffusivity of Li was shown to span $\sim 10^{-10}$ to 10^{-9} $\text{cm}^2 \text{s}^{-1}$ between $\text{Li}_{0.5}\text{Ti}_2\text{O}_4$ and LiTi_2O_4 , in good agreement with the excellent experimental rate-capability typically observed in Li spinel cathodes. Except in Mn_2O_4 , we could not converge the NEB for Al^{3+} due to the very large forces along the transition path, which is usually symptomatic of a very high barrier. The divalent barriers vary significantly with the chemical nature of the intercalant: Zn^{2+} (~ 800 – 1000 meV), Mg^{2+} (~ 600 – 800 meV), and Ca^{2+} (~ 200 – 500 meV). Although Ca^{2+} migration appears to be facile in our calculations, only in Mn_2O_4 does Ca^{2+} prefer to occupy the tetrahedral site as opposed to the octahedral site (which can be observed in Fig. 14 as the energy along the migration path becomes negative when Ca is near the octahedral site in the Ni, Cr, and Co spinel). For this case, the migration barrier should be measured as the energy increase from the octahedral site to the maximum along the path (see Fig. 14). We find that for all fully intercalated phases, the tetrahedral sites are more stable than the octahedral sites, which indicates a cross-over in site preference with concentration for some of the intercalating cations.

3.3 Discussion

Technical extrapolations of projected multivalent chemistries to the cell level have shown that multivalent intercalation is one of the few technologies that can outperform Li-ion batteries in terms of energy density. In this paper, we have used first principles calculations, well established in Li-cathode research,^{109, 164, 180, 183, 184} to evaluate the properties of multivalent-ion intercalation in spinel structures with different chemistries. We evaluated average insertion voltage, stability in the charged and discharged state, volume change upon intercalation, oxidation strength of the charged cathode, and the mobility of the multi-valent cations. Such first principles screening is important for this new field as multi-valent ion electrochemistry is not well established and, due to incompatibility between electrolytes and electrode materials, it can be difficult to obtain unambiguous experimental results on the performance of a specific cathode material.^{14, 185, 186} We found that the insertion voltage of Ca^{2+} , Mg^{2+} , Zn^{2+} , Al^{3+} and Y^{3+} against their respective metal anodes in general follows the electrochemical series but with quantitative variations due to the nature of the site preference of the intercalating ion. For example, Ca insertion voltages in spinels are lower than expected, as Ca in general prefers higher coordination than tetrahedral (commonly the most favorable site in the spinel structures). The Fe_2O_4 and Ni_2O_4 spinels are unlikely to function across the full capacity range due to the highly oxidizing and unstable nature of their fully charged states. As expected, Ti_2O_4 spinels have low insertion voltage for most intercalants, and in addition, are fairly unstable. The V_2O_4 and Cr_2O_4 spinels are also fairly unstable in the charged state, and the V spinel exhibits a low insertion voltage for all intercalants besides Mg and Ca. From the perspective of stability, the most promising spinel chemistry is Mn_2O_4 as it is stable in the charged state and fairly stable in the discharged state for several intercalating ions. Intercalant mobilities are generally low due to the high activation energies when transitioning between the tetrahedral and octahedral sites, though they are clearly not only controlled by charge. For

example, among the divalent ions Zn mobility is inferior to Mg, and Ca may have fairly good mobility in the spinel. Al^{3+} intercalation into the spinel structure can likely be excluded from consideration even though it has the peculiar feature that volume changes upon insertion are very small. The activation barrier for motion is very high for Al^{3+} in Mn_2O_4 and its discharged spinels are all highly unstable. Somewhat surprisingly, and in contrast to experimental claims,¹⁵⁰ we find that mobility of Zn in the spinel structure is very low, which in addition to its low insertion voltage, should exclude this system from further consideration for high energy density cathodes. The large intercalating ions such as Y^{3+} and Ca^{2+} are interesting, though the Y-spinels become unstable in the discharged limit. Both of these ions have reasonable insertion voltages and Ca^{2+} has better than expected migration barriers, due to its relative instability in the tetrahedral site. While this effect lowers the voltage from what would be expected by considering the electrochemical scale, it also seems to lower the migration barrier for motion. This may be similar to the more general principle that high energy defects in materials often have higher mobility.

Considering all computed properties, Mn_2O_4 spinels are particularly interesting due to their stability (Fig. 15). Among the divalent cations, both Mg^{2+} and Ca^{2+} may potentially be mobile in the spinel structure, warranting further experimental and computational investigation (particularly at small particle sizes). Mixed spinel structures may provide a further promising avenue, as the $\text{Ni}^{4+/3+}$ and $\text{Co}^{4+/3+}$ show higher voltage than the $\text{Mn}^{4+/3+}$ redox couple and compounds such as LiNiMnO_4 are known to combine higher operating voltage with a relatively stable charged state.¹⁴⁵

¹⁴⁶ Improving the diffusivity should be a focus for all multivalent cathode materials.

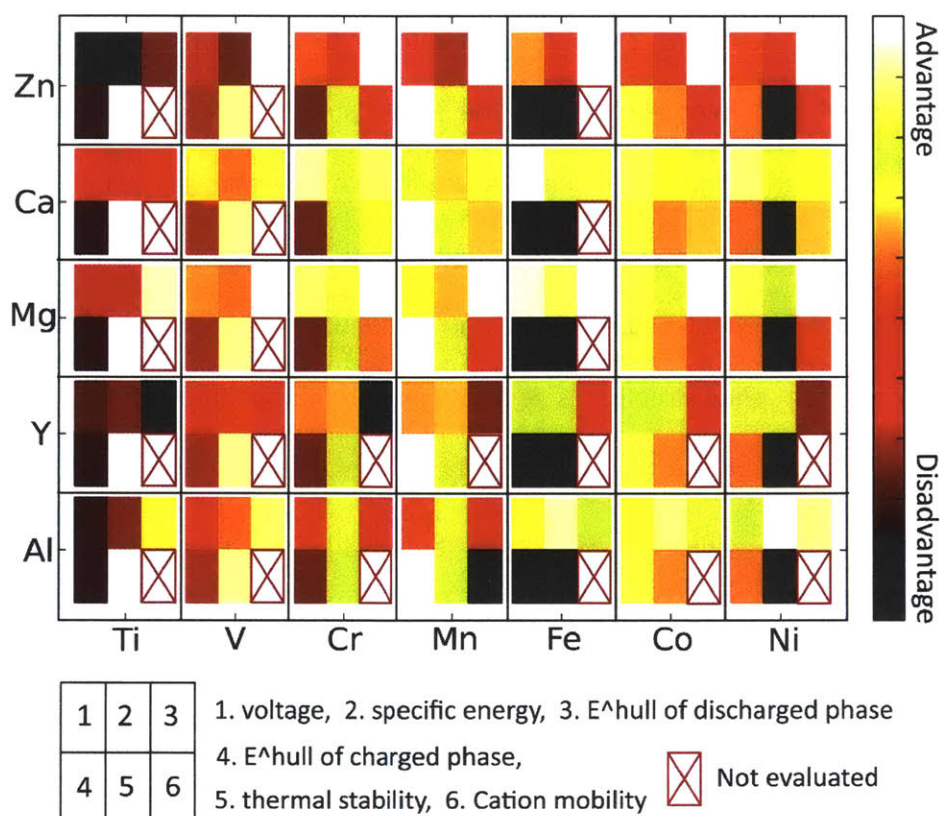


Fig. 15 Qualitative summary of multivalent spinel compounds based on multiple performance metrics, such as voltage, specific energy, thermodynamic stability of charged and discharged phases, thermal stability and intercalant mobility. The favorable (unfavorable) properties are represented with light (dark) color.

Finally, a concern with spinels, as with all intercalation materials, is the occurrence of cation disorder. In the extreme case, normal spinels can convert to inverse spinels with part of the transition metals on the tetrahedral site. While in more common layered materials, lowering of the intercalant mobility by cation disorder is well understood through the contraction of the interlayer slab space by disorder,⁶⁹ we are not aware of an equivalent study for spinels. Given the 3D and more rigid nature of the framework and the 3D diffusion network, one would expect spinels to be more tolerant to cation disorder. Nonetheless, we have performed a preliminary investigation into the driving force inverse spinel formation by adopting the same methodology as in Bhattacharya et

*al.*¹⁷² Based on small supercell calculations, we find that the normal spinel is always energetically favorable for Ca, Mg, Zn compounds. Further information can be obtained from the study of Burdett *et al.* who elucidated that cation disorder is strongly correlated to the relative size of the A and B ions.¹⁸⁷ Hence, Li and Zn prefer to form normal spinels, and we do not expect cation disorder. Ca is large and has the possibility to occupy octahedral sites that forms inverse spinel. Similarly, Mg may show cation site disorder for Ni, Fe, Co when synthesized at high temperature. However, in the case that well-ordered spinels cannot be formed at high temperature synthesis conditions, it may be still be possible to create the normal ordered spinel phase by chemical or electrochemical delithiation of the lithium spinels^{149, 151} and inserting multivalent cations.

In summary, in this chapter, we have performed systematic calculations to screen for and discover improved multivalent cathode materials using the spinel structure as a general host. On the basis of all property calculations, the spinel Mn_2O_4 is found to be a superior candidate with Ca^{2+} and possibly Mg^{2+} as mobile cations. It is our hope that our work provides a general guide and standard for future theoretical as well as experimental multivalent cathode development and design.

Chapter 4. Evaluation of sulfur spinel compounds for multivalent battery cathode applications

4.1 Motivation

We note that one recent experimental work demonstrated highly reversible and extensive intercalation of Mg into the tetrahedral sites of Mn_2O_4 spinel, but only achieved a low degree of intercalation (3 at% Mg in the discharged state) when paired with a non-aqueous electrolyte,^{188, 189} consistent with the kinetic limitations predicted by theory (activation barrier of ~800 meV in

cation dilute limit).¹⁹⁰ Indeed, one might intuitively expect that the multivalent elements, due to their higher charge compared to Li^+ , will form stronger bonds with the oxygen anion lattice and will hence generally exhibit larger activation barriers for ionic mobility. However, recent work compared the mobility of multivalent intercalating ions in several different oxide frameworks and found the diffusion barrier to be highly dependent on the intercalant site preference to the diffusion path topology of the host structure.¹²⁴ Thus, tailoring the structure carefully to the migrating ion size and electronic structure provides one of the most important controls for mobility. Another design control can be leveraged by tuning of the chemistry rather than the structure. In contrast to oxide materials, previous findings hint that sulfides may exhibit improved Mg ion diffusivity. Aurbach *et al.* reversibly inserted Mg into the anionic framework of Chevrel Mo_6S_8 , obtaining a capacity of $\sim 70 \text{ mA h g}^{-1}$ for more than 600 cycles.¹ Liang *et al.* reported that highly exfoliated graphene-like MoS_2 accompanied by a nano-sized Mg anode can deliver $\sim 170 \text{ mA h g}^{-1}$ capacity and 1.8 V voltage for over 50 cycles.¹⁹¹ Furthermore, the Mg^{2+} ionic conductivity can be optimized with the expanded interlayer spacing.¹⁹² In addition, Tao *et al.* demonstrated reversible Mg intercalation/deintercalation in TiS_2 with tube morphology.¹⁹³ Recent theoretical work predicts low Mg mobility, in spinel and layered O1 type TiS_2 (barriers corresponding to 860 meV and 1160 meV, respectively), but suggests that strain engineering could be used to enable more facile Mg intercalation.⁹⁰ Motivated by the above-mentioned studies of sulfides, we here systematically evaluate 21 sulfur spinel compounds to uncover their potential for multivalent cathode applications and compare these properties against those previously obtained for oxides. It is expected that the set will exhibit lower voltage as compared to the oxide counterparts, however, the goal of our work is to evaluate the benefits as well as drawbacks in tuning chemistry through the anion framework as well as to suggest improved cathodes as compared to the Chevrel phase. Properties such as insertion voltage, capacity, stability and intercalant mobility are evaluated to

help select the most promising candidate materials for experimental synthesis and characterization. Moreover, we uncover the general trend and diffusion mechanism in this category of compounds, and provide a guide for future material synthesis and design.

4.2 Structure, Voltages, Capacities, NEBs, etc.

Spinel compounds belong to space group $Fd\bar{3}m$ with the general formula AB_2X_4 . The anion 'X' can be oxygen to form oxide spinels or divalent S or Se ions to form thiospinels. Within the spinel crystal structure, the cation 'B' is octahedrally coordinated by anion X, and these octahedra share edges and extend in space such that there exist 3D diffusion channels (Fig. 16). In a normal spinel, cation 'A' occupies the tetrahedral sites to form the $Fd\bar{3}m$ symmetry.^{143, 194} Apart from the tetrahedral site that is occupied by cation 'A', there also exist face-sharing octahedral sites located between the tetrahedral sites. In some materials, cation 'A' occupies these octahedral sites rather than the typical tetrahedral sites, either due to the 'A' cation naturally favoring an octahedral environment or due to limited availability of tetrahedral sites when the concentration of 'A' is high. In this case, the crystal structure can be categorized into a rocksalt-like geometry belonging to space group $Imma$ as shown in Fig. 16(b).^{182, 195} For example, Ca prefers octahedral sites in Mn_2O_4 host structures;¹⁹⁰ and excessive intercalation of Li ions into Mn_2O_4 spinel host will also push the tetrahedral Li into the octahedral sites and form rocksalt $LiMnO_2$.¹⁹⁶ The diffusion path for the 'A' cation alternates through tetrahedral and octahedral sites along zigzag-shaped paths as illustrated in Fig. 16(c).¹²⁴ In this paper, we systematically evaluate the performance of sulfur spinels (formula AB_2S_4) as multivalent cathode materials, selecting 'A' atoms from the set {Mg, Ca, Zn} and 'B' atoms as redox-active 3d transition metals from set {Ti, V, Cr, Mn, Fe, Co, Ni}, totaling 21 combinations.

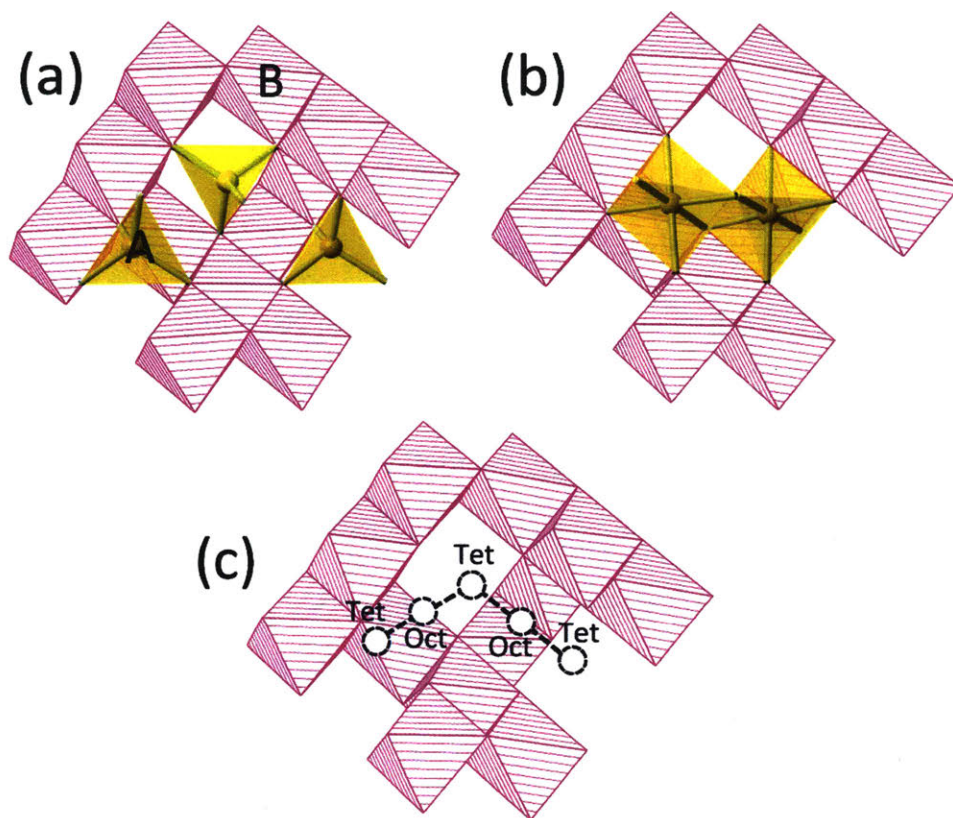


Fig. 16 In AB_2X_4 spinel crystal structures, the 'A' atom (yellow polyhedra) can occupy either the (a) tetrahedral site or (b) octahedral site. When the 'A' atom diffuses through the spinel host structure framework (pink octahedrons built with 'B' and S atoms), it alternates between the tetrahedral site and octahedral site along a (c) zigzag energy minimum path.

First, we evaluated the thermodynamic stability of compounds within the sulfur spinel family. The thermodynamic stability of a material is defined as the driving force to decompose a compound into a combination of the most stable compounds in its corresponding chemical system. To determine the appropriate set of stable compounds for comparison as well as their energies, we combine our first-principles calculation results with the comprehensive data available in the Materials Project.¹⁵⁷ The thermodynamic stability of a target spinel phase was estimated by comparing its formation energy against the convex hull of ground state energies in the relevant

portion of the phase diagram, which represents the driving force for decomposition and which we refer to as “energy above hull”.¹⁶²⁻¹⁶⁴ A high energy above hull indicates that a material is thermodynamically unstable, and serves as an indicator for synthesizability as well as the likelihood for degradation upon cycling.¹⁹⁷

Fig. 17 plots the energy above hull for fully discharged and fully charged phases for each compound in sulfur spinel family. The thermodynamic stability results suggest that both Ti_2S_4 and Mn_2S_4 spinel structures represent relatively stable empty hosts for cation intercalation. The three compounds V_2S_4 , Cr_2S_4 and Ni_2S_4 , exhibit moderate energy above hull values of approximately 70 meV per atom, and are less stable than the Ti- and Mn-containing phases but still within the energy scale of common metastable compounds. Amongst the 21 compounds, in the discharged phase, ACr_2S_4 and ATi_2S_4 are the most stable compounds with $A = \{Ca, Mg, Zn\}$. $MgCr_2S_4$ and $ZnCr_2S_4$ possessing the lowest energy above hull and hence are likely accessible through direct synthesis. $MgMn_2S_4$ and $MgTi_2S_4$ spinel in the discharged phase have fairly low above hull energies as well, whereas both V_2S_4 and Fe_2S_4 spinel compounds fall into the unstable range with large above hull energies (>85 meV per atom, *cf.* Fig. 17).

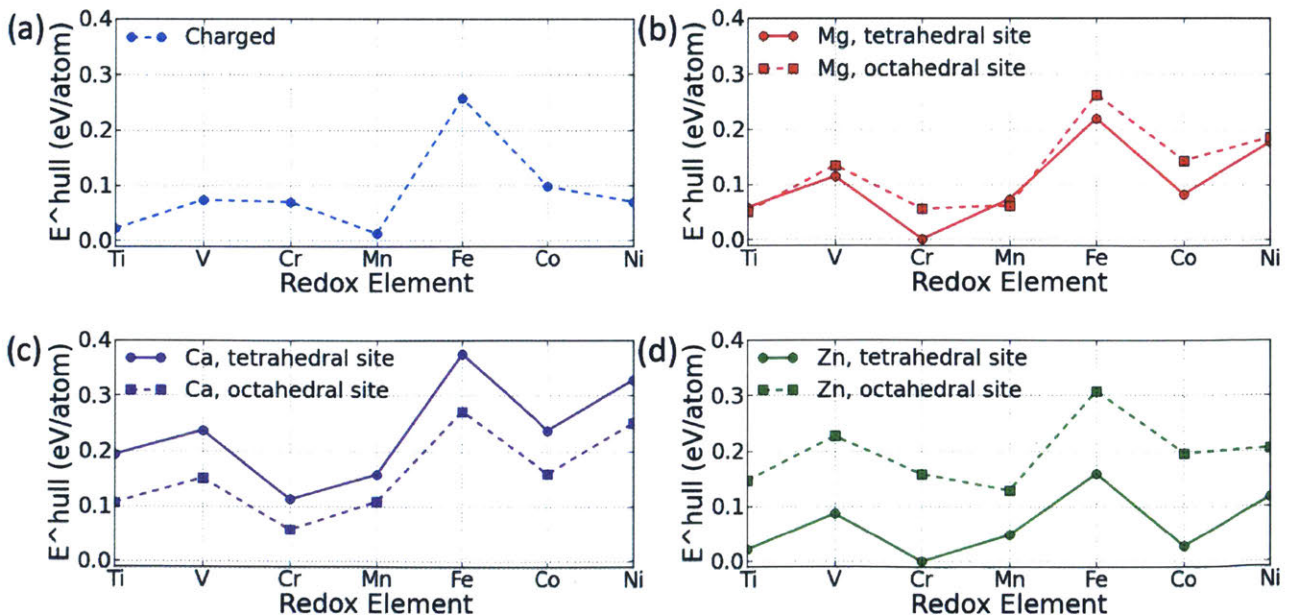


Fig. 17 The calculated thermodynamic stabilities of sulfur spinel compounds in the (a) charged and (b–d) discharged phases. The energy above hull is measured as the formation energy difference between a compound and the convex hull formed by stable compounds. The distance between the dashed and solid lines indicate site energy preferences for the cation in the discharged state.

A priori it is unknown whether a cation 'A' in AB_2S_4 spinels occupies the tetrahedral or the octahedral site, wherefore we evaluated the thermodynamic stabilities for both situations. Site preference is assessed by placing the multivalent intercalant 'A' = {Ca, Mg, Zn} on either the tetrahedral or octahedral sites and evaluating the difference in energy. These site energy differences are plotted in Fig. 17 as a function of chemistry. Both the size and electronic structure can affect the A cation's site preference. Ca compounds normally prefer the rocksalt-type structure in which they are octahedrally coordinated. The site energy difference is approximately 500 meV for Mn_2S_4 and Cr_2S_4 and approximately 600–650 meV for other compounds. In sulfur spinels, the preference of octahedral sites for the Ca^{2+} ion is due to its larger ionic size in accordance with Pauling's rule.¹⁹⁸ Mg^{2+} has a smaller ionic size relative to Ca^{2+} , and the ratio between the Mg^{2+} and S^{2-} ionic radii is ~ 0.4 , falling into a range that favors both octahedral and tetrahedral environments.¹⁹⁸ Therefore, amongst the intercalant species {Ca, Mg, Zn}, Mg is the most flexible in terms of cation site preference and displays the smallest site energy difference. In $MgMn_2S_4$ and $MgTi_2S_4$, the site energies for Mg between the two types of sites are almost equal, although for $MgCr_2S_4$ and $MgCo_2S_4$ there is a stronger preference for the tetrahedral site (which is ~ 400 meV and ~ 500 meV lower than octahedral site, respectively). At compositions AB_2X_4 , for octahedral A cations only half of the sites are filled and hence, there is a choice of which sites to occupy. We investigated nine different randomly chosen, but evenly distributed, Mg cations among the available octahedral sites in TiS_2 , as a representative case. We estimate that the choice of

octahedral site configuration may modify the site energy by less than ~20 meV, which is obtained from an extensive investigation of the Mg site energies for both octahedral and tetrahedral site configurations in TiS_2 .⁸⁹ The Zn^{2+} ion generally prefers tetrahedral sites as exhibited by the ~1050 meV (calculated from ~150 meV per atom E above hull energy) difference in stability as compared to the rocksalt-like phase. Zn prefers four-coordinated tetrahedral environments¹⁹⁹ because the Zn^{2+} ion, with an electronic structure of $[\text{Ar}]3d^{35}$, has ten electrons outside the argon shell that completely fill the 3d orbitals, leaving only the empty 4s and 4p orbitals to form sp^3 hybridization. In the rest of our work, we adopt the most stable site for the respective mobile cation in the discharged state.

In addition to determining structure and stability, the cation site preferences can be related to cation mobility. The diffusion path in spinel structures traverses the tetrahedral as well as the octahedral sites;¹²⁴ thus, the energy difference represents a minimum value for the activation barrier and low site energy differences indicate higher cation mobility. For example, Zn-containing compounds are not preferred because a 1050 meV site energy difference implies a migration energy barrier of at least 1050 meV. Therefore, we focus our attention to compounds with low site energy differences to maximize the chance of finding a host enabling facile MV ion diffusion.

Combining the assessments of thermodynamic stability and the minimum activation barriers of sulfur spinels, Cr_2S_4 , Ti_2S_4 and Mn_2S_4 emerge as the top three candidates. To obtain more accurate diffusion activation barriers for these materials, we performed nudged elastic band (NEB) calculations to compute the energy along the migration path for Cr_2S_4 , Ti_2S_4 and Mn_2S_4 in the limit of dilute cation insertion (Fig. 18). Compounds that exhibit reasonable cation mobility under these assumptions include: Mg in Mn_2S_4 (515 meV), Ca in Cr_2S_4 (542 meV), Mg in Cr_2S_4 (567 meV), and Mg in Ti_2S_4 (615 meV). Other combinations exhibit much larger activation barriers, up to ~1500 meV for Zn^{2+} migration in Cr_2S_4 . We note that these findings are in very good qualitative

agreement with the estimations based only on site energy difference (Fig. 18(d)). While the site energy differences do not fully determine the migration barrier, one can use it as an indicator to screen out compounds based on a lower estimate of the activation energy. In particular, the activation energy barrier in spinels equals the site energy difference plus the additional energy needed for the cation to pass through an intermediate transition state composed of a narrow, triangular aperture of three sulfur atoms. This intermediate state corresponds to the two activation barrier maxima at the ~25% and ~75% points along the diffusion path in Fig. 18(a-c).¹²⁴ The variable energy in passing through this triangle aperture adds an additional energy cost of ~0–600 meV, and elevates the activation barrier for compounds which exhibit small site energy differences [Fig. 18(d)].

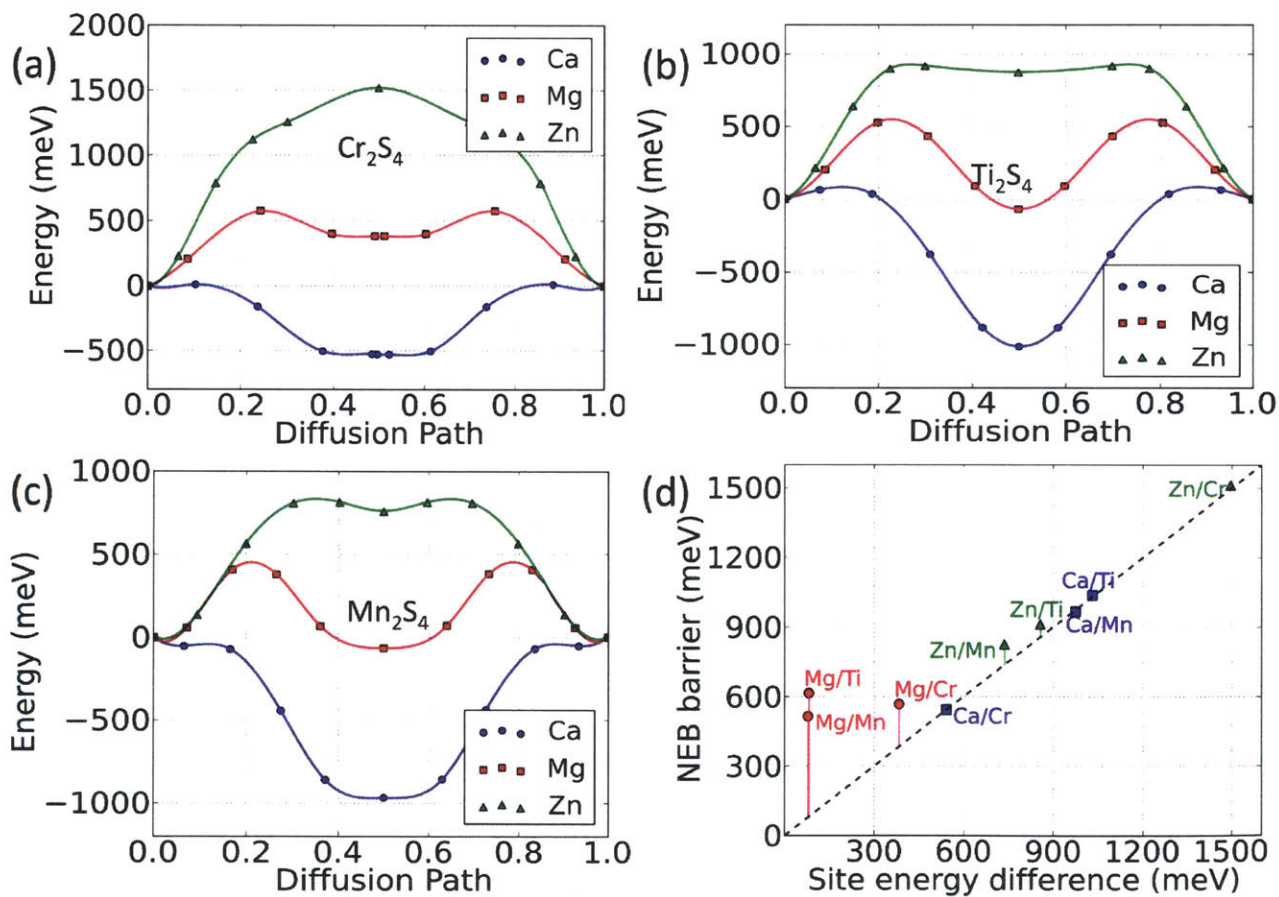


Fig. 18 Calculated energy barrier for migration of ‘A’ cation in spinel along the minimum energy path as obtained by first-principles nudged elastic band (NEB) in calculations. (a) Cr_2S_4 , (b) Ti_2S_4 and (c) Mn_2S_4 within dilute limit of cation insertion. (d) The correlation between site energy difference of the cation (see Fig. 17) and the NEB migration barrier.

In addition to stability and diffusion, we plot in Fig. 19(a) the calculated average voltage vs. the gravimetric capacity for the full intercalation reaction of $\text{B}_2\text{S}_4 + \text{A} \rightarrow \text{AB}_2\text{S}_4$ for the intercalants $\text{A} = \{\text{Mg}, \text{Ca}, \text{Zn}, \text{Y}, \text{Al}\}$ and redox active transition metals $\text{B} = \{\text{Ti}, \text{V}, \text{Cr}, \text{Mn}, \text{Fe}, \text{Co}, \text{Ni}\}$. We find, not surprisingly, that the average voltage of sulfur spinels is significantly lower than that of oxide spinels; for example, Ca intercalation in oxides occurs in a range of 2.7–4.0 V (excluding Ti_2O_4 , which has an average voltage of 1.5 V),¹⁹⁰ whereas the average voltages of non-Ti sulfur spinel compounds fall in the range of 1.2–2.0 V. Similarly, Mg and Zn intercalation in sulfide spinels occurs at approximately 1.5 V below their oxide counterparts. This is consistent with the effect of the anion potential on Li-insertion reactions clarified in early first-principles work on lithium cathodes.¹⁶¹

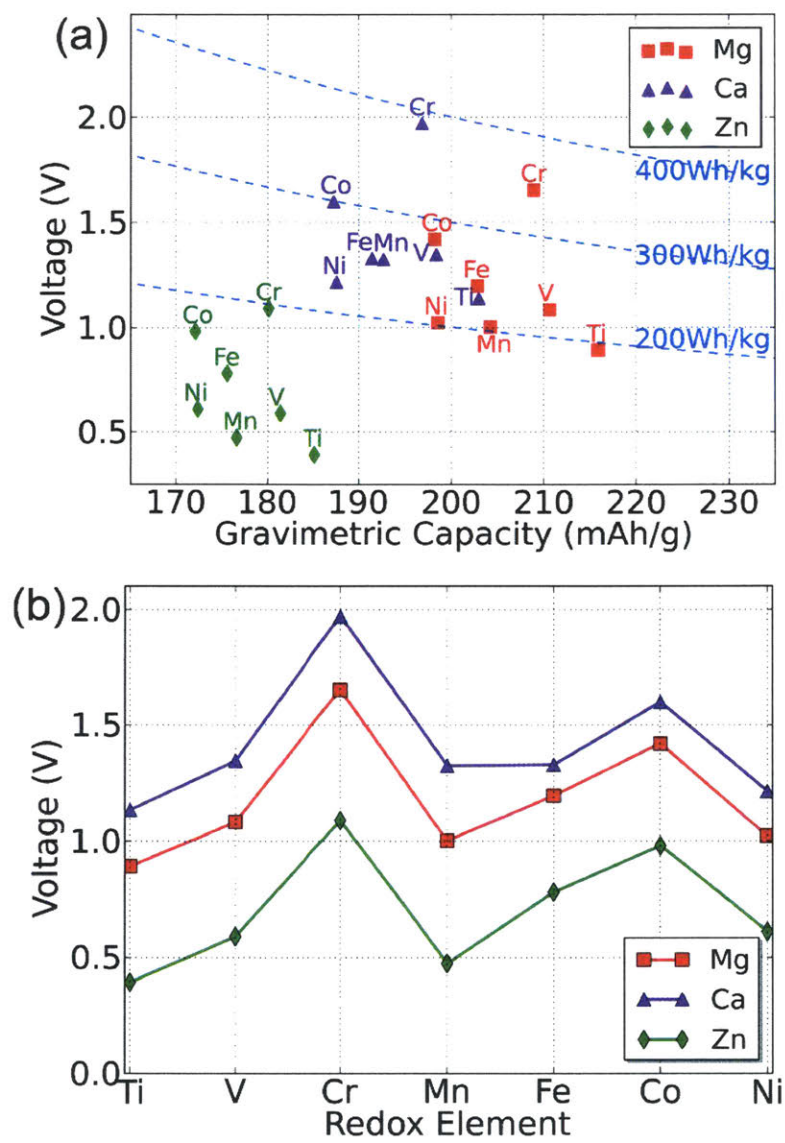


Fig. 19 (a) The calculated average voltage vs. gravimetric capacity for intercalation of 'A' = {Zn, Ca, Mg} in B_2S_4 spinels up to composition AB_2S_4 . The redox-active metal is marked next to each point for clarification. Dashed curves are plotted to mark the specific energy of 200 W h kg^{-1} , 300 W h kg^{-1} and 400 W h kg^{-1} as reference values, respectively. (b) The calculated voltage of each spinel phase as a function of the redox-active transition metal and intercalating cation. The different colors denote different intercalating species as specified by the legend.

The detailed variation of intercalation voltage *versus* redox metal species is plotted in Fig. 19(b). The differences in voltage between insertion cations stay roughly constant regardless of the redox metal choice: Ca intercalation occurs ~0.2 V higher than that of Mg, and Mg intercalation occurs ~0.5 V higher than that of Zn. This voltage trend is consistent with, but less pronounced than, the aqueous electrochemical series of {Ca, Mg, Zn}, *i.e.*, $E_{\text{Ca(aq)}}^0 = -2.86 \text{ V}$, $E_{\text{Mg(aq)}}^0 = -2.37 \text{ V}$ and $E_{\text{Zn(aq)}}^0 = -0.76 \text{ V}$. Similarly, regardless of the choice of active cation {Mg, Ca, Zn}, the qualitative trend *versus* redox element follows a similar pattern: Cr₂S₄ host structures provide the maximum voltage and Ti₂S₄, Mn₂S₄ and Ni₂S₄ exhibit relatively lower voltage. The voltage profile of the sulfide spinels can be related to the corresponding change in electronic configuration between the charged and discharged states. For example, Cr exhibits a high voltage because the discharged state, Cr³⁺, has a very stable electronic configuration (d³, corresponding to half-filled t_{2g} orbitals) whereas the charged state, Cr⁴⁺, has an unstable electronic configuration (d², which tends to oxidize further to d⁰, corresponding to Cr⁶⁺). Conversely, the “low voltage” metals exhibit more stable electronic configurations in the charged state. For example, Ti⁴⁺, Mn⁴⁺ and Ni⁴⁺ are very stable, containing, respectively, d⁰, half-filled and filled t_{2g} states. In these instances, intercalation adds an electron that results in a less stable electronic arrangement for the host metal, sometimes (in the case of Ni and perhaps Mn) filling an antibonding orbital, which results in decreased stability.

In addition to the lower voltage, the gravimetric capacities of sulfur spinel compounds are approximately 30% lower than their oxide counterparts due to the added mass of the S ion. Considering the reductions in both voltage and capacity, the specific energy of the sulfur spinel compounds is on the order of ~400 W h kg⁻¹. However, it is possible that sulfur-based compounds, with their improved intrinsic bulk cation mobility and less need (presumably) for electronically conductive coatings, could achieve a higher fraction of their theoretical energy density, and thus

higher practical energy densities. It should also be noted that such systems represent potentially better performance than that demonstrated from the Chevrel phase,¹³ which is often taken as a point of reference for multivalent cathode compounds as the only to date known cathode which reversibly cycles Mg at room temperature.¹³

Considering all the properties evaluated (Table 1), Mg or Ca in a Cr₂S₄ spinel host are found to be the most promising cathode materials due to their good mobility and acceptable voltage. Mg in Mn₂S₄ and Ti₂S₄ may also be worthwhile systems to study on the basis of the favorable cation mobility.

Table 1 Properties of selected multivalent sulfur spinel systems

Spinel materials	Stable 'A' site	Voltage (V)	Capacity (mA h g⁻¹)	Diffusion barrier (meV)
Mg in Cr ₂ S ₄	Tet	1.65	209	542
Mg in Ti ₂ S ₄	Oct	0.89	216	615
Mg in Mn ₂ S ₄	Oct	1.00	204	515
Ca in Cr ₂ S ₄	Oct	2.16	197	567

4.3 Discussion

In this chapter, we used first-principles calculations to evaluate the electrochemical properties of multivalent intercalation in sulfur spinel compounds. To exemplify our approach, we include a comparison between our DFT calculations and available experimental results for verified Mg intercalation in Table 2. Here we also include new benchmarking results on the Chevrel Mo₆S₈ phase (see Methodology section) which demonstrates a very low migration barrier of 360

meV for Mg^{2+} in the dilute (charge) cation limit, in agreement with its demonstrated excellent intercalating properties as shown by the Aurbach group.¹³

Table 2 Comparison between theory and experiment from previous studies. The DFT evaluated properties are in good agreement with experimental values vs. Mg^{2+}/Mg^0

Material system	Average voltage (theory)	Average voltage (expt.)	Migration activation energy (theory)	Migration activation energy (expt.)
Spinel MnO_2	2.86 V ¹⁹⁰	2.9 V ¹²⁴	650–850 meV ¹⁹⁰	Impeded ¹⁸⁸
Spinel TiS_2	0.89 V (this thesis)	1.2 V ⁸⁹	615 meV (this thesis)	550 meV ⁸⁹
Chevrel Mo_6S_8	0.99 V	1–1.3 ^{13, 55}	~360 meV (this thesis) ~500 meV ⁵⁵	Operable C/8 ¹³

Based on our evaluations of compound stability, cation activation energy, voltage and capacity, $MgCr_2S_4$, $MgTi_2S_4$, $MgMn_2S_4$ and $CaCr_2S_4$ spinel compounds hold the most promise for multivalent cathode applications amongst the 3d transition-metal sulfur spinel compounds. The calculation method we adopt has been proven to be reliable for evaluating electrochemical intercalation in Mn oxide spinel^{188, 190} and Chevrel Mo_6S_8 (see benchmark calculations in the Methodology section)⁵⁵ and most recently in thiospinel TiS_2 ⁸⁹ (see Table 2).

We identified several combinations of active cation and redox metal ions that exhibit excellent thermodynamic stability in both the fully charged as well as the fully discharged states. Furthermore, in the sulfur spinel structure, we found that Zn tends to prefer tetrahedral sites, Ca tends to prefer octahedral sites, and Mg shows similar preference for octahedral and tetrahedral sites. These results, which are related to the electronic configuration of the active cations and their ionic radii, not only determine the preferred cation sites, but also set bounds on the intrinsic mobility of the different host/intercalant combinations. Our results indicate that for the spinel

structure, it is feasible to filter out materials with poor cation mobility using site energies alone. However, to identify compounds with promising cation mobility the minimum energy along the diffusion paths needs to be evaluated. Activation barrier calculations using the nudged elastic band method found four compounds with acceptable cation mobility: MgTi_2S_4 , MgCr_2S_4 , MgMn_2S_4 , and CaCr_2S_4 . It is noticeable that there is a distinctive difference between this work and a recent report by Emly *et al.*⁹⁰ regarding the activation energy barrier for Mg diffusion in Ti_2S_4 at dilute concentrations, e.g. ~600 meV reported here as compared to 860 meV⁹⁰. We believe that the discrepancy is primarily caused by the difference in equilibrium lattice parameter used in the NEB calculations – in this work, the relaxed discharged material (e.g. the calculation cell is relaxed with intercalant) is employed in the NEB calculations instead of the using that of the end member (empty) charged structure. Indeed, Emly *et al.* finds that the activation energy can be dramatically modified by the volume change⁹⁰ and even a small amount of well-distributed cations can expand the volume of host significantly. Hence, our results are actually in good agreement with Emly *et al.* considering the effect of the intercalant-induced volume expansion. Although our calculations indicate that sulfides may be advantageous compared to oxides in terms of diffusivity, sulfur spinel compounds exhibit lower intercalation voltages by more than 2 V and lower gravimetric capacity. For a particular intercalant, the choice of redox metal affects the voltage by ~0–0.7 V, which can largely be explained by considering the electron configuration of the transition metal. The low voltage of this series of compounds also hints at a possible platform for batteries with aqueous electrolytes, although we anticipate that stability of sulfides in an aqueous environment would present additional challenges.²⁰⁰

In general, intercalant mobility is mainly determined by three factors: (1) connectivity between sites; (2) sizes of the diffusion channel/cavity and intercalant; (3) and interaction strength between the intercalant and host structure. The site connectivity divide cathode materials into 1D,

2D or 3D intercalation topology, which in turn affects the diffusion behavior of a material dramatically as, in principle, a well-distributed diffusion network should facilitate mobility by providing improved tolerance towards defects and changes in lattice parameters.^{201, 202} Moreover, the channel size should be large enough to accommodate the intercalant. Finally, high mobility is facilitated by weak interaction between the intercalant and host anion lattice. In sulfide spinels, the 3D diffusion channels and expanded volume (the latter as compared to oxide spinels), at least the first two criteria are satisfied. Meanwhile, the ionic interaction between intercalant and host framework is likely reduced considering the longer 'A'-S bond (than 'A'-O bond) and the lower electronegativity of S^{2-} as compared to O^{2-} . Hence, for sulfide systems, we surmise that facilitated intercalant mobility can be achieved through (i) a weakening of ionic bonds between the migrant ions and the host structure and (ii) a moderate increase of diffusion channel size. Our systematic study allows for a rigorous quantification in the gain in mobility going from S^{2-} instead of O^{2-} , for the same structure. Indeed, comparing the Mg activation barriers across the different transition metal cations in our previous oxide spinel work² to the results presented here, we find an average ~200 meV reduction in ionic barrier, which is equivalent to ~4 orders of magnitude improvement in bulk diffusion coefficient. Beyond tuning the majority anion species, we speculate that incorporating mono-valent anions to reduce the electrostatic interaction between intercalant and host could possibly improve the intercalant cation mobility. For example, theoretical calculations predict that partially substituting the O atom with F in one corner of "transition metal-oxygen" octahedron improves the Mg ion mobility for both VPO_4F and $FeSO_4F$.^{90, 203} Polyanionic compounds might lead to good mobility as well, as those materials generally present a more covalent bonding framework with weaker electrostatic interactions between the host and the mobile cation.

In addition to these considerations the availability of fresh Mg near the electrode is greatly influenced by process of Mg desolvation from the bulk electrolyte followed by surface diffusion, and thus might dominate Mg bulk diffusion.^{5,10,11} Previous investigation demonstrated the formation of “sturdy” ionic-couples in the electrolyte bulk and Mg desolvation energies of a multitude of electrolyte species, suggesting that the availability of fresh Mg at the surface electrodes can be largely impacted by not negligible desolvation energies^{31, 35, 189} proposed a desolvation mechanism of Mg electrolyte in proximity of a sulfide Chevrel cathode surface, discussing various mechanisms behind the transport of Mg from the electrode surfaces in the bulk. Wan *et al.*⁵⁵ estimated that the migration of incoming Mg-Cl⁺ units from the bulk electrolyte to the surface and later into the Chevrel bulk as Mg ions only cost ~0.5 eV, hence not limiting Mg availability in the cathode bulk but manifesting *via* not negligible intercalation over-potentials at the interface.

From the synthesis viewpoint, previous research indicates that the Cr₂S₄ normal spinel framework can be prepared from their cupric compounds²⁰⁴ by electrochemical removal or ion exchange of copper in certain concentration regions.²⁰⁵ Normal spinel-type Mg_xTi₂S₄ (0 < x < 0.5) can also be synthesized *via* Mg intercalation into the cubic Ti₂S₄.⁹³ Indeed, recent collaborative work⁸⁹ has demonstrated that the thiospinel Ti₂S₄ shows promise as a cathode material for Mg batteries, yielding a high capacity of 195 mA h g⁻¹ at an average voltage of 1.2 V at 60 °C. According to our calculations, the low energy above hull of spinel LiMn₂S₄ (~30 meV per atom) suggests that ion exchange from the Li version could present another possible avenue for synthesis. Thus, it should be possible to test multivalent intercalation for the specific hosts identified from our computational results.

Chapter 5 Materials Design Rules for Multivalent Ion

Mobility in Intercalation Structures

5.1 Motivation

In this chapter, we focus on understanding and charting the challenge posed by creating cathode host structures with sufficient MV cation mobility required for reversible intercalation at reasonable rates. Indeed, the expectation is that the higher charge of MV cations will polarize the host environment, thereby reducing mobility and rate capability of MV chemistries. While for Li^+ intercalation both extensive experimental⁶⁴⁻⁶⁶ and theoretical⁶⁷⁻⁷² Li mobility data are readily available, the lack of reliable electrochemical MV test vehicles^{14, 25} and limited exploration of MV chemistries and host structures^{206, 207} have made it difficult to understand what controls MV ion mobility. Note that reasonable diffusivity is a required condition for cathode materials but does not guarantee the absence of other potential rate-limiting factors (such as phase transformation or electronic conductivity). Therefore, the objective of this chapter is to chart the mobility of MV cations in oxide hosts, establish useful guidelines to identify high mobility cathodes, and as such get a better perspective on the feasibility of intercalation-based rechargeable batteries with very high energy density.

In such complex situations, *ab initio* computing has advantages, as it can isolate distinct physical phenomena and quantitatively assess their thermodynamics and kinetics, which facilitates the identification of the specific structural and chemical features that determine materials properties. Driven by the important role of cation diffusion in geological processes and several technological applications in addition to batteries, phenomenological^{207, 208} and empirical^{124, 209-211} models have been developed highlighting factors such as crystal porosity or crystal “openness”, electrostatic site energy, and ionic radius of the diffusing species. In this work, we take a

significant step forward by harnessing the quantitative accuracy afforded by density functional theory (DFT) nudged elastic band (NEB) simulations^{139, 141, 212} to gain deeper insights and arrive at a simple, quantitative recipe for screening compounds and structures. While the NEB method has been applied successfully to address Li diffusion in a multitude of cathode materials providing notable scientific insights,^{167, 168, 213-216} in this chapter, we extend NEB predictive capabilities to explore the unpaved territory of MV ion migration in selected cathode materials.

In detail, we investigate the migration of MV ions (Mg^{2+} , Zn^{2+} , Ca^{2+} , and Al^{3+}) in four well-known Li-ion intercalation host structures: spinel Mn_2O_4 , olivine FePO_4 , layered NiO_2 , and orthorhombic $\delta\text{-V}_2\text{O}_5$. Variants of the first three chemistries have proven to be commercially viable as active cathode materials in Li-ion batteries, and spinel Mn_2O_4 as well as orthorhombic $\delta\text{-V}_2\text{O}_5$ is among the few insertion chemistries known to reversibly intercalate MV ions (along with Chevrel Mo_6S_8 and layered MoO_3).^{13, 58, 124, 217, 218} Moreover, we focus not only on evaluating the suitability of these candidate MV cathode materials on the basis of mobility considerations, but also on identifying the general structural and chemical descriptors that will allow for new MV ion conducting cathode materials to be identified. We find that while the mobility of MV ions is consistently lower than Li^+ , the barrier of different +2 ions depends very strongly on the structure such that the optimal structure for each intercalating ion is different. Indeed, our findings indicate that a structure that has reasonable mobility for one divalent ion may be terrible for another divalent ion. However, clear design guidelines can be established by pairing the diffusion topology of a structure with the site preference of each intercalant.

5.2 Discussions

First-principles migration energies are computed using DFT with NEB^{136, 219}. The migration energies along the diffusion paths in the charged state are shown as solid lines in Figure 20 for (a) spinel Mn_2O_4 , (b) olivine FePO_4 , and (c) layered NiO_2 , with a summary of the migration

barriers E_m (e.g., the maximum energy along the path) shown as solid bars in Figure 20, panel d. Note that in these plots, the energies of the intercalation sites (beginning and end points of the path) have been arbitrarily set to zero and the path length normalized to 100% in the x-axis. For adequate battery operation, we quantitatively estimate that E_m can be at most ~525 meV when using a micron-sized particle and ~650 meV in a nanosized particle.

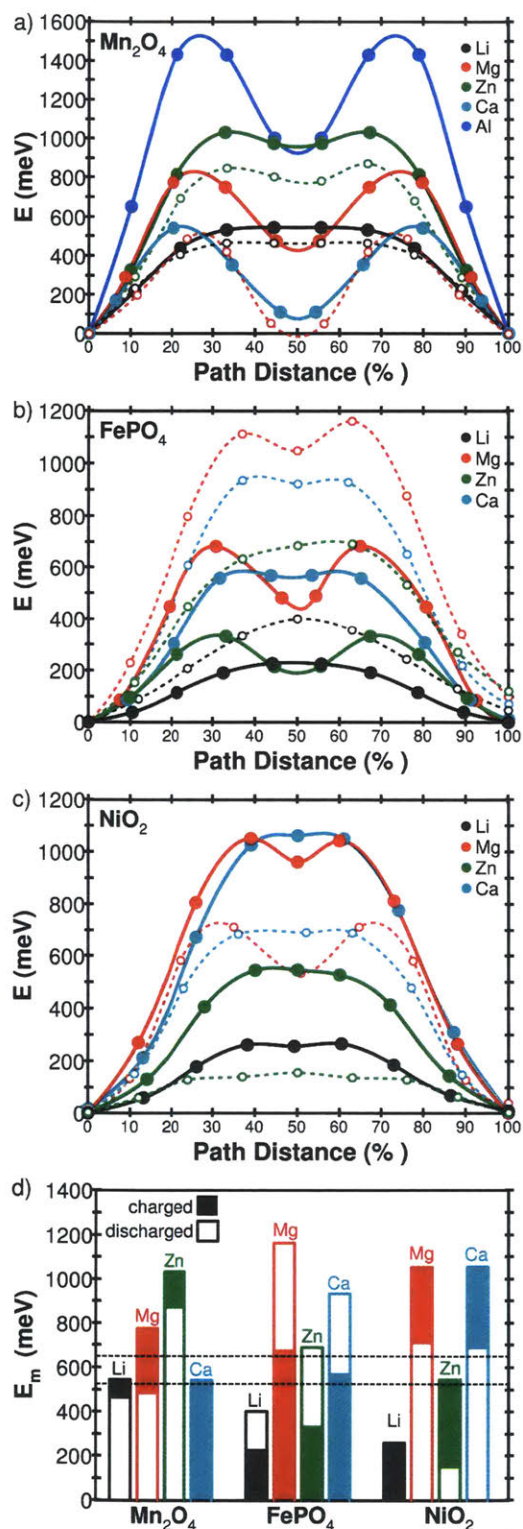


Fig 20. First-principles (NEB) results for Li^+ and MV (Mg^{2+} , Zn^{2+} , Ca^{2+} , and Al^{3+}) migration energies E_m in the (a) spinel Mn_2O_4 , (b) olivine $FePO_4$, and (c) NiO_2 structures, in the deintercalated/charged limit (solid lines), and the intercalated/discharged limit (dashed lines), with

(d) a summary of migration barriers E_m compared to the prescribed ~525–650 meV threshold (dashed).

As expected, the Li migration barriers are low, either well below or just above the ~525 meV threshold in good agreement with experimentally observed reversible Li intercalation and previous theoretical computations.^{69, 70, 170, 182} MV ion diffusion is categorically poorer than Li^+ diffusion in the same structure, and the Al^{3+} barriers are higher than all the +2 ions, which in turn exhibit higher barriers than Li^+ . In fact, the Al^{3+} barriers are so high that it is reasonable to conclude that bulk Al^{3+} intercalation into a close-packed oxygen lattice may not be possible at room temperature. The divalent ions (Mg^{2+} , Zn^{2+} , and Ca^{2+}), although noticeably more difficult to intercalate than Li^+ , can be below or near the ~525–650 meV threshold: Zn^{2+} in FePO_4 and NiO_2 , Mg^{2+} in FePO_4 , or similarly Ca^{2+} in Mn_2O_4 and FePO_4 .

As previously demonstrated in a variety of oxide spinels by Liu et al.,¹⁹⁰ the transition metal chemistry does not significantly affect the MV cation diffusion path and respective barriers. We will demonstrate that the general features of the migration energies shown in Figure 20, panels a–c can be rationalized by considering the changing anion coordination environment along the diffusion path. In the close-packed oxygen structures of our model compounds (face-centered cubic *fcc* for spinel and layered, and hexagonal close-packed *hcp* for olivine), the tetrahedral (*tet*) and octahedral (*oct*) interstitial sites share a face. Direct migration between equivalent sites (either *oct* to *oct* or *tet* to *tet*) is usually very high in energy as it requires the ion to pass through a narrow O–O bond⁶⁸ which is also reflected in our result for hop through the oxygen dumbbell in layered NiO_2 . Rather, the lower energy path typically crosses through a shared face between *tet* and *oct* sites leading to diffusion topologies that are either *tet* → *oct* → *tet* (shown in Figure 21a) or *oct* → *tet* → *oct* (shown in Figure 21b) depending on which insertion site is stable. As an example, the spinel diffusion topology is shown in detail in Figure 21, panel a: the

intercalating ion initially resides in the stable tetrahedral *tet* site (with energy E_s), then migrates through a three-coordinated oxygen face (with energy E_a) shared with the adjacent intermediate octahedral *oct* site (with energy E_i), and finally follows a symmetric path to the next equivalent stable site. In the olivine and layered structures, diffusion proceeds in a similar fashion but between stable octahedral sites through an intermediate tetrahedral site (shown in Figure 21b). Revisiting Figure 20, panels a–c, the local minima are seen to correspond either to the stable or intermediate sites, and maxima either to the three-coordinated or intermediate sites.

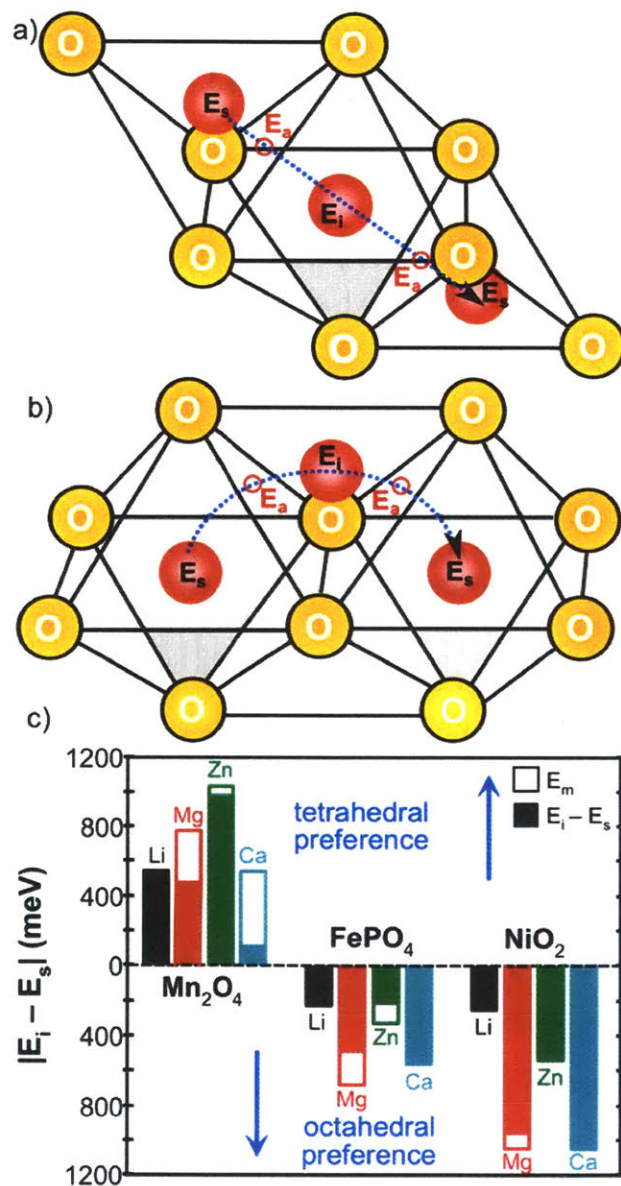


Fig 21. Low-energy ion migration paths in close-packed oxides adopt either (a) *tet* → *oct* → *tet* or (b) *oct* → *tet* → *oct* diffusion topologies: beginning in the stable insertion sites (E_s), crossing through a three-coordinated oxygen face (E_a) into the intermediate site (E_i), and finally migrating to the next stable site through a symmetric path. Comparing the (c) site energy difference $|E_i - E_s|$ between *tet* and *oct* sites (solid bars) to the migration barriers E_m (hollow bars) along the diffusion path for Li^+ , Mg^{2+} , Zn^{2+} , and Ca^{2+} in spinel Mn_2O_4 , olivine FePO_4 , and layered NiO_2 reveals the underlying influence of each intercalant's anion coordination preference on the migration barrier.

Since the *tet* and *oct* sites are always part of the ion migration path, the absolute value of their energy difference $|E_i - E_s|$ shown in Figure 21, panel c is then a lower bound on the migration barrier E_m . In these cases, the energy along the migration path assumes a single “plateau”-type shape, as can be seen in Figure 20.⁶⁸

Consequently, the site energy difference (solid bars) can be used as a criterion for mobility screening and in some cases is even identical (e.g., Li^+ in Mn_2O_4 and FePO_4 , Ca^{2+} in NiO_2) or nearly identical (e.g., Li^+ in NiO_2 , Zn^{2+} in Mn_2O_4 , and NiO_2 , and Ca^{2+} in FePO_4) to the migration barrier (hollow bars). The energy differences obtained from our DFT calculations (Figure 21c) correlate well with the known site preference of the intercalated species. In the crystallography and mineralogy literature, the anion coordination environments of several different cations have been exhaustively catalogued: Li^+ and Zn^{2+} are most often found in four-, Mg^{2+} in six-, and Ca^{2+} in eight-coordination.^{199, 220} Furthermore, in their systematic study of inverse and normal spinels, Burdett et al. observed the consistent trend that the tetrahedral site preference decreases in order of Li, Zn, Mg, and Ca.^{187, 221} Clearly, the combined knowledge of the diffusion topology and preferred coordination environment of the diffusing species now allows us to explain the variation of the barriers in Figure 20. For example, Zn^{2+} has a very high migration barrier in the spinel structure, as its stable insertion site is also its preferred coordination (tetrahedral). Similarly, Mg^{2+} has high

migration barriers in both the layered and olivine structures, where the stable insertion site is six-coordinated.

Ca^{2+} prefers to be eight-coordinated and is especially penalized when migrating through a site with significantly lower coordination, explaining the high migration barriers in both layered NiO_2 and olivine FePO_4 , which require migration through an intermediate tetrahedral site. On the other hand, when the intermediate site is the intercalant's preferred coordination, the site energy difference is smaller, for instance, Li^+ and Zn^{2+} in olivine and layered compared to spinel, and similarly Mg^{2+} in spinel compared to olivine and layered.

To study the effect of intercalant concentration, we also investigated vacancy diffusion barriers in the fully discharged limit in our test structures (dashed lines and hollow bars in Figure 20). For spinel, we used composition $(\text{M})\text{Mn}_2\text{O}_4$, $(\text{M})_{0.5}\text{FePO}_4$ for olivine, and $(\text{M})\text{NiO}_2$ for layered. Although the migration barriers in the discharged limit may either increase (as seen in olivine FePO_4) or decrease (as seen in both spinel Mn_2O_4 and layered NiO_2), our observations relating migration barrier to site preference continue to hold. In the spinel system, the increasing degree of intercalation further stabilizes the intermediate octahedral site due to the decreased electrostatic interaction with reduced nearby transition metal ions, an effect that has also been observed in the studies of Li diffusion in spinel Co_2O_4 , Ni_2O_4 , and Ti_2O_4 systems.^{170, 182, 190} When the calculations are able to converge, Ca^{2+} is shown to be even more stable in the intermediate octahedral site rather than the tetrahedral site,¹⁹⁰ which is a strong indicator of its instability in the normal (tetrahedral occupancy) spinel structure.

For olivine FePO_4 , we investigated migration in the half-intercalated structure to limit reduction to Fe^{2+} and place the divalent intercalants in a known low-energy ordering of $\text{Li}_{0.5}\text{FePO}_4$ where the intercalating species occupy alternating octahedral sites oriented along the 1D diffusion direction.²²² To arrive at an equivalent stable insertion site now requires migration

through two consecutive but symmetrically equivalent *oct-tet-oct* motions, which explains why the migration energies at the end points are larger than zero in Figure 20, panel b. Compared to migration in the empty host, occupation of the intermediate tetrahedral site is further penalized due to the proximity of a nearby intercalated (Li or MV) cation, which pushes the diffusion path away from the tetrahedral site and nearer toward the shared edge between octahedral sites, as seen in Figure 21, panel b. Consequently, the diffusion path begins to resemble direct *oct-oct* migration more so than *oct-tet-oct*, which is reflected in the shift to a “plateau”-type shape of the migration energy and also higher migration barriers, as observed in Figure 20, panel b. In layered NiO_2 , we calculated the migration energy for the low-energy divacancy migration as observed in the LiCoO_2 system⁶⁸ and found that the MV migration barriers are reduced in the discharged limit as the layer spacing increases, stretching the intermediate tetrahedral site and simultaneously lowering the energy penalty for occupation.^{68, 69}

From our quantitative study of cation diffusion, a clear picture emerges on the relation between structure, chemistry, and intercalation mobility. The observed dominance of site energies and coordination preferences would imply that cation mobility is the first order determined by the careful matching of an intercalant’s site preferences and the structure’s topology (for a given anion chemistry) and less so by other factors that have been empirically brought forward such as transition metal chemistry, “openness” of structure, or ionic size. In particular, the fact that we find very different barriers for Zn^{2+} and Mg^{2+} , which have similar ionic size (72–74 pm),²²³ seems to limit the usefulness of ionic size as factor in estimating mobility. In addition, a recent study on diffusion in spinels found only a small effect on cation mobility from varying the transition metal chemistry.¹⁹⁰ Although the particular transition metal chemistry in a structure is not a primary factor, it can influence migration energies through secondary factors such as lattice parameter, site disorder (e.g., Ni in layered compounds²²⁴), or subtle changes in electrostatic screening. An

example of the latter is the small difference between late and early transition metal layered compounds.⁶⁹ The diffusion path is to a large extent controlled by a structure's topology as ions hop from one site to another through the faces between anion polyhedra, and the energy along the path is controlled by the relative site energies and the preferred coordination of the intercalating ion.

These observations lead us to a two-fold strategy to identify host materials with high MV intercalant mobility: identify structures in which a specific intercalant inserts in a site that does not have its preferred coordination. This makes it more likely that the migration energy will be low as the insertion energy is already "high", although the lower free energy of insertion comes with a reduction in voltage.¹⁶¹ Our results show several examples of this strategy, Zn^{2+} in olivine FePO_4 and layered NiO_2 , Mg^{2+} in spinel, and Ca^{2+} in spinel all fit this description, and all have migration barriers E_m that are either below or very near to the ~525–650 meV limit. When the opposite occurs, as for Zn^{2+} intercalation in spinel, the migration energy is very high, as seen in Figure 20, panel c. The insertion of a MV ion into a "non-preferred" coordination environment almost certainly guarantees that the discharged structure is thermodynamically metastable rather than thermodynamically stable. We observe this behavior for Ca^{2+} in the discharged spinel structure,¹⁹⁰ as well as for Zn^{2+} in layered NiO_2 , in marked contrast to lithium cathodes, which are usually ground states in their discharged (lithiated) state but metastable in their charged state. Our strategy to displace the instability to the discharged state where the cathode is less oxidizing and does not store electrical energy contributes to battery safety. Indeed, in lithium-ion batteries, the maximum oxidation power, largest cathode structure instability, and maximal electrical energy stored in the cell all coincide in the charged state creating a serious thermal runaway and safety problem.¹⁶⁵ The desire to have the intercalant not in its preferred coordination also calls into question the approach of synthesizing candidate MV cathode materials with the MV ion already

present; in this case, it will likely form a structure where its coordination is favorable, making its migration barrier high. Hence, favorable cathodes for MV intercalation should be sought from oxidized host materials that do not contain the intercalant. The materials for which Mg insertion has been established, orthorhombic V_2O_5 , layered MoO_3 , and Chevrel Mo_6S_8 , all display this characteristic identity prototype structures that have low coordination change along the diffusion path, either intrinsic to the structure or by flexibility in the structure. We believe that nanoparticle V_2O_5 in which slow Mg insertion has been established^{58, 217, 218} is an example of such a structure.

The migration energies of Li^+ , Mg^{2+} , Zn^{2+} , Ca^{2+} , and Al^{3+} in the δ - V_2O_5 structure are shown in Figure 22, panel a along with the diffusion path illustrated in Figure 22, panels b–d. The δ -phase of V_2O_5 has a pseudolayered structure composed of sheets of edge- and corner-sharing VO_5 square pyramids with the intercalating species sitting in corner-sharing tetrahedral sites, as shown in Figure 22, panel b. Although the intercalating species is situated in what appears to be a tetrahedral environment, there are two additional oxygen atoms nearby. Hence, Mg can be thought of as nominally “4 + 2” coordinated. The diffusion topology is now “4 + 2” – “square pyramid” – “4 + 2” through the three-coordinated shared face (as seen in Figure 22c). More detailed information regarding the V_2O_5 structure can be found in the literature²²⁵. Since the coordination change between the stable and intermediate site is smaller than in structures with close-packed anion sublattices (“4 + 2” – 5 – “4 + 2” compared to 4 – 6 – 4), the site energy difference is expected to be smaller, as is indeed observed in Figure 22, panel a, where $E_i - E_s$ is ~200 meV or less for all diffusing species considered. Not only are the site energy differences well within the prescribed ~525 meV E_m threshold, but also are the barriers for Ca^{2+} and Zn^{2+} in V_2O_5 (also Mg^{2+} is not very high either at ~600 meV in the charged state). Indeed, Ca and Mg intercalation has been established in V_2O_5 .^{(24)²¹⁷} Careful observation of the V_2O_5 host structure at various stages of MV cation migration shows that the layers ripple (denoted by the angle θ

in Figure 22d) according to the structure's low-energy phonon bending modes,²²⁶ which facilitate a pseudo four-coordination as the diffusing species migrates through the three-coordinated shared face. Therefore, since there is minimal coordination change along the diffusion path in V_2O_5 , both between the stable ("4 + 2") site, the intermediate site (square pyramid), and the shared face (pseudo-tetrahedral), the migration barriers are accordingly low as confirmed by the first-principles calculations in this work.

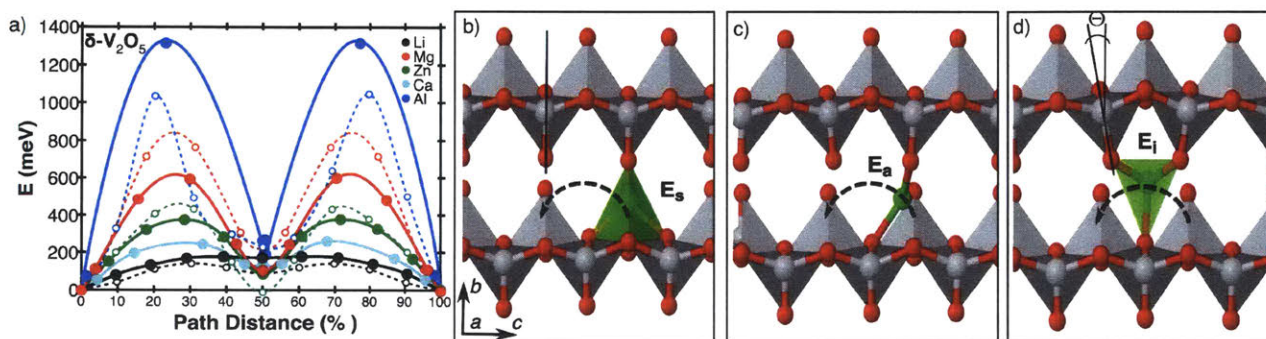


Fig 22. (a) Li and MV migration energies plotted along the diffusion path in $\delta-V_2O_5$ in the empty lattice (solid) and dilute vacancy (dashed) concentration limits as seen for Mg in the (b) stable, (c) activated, (d) and intermediate site.

In this paper, we focused on the effect that structural topology has on cation diffusion and did not investigate the effect of anion chemistry though it can substantially influence the migration barrier of intercalants by changing the site preference through size effects and ligand interactions. In addition, the generally better ionic conductivity of sulfides as compared to oxides has been attributed to better screening of the electrostatics by S^{2-} compared to O^{2-} .⁶⁹ Hence, sulfides may be expected to have better MV-ion mobility than oxides. However, heavier anions will lead to a reduction in specific energy both through their higher weight and through a limit on the voltage they can achieve as the p -states of anions such as S are above the d -states of the oxidized level of the S^{2-} states.

In summary, we have charted the migration energy of multiple high-valent intercalation ions in common oxide host materials combining the predicting capabilities of DFT and the NEB approximations. While our results give little hope to use Al^{3+} intercalation in an oxide host for energy storage, the divalent intercalants have close to reasonable migration barriers to enable room temperature intercalation. More importantly, our ability to identify clearly the factors through which structure governs their migration energy has enabled design guidelines for finding high mobility host materials for divalent cations. We believe that this is an important step forward to realize the full promise of high-energy density storage systems based on MV ions.

Chapter 6. High-throughput NEB

NEB calculation is 3-step calculation:

Step 1. Execute DFT calculation of the starting point and ending point of the diffusion path. After choosing the host structure and the diffusing cation, a super cell structure is constructed for DFT calculations, with the moving cation in the starting and ending position.

Step 2. Extract the structure information from previous starting and ending point DFT calculations, a diffusing path of the cation is interpolated between two end point structures. Because I'm using a guessing algorithm³³ for the diffusion path, by the requirement of the algorithm, an extra DFT calculation is necessary for finding an optimal path to start the NEB DFT calculation.

Step 3. Starting from the interpolated guessing path, execute NEB relaxation DFT calculations.

Thus, the first system I tried is to put this normal manual calculation into high-throughput automatic system.

6.1 Framework

The automatic job tree structure is shown in Fig. 23. It's roughly the same structure of the 3 steps plus database extraction and insertion, except from the detour job structures that I added into the DFT calculations of Step 1 and Step 3.

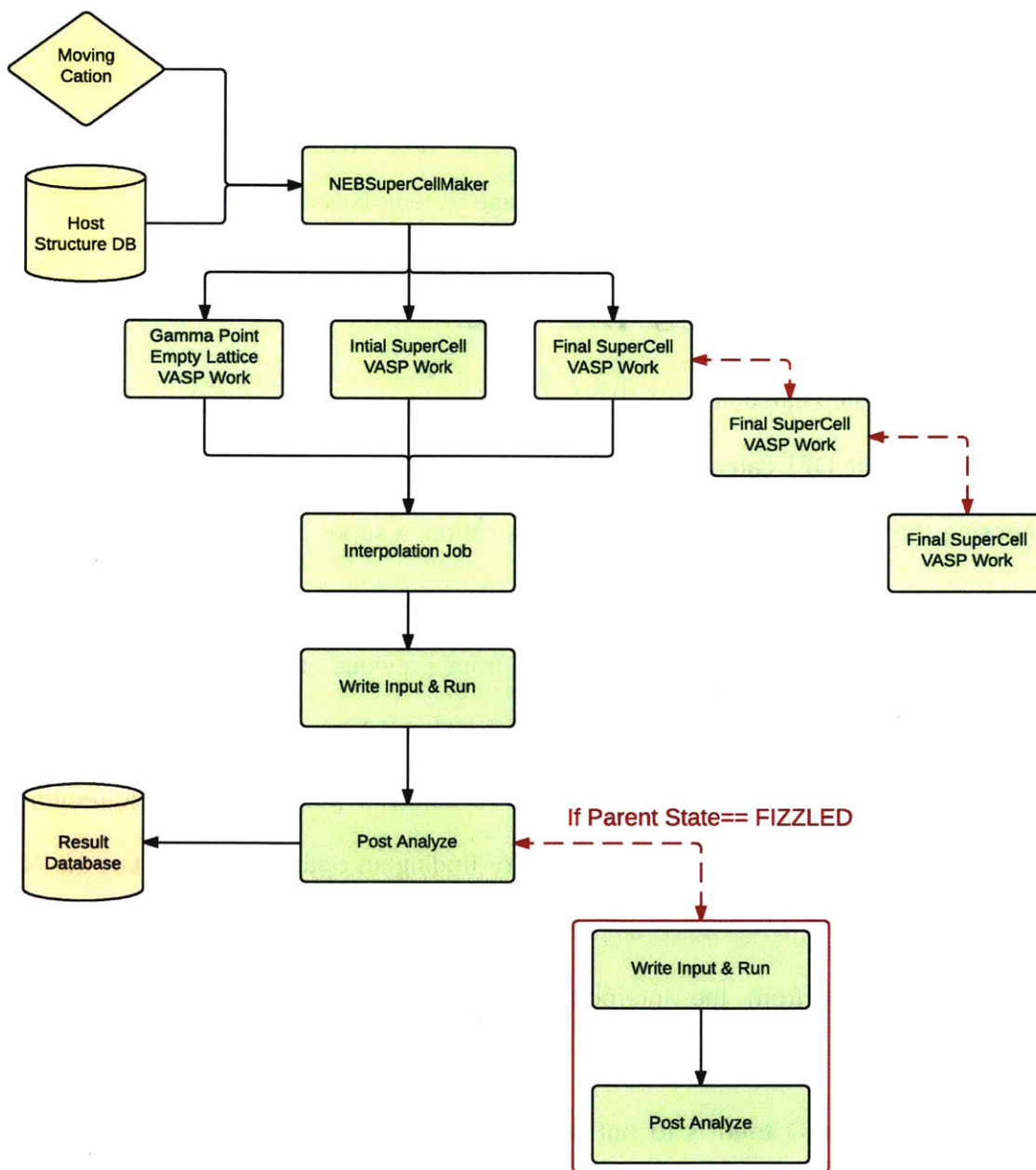


Fig. 23. Job structure tree for NEB calculations

The detours are designed as an error handler system. The design is to stop the calculations at certain frequency (e.g. every 10 hours), and have a script job to check the status of the previous DFT job. There are three possible different results for the check:

- There is an error found from the output of the previous job. Then corresponding corrections are made and a new job with such corrections is restarted from the initial state of previous job.
- There is no error found, but the previous job is not completed. Then a new job is created from the ending status of previous job.
- There is no error found and the previous job is completed. Then the detour structures are finished and the system returns back to the main tree for executing the next step.

To automate the dependencies of each job inside the job tree, I'm using a set codes called Fireworks, designed and implemented by my collaborator Anubhav Jain. It utilizes a workflow model:

- A FireTask is an atomic computing job. It can call a single shell script or execute a single Python function (either within FireWorks, or in an external package, like VASP for the DFT calculations).
- A FireWork contains the JSON spec that includes all the information needed to bootstrap the job. For example, the spec contains an array of FireTasks to execute in sequence. The spec also includes any input parameters to pass to the FireTasks.
- A Workflow is a set of FireWorks with dependencies between them.

Between FireWorks, a FWAction can be returned to store data or modify the Workflow depending on the output

In summary:

Workflow = A set of FireWorks + dependencies between FireWorks

FireWork = A set of FireTasks + linear sequence of FireWorks + spec

FireTask = A script or a call for external program

Each of the green blocks in Fig. 4 is a FireWork. And the tree depicts the dependencies among them. Detours and data passing between FireWorks are created or done by returning FWAction.

5.2 Obstacles

After implementing this high-throughput machine with some effort, the system is capable of reproducing the manual results (Fig. 24).

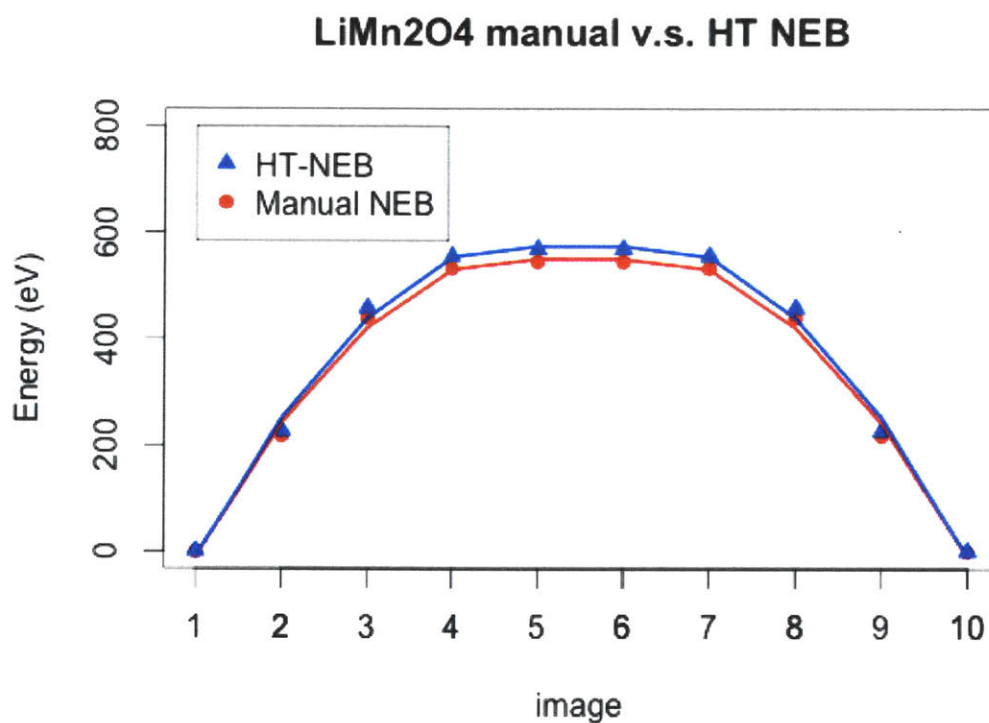


Fig. 24 High-throughput NEB results comparing with manual NEBs, Li migration in Mn₂O₄ spinel structure

However, when I put more structures into the system, the job failure rates turn out to be really high (>60%) and most of the job errors can't be easily dealt with. The other problem I am facing is high-throughput NEB consumes a great amount of computation resources (CPU hours), which limit the method to be applied to a wider range of structures database.

Chapter 7. PathFinder and ApproxNEB Algorithms

In this chapter, we intend to develop new algorithms to solve the problems presented in Chapter 6. The standard workflow for the NEB calculation consists of 3 main steps:

- Step 1. Relax the initial and final state structures.
- Step 2. Linearly interpolate a number of images between initial and final states.
- Step 3. Apply the NEB algorithm to compute the MEP.

We find that the linear interpolation in Step 2 is the primary source of inefficiency and instability in the calculation procedure. This is especially true if the final MEP displays substantial curvature from the initial linear interpolation. Furthermore, during the preparation of the NEB calculation in some systems, the linear interpolation can place atoms (of one image) at unreasonably close distances to one another, causing instability during the NEB relaxation (see for example, the CaMoO₃ structure in the section 7.4). Here we present a new method to initialize the NEB interpolation close to the final relaxed band that we call *PathFinder Algorithm*. In the following sections, we discuss the idea behind the *PathFinder algorithm* and give details about its implementation. We also test the *PathFinder algorithm* on a set of six materials, demonstrating its predictive capabilities and the computational runtime reduction it brings.

7.1 Methods

In the NEB algorithm, each image along the band is relaxed by two forces – the true force from the potential and the spring force (from the virtual springs) connecting adjacent images. Note that both forces are decomposed into components perpendicular and parallel to the path, and only the perpendicular component of the true force and parallel component of spring force are relaxed in the NEB procedure. The force projection is referred to as ‘nudging’ and leads the chain of images to the MEP. To predict the MEP with fewer computational resources, we would like to imitate this relaxation process starting from a static potential. As the spring forces are very easy to simulate, the difficulty lies in finding a potential field that is able to reproduce the true force from first-principle calculations.

The key idea behind *PathFinder* is that when an atom migrates inside a host structure, it moves to avoid atoms or bonds, as atomic charge density overlap with other species would correspond to reactions, or at least large changes in energy. Consequently, non-reactive migration paths should avoid concentrations of electronic charge density. Thus, we propose using the electronic charge density obtained from DFT as the potential landscape within which to estimate the migration MEP. In general, this potential will push migrating atoms to regions of diminishing charge density, corresponding to areas void of atoms or bonds, matching the intuition regarding the migration path geometry.

Based on this construction, the migrating images relax according to the sum of two forces:

$$\vec{F} = \vec{F}_1 + \vec{F}_2 = \nabla(\text{charge density}) + k_{PF} \cdot (\vec{r}_{n+1} - \vec{r}_n) \quad (1)$$

where \vec{F}_1 is the force coming from the charge density ‘potential’, \vec{F}_2 is the spring force, \vec{r}_n is the position of image n in real space and k_{PF} is the spring force constant for the pathfinder, where all quantities are given in non-dimensional form. The non-dimensional spring constant $k_{PF} = 0.17$ is a constant fit to best reproduce the paths from a full VASP NEB calculation with a default NEB spring constant of $5.0 \text{ eV}/\text{\AA}^2$. The relaxation algorithm we use for the migration path is the zero-

temperature string method (ZTS) described by *Vanden-Eijnden et al.*^{227, 228} We choose the string method specifically because it demonstrates superior performance to NEB when a large number of images can be used.⁷⁴ Finally, the positions of all non-migrating atoms can be interpolated linearly for the intermediate images, as their positions are nearly static and thus reasonably represented by the linear path.

The PathFinder requires three inputs (see Fig. 25):

1. The initial state structure (structure of the atom-vacancy pair pre-migration jump)
2. The final state structure (structure of the atom-vacancy pair post migration jump)
3. The charge density of the host structure

For illustration, Fig. 25 depicts the three inputs to compute Li diffusion paths in LiFePO_4 along the b axis,⁷¹ where in the initial and final states Li-ions sit in the stable sites. The PathFinder algorithm relaxes intermediate Li images along the migration path to positions on the MEP. To initialize the PathFinder algorithm, we compute the charge density of the host structure using a static calculation with Gamma point sampling of reciprocal space, as we have found that the paths thus obtained are sufficiently converged for all test cases. The output of the PathFinder algorithm are the positions of the intermediate images which can then be used to initialize a NEB calculation. As the computational cost of the PathFinder itself is negligible compared to the full NEB calculation, we find that it is effective to use a large number of interpolated images in the PathFinder to ensure optimal convergence of the string method, and then pick a small set of evenly spaced images from the estimated MEP to initiate the full NEB calculation.

The complete code set an example for using the algorithm can be found at the referenced github code repo. The code implementation depends on the *Python Materials Genomics* (*pymatgen*) Library.¹⁵⁸

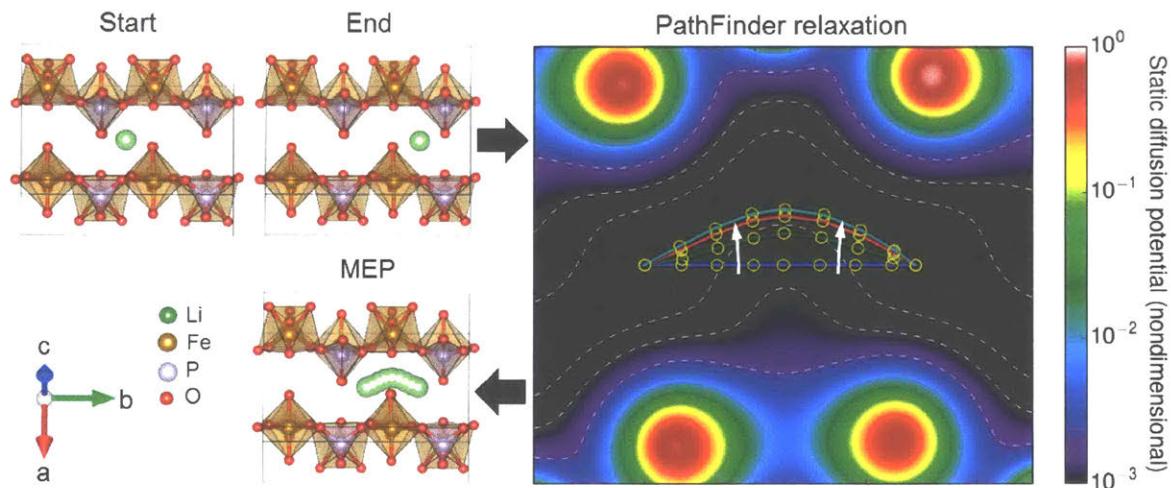


Fig 25. Illustration of the PathFinder Algorithm for an example of Li migration in LiFePO_4 (Li in green, O in red, Fe in brown, and P in purple) projected onto the plane-of-best-fit for the MEP. The upper left panel shows the initial and final states of the Li migration jump, which serve as the inputs to the PathFinder algorithm. The right panel depicts the path relaxation in the PathFinder algorithm, where the path is relaxed through the virtual potential derived from the DFT electronic charge density and the spring force, where the potential is shown color-coded by magnitude with equipotential contours depicted by dashed lines, and with white arrows indicating the direction of relaxation. Finally, the lower left panel depicts the final relaxed Li MEP path produced by the PathFinder algorithm, which is in close agreement to the MEP obtained from a full NEB calculation

7.2 Error Metric Definition

To assess the capabilities of PathFinder and ApproxNEB we study cation migration in a set of materials that are of practical interest in the field of batteries. As we expect the PathFinder and ApproxNEB methods to yield improved performance relative to standard NEB in cases where the migration paths deviate from straight-line paths, we report the curvature of the MEP as obtained by NEB calculations.

- Li in spinel LiTiS_2 (linear MEP);^{229, 230}

- Zn in spinel ZnMn_2O_4 (linear MEP);^{190, 231}
- Zn in post-spinel ZnMn_2O_4 (linear MEP);²³²
- Li in olivine LiFePO_4 (curved MEP);^{70, 222, 233-235}
- Mg in $\delta\text{-MgV}_2\text{O}_5$ (curved MEP);²³⁶⁻²³⁸
- Ca in layered CaMoO_3 (curved MEP).⁵⁸

To quantify the accuracy of the PathFinder algorithm in reproducing the geometry of the fully converged MEP, we define an error metric, shown schematically in Fig. 26. We first interpolate the full migration path obtained from an NEB calculation by connecting adjacent optimized images, i.e., the orange dots of Fig. 26. We then compute the distance $l(x)$ from this MEP for every image obtained from the PathFinder-relaxed path and report the maximum $l(x)$ as the error of the PathFinder-derived approximate MEP.

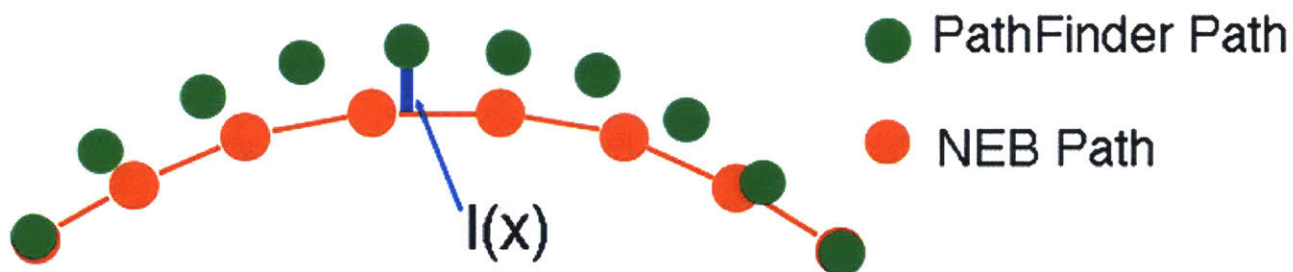


Fig 26. Illustration of the path prediction error metric.

7.3 PathFinder v.s. Linear Interpolation on Error Metric

The geometry error for the cation migration path for each benchmark material is given in Fig. 27. Specifically, for each material, we compare the error of the PathFinder path and the standard linear interpolation, with respect to the NEB-converged MEP, in order to understand which interpolation scheme can serve as a superior initialization. Note that while in the NEB calculations of the benchmark materials, seven images are used to interpolate the migration path, in the

PathFinder Algorithm, we use 21 images to ensure good performance of the string method. Nonetheless, for consistency, in Fig. 27b, we use seven equally spaced images for visualization.

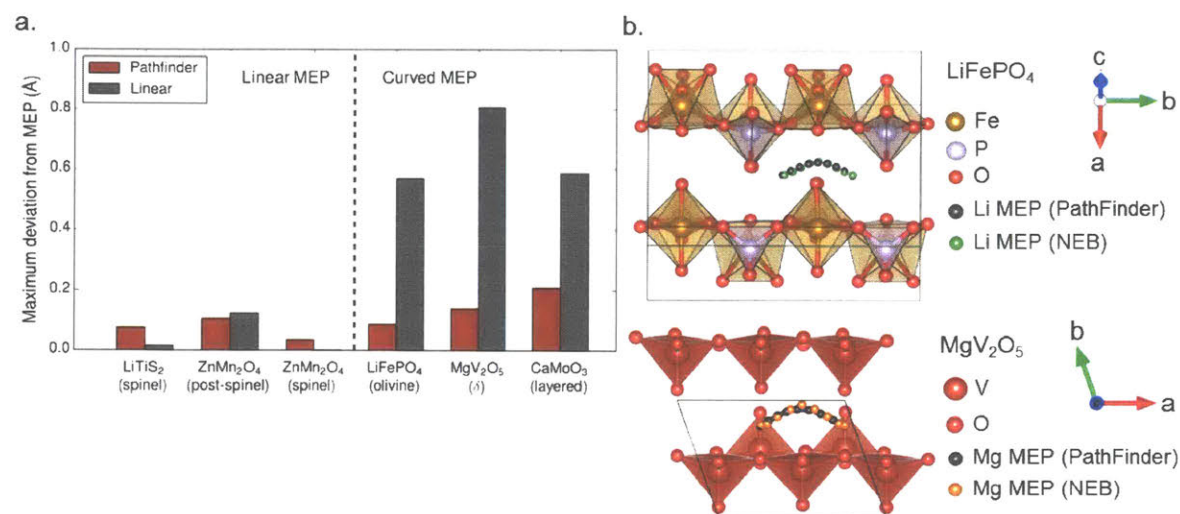


Fig 27. (a) Geometric error in the MEP initialization based on the PathFinder algorithm and linear interpolation across benchmark materials, illustrating the consistent performance of the PathFinder algorithm across both linear and curved MEP geometries. (b) A comparison of the migration path of Li in LiFePO₄ and Mg in MgV₂O₅ obtained the PathFinder algorithm (black) and the converged true MEP (green).

As is clear from Fig. 27a, if the fully relaxed NEB path possesses a large degree of curvature, the PathFinder algorithm systematically provides a better initialization than traditional linear interpolation. The migration path derived from the PathFinder algorithm falls within 0.2 Å of the NEB-derived MEP in all test structures, which is both a very small error in absolute terms, and is 5 to 10 times smaller than the error obtained from linear interpolation. Fig. 27b shows this agreement visually for the LiFePO₄ and MgV₂O₅ test cases. In both structures, the PathFinder algorithm reliably yields a migration path geometry very close to the true MEP structure, capturing the effect of nearby oxygens on the cation migration trajectory. In the cases where the MEP is

linear, the linearly interpolated initial band usually has a slightly smaller error than the PathFinder-derived path, as a linear interpolation is by circumstance already the optimal configuration. Nonetheless, the error of the PathFinder-derived path remains within the 0.2 Å bound observed earlier, which is a sufficiently small absolute error that we can expect its effect on the NEB calculation speed, accuracy, and stability to be negligible, as compared to the traditional linear interpolation scheme. Thus, we conclude that the PathFinder algorithm offers a robust estimate of cation migration MEPs, yielding a migration path within a small error of true MEP for both linear and curved geometries, offering both an efficient estimate of MEP geometry and a reliable initialization for subsequent NEB calculations.

7.4 PathFinder v.s. Linear Interpolation on Computational Resource Cost

To characterize the computational efficiency gains through the PathFinder initialization, we compare the runtime of NEB calculations initialized using the PathFinder scheme versus the traditional linear interpolation. The computational resources are measured by total CPU hours used on a Cray XC30 machine with a parallelization of 24 cores per image. To ensure a fair comparison, all computational parameters are kept the same for the two initialization schemes. The results of our test are given in Fig. 28. As could be expected from our analysis of MEP geometry, initialization using the PathFinder algorithm does not significantly affect performance for structures with a linear MEP for migration, but does lead to consistent performance gains in cases where the MEP deviates from a linear path.

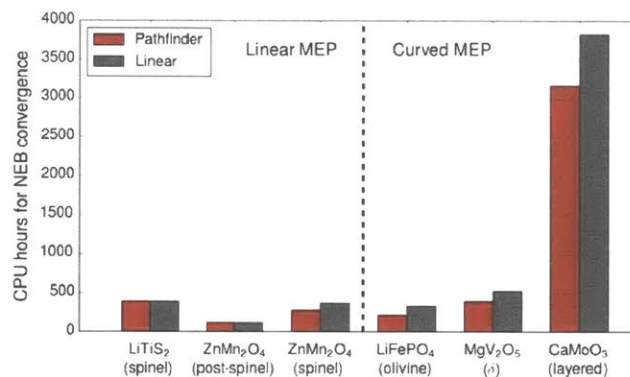


Fig 28. CPU hours used by the NEB calculations initiated from linear interpolation and PathFinder interpolation, respectively.

7.5 PathFinder v.s. Linear Interpolation on CaMoO₃ example

As we mentioned earlier, one of the common issues arising in NEB calculations is that linear interpolation can yield highly unphysical image structures that are difficult to relax due to exceptionally high forces and instabilities in the electronic minimization. PathFinder avoids this problem by biasing the migrating ion away from concentrations of electronic charge density, avoiding unintended reactions in the structure within intermediate images. For example, when calculating the MEP of Ca inner-layer diffusion along the *a* axis in CaMoO₃, we find that typical NEB with linear interpolation is unstable due to excessive forces in some images. The reason for this instability is clear from Fig. 29. Initialization of the NEB calculation from linear interpolation puts one oxygen atom (colored in yellow) too close to some of the Ca images, an issue which is avoided by the PathFinder. This unphysically small Ca-O distance results in large inter-atomic forces, destabilizing the calculation. Conventionally, such instabilities can be mitigated by careful tuning of convergence and relaxation parameters needed, resulting in a significant increase in runtime and decrease in throughput. Furthermore, such instabilities are the primary reason why

the NEB method has been difficult to automate and scale to thousands of compounds as is required for the newly emerging Materials Genome Database.¹⁵⁷

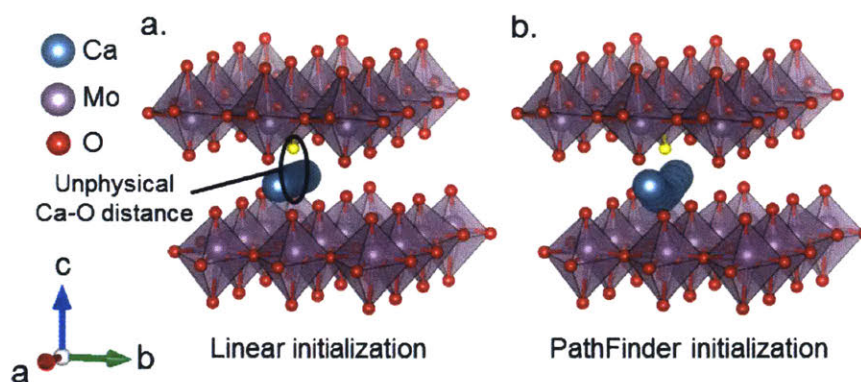


Fig 29. CaMoO₃ NEB calculations for Ca inner-layer diffusion. (a) Visualization of a standard linearly-interpolated path, illustrating the unphysical Ca-O distance that arises in the middle image. Note that the problematic interacting oxygen is marked in yellow. (b) Visualization of the PathFinder-approximated MEP, demonstrating a more physical migration path geometry that avoids the oxygen that lies near the migration path.

7.6 ApproxNEB Method

While the PathFinder algorithm can provide a good approximation of the geometry of the MEP, we will demonstrate in a later section that it does not yield accurate energetics along the path. For this reason, we propose to investigate the energetics of each image using the ApproxNEB method, in which the band is decoupled into individual image calculations.

The key idea of ApproxNEB is that, if we fix the moving cation along the approximate MEP obtained from the PathFinder algorithm, and perform a single point relaxation image by image, we can acquire the missing energetics, thereby fully characterizing the MEP. The difference between ApproxNEB and NEB algorithms are depicted in Fig. 30. In general, the execution of the NEB algorithm, in first-principles or classical potential codes, requires communication between images, as they are connected by virtual springs. At the end of each ionic relaxation step, images

communicate with each other to update spring forces and a new step in the constrained potential energy is taken – this procedure is repeated until the NEB force and energy criteria are satisfied. The ApproxNEB method removes the spring force and estimates the diffusion barrier by fixing the moving cation and relaxing other atoms in each image. In order to constrain translational degrees of freedom of the system, this procedure requires that the position of a reference atom that is farthest away from the moving ion in the unit cell to be fixed. This constraint prevents the whole cell from shifting uniformly to translate into the initial or final state. Under these constraints, the energy of the independently relaxed images provides an approximate MEP trajectory.

As discussed earlier, in NEB calculations, the migrating ions are relaxed by a combination of virtual spring forces and true forces, while non-migrating atoms are relaxed only by the true forces. The spring forces serve to push the migrating ions to higher energy positions on the MEP. However, if we already know the geometry of the MEP from the PathFinder method, the spring forces can be removed by fixing the moving cation on the MEP. From this perspective, ApproxNEB and NEB provide equivalent constraints on the system during relaxation.

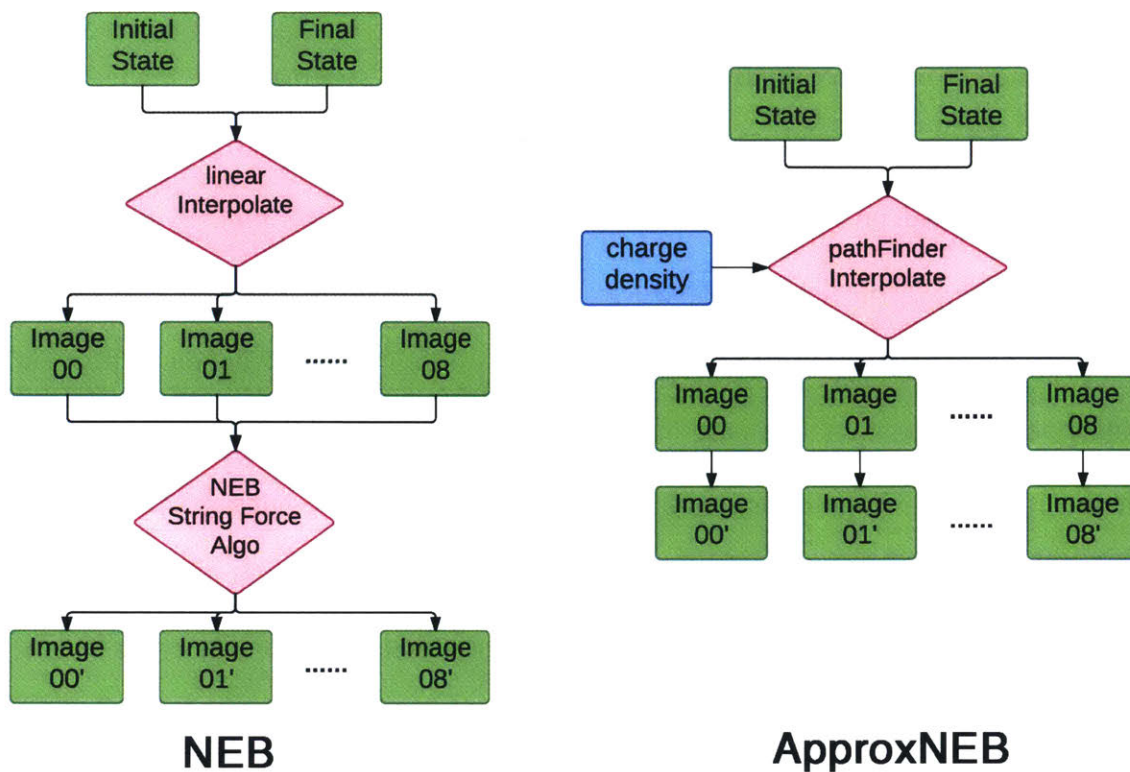


Fig 30. A comparison between traditional NEB and ApproxNEB calculation schemes. Here we assume that 7 images are interpolated between initial and final state (image 00 and image 08 are the initial and final states) and demonstrate that under the ApproxNEB scheme, image calculations are decoupled, decreasing the computational cost of the MEP characterization.

7.7 ApproxNEB v.s. NEB on Barrier Estimation

Having established the PathFinder approach as a reliable method to efficiently estimate migration geometry, we turn to the ApproxNEB approach of characterizing the energetics of the MEP. To assess the validity of this approach, we compare the overall energy profile of the MEP and the migration barrier obtained from the ApproxNEB algorithm to those obtained from a traditional NEB scheme. As can be seen in Fig. 31, the two methods yield energy profiles and migration barriers within 20 meV of each other, suggesting that ApproxNEB is able to reproduce the results of NEB to

good agreement across a variety of systems and migration geometries. As shown in Fig. 31b, the barriers obtained from ApproxNEB method are close to but systematically higher than those obtained from NEB. This trend is to be expected as in the ApproxNEB scheme, because the moving cation is fixed on the path provided by the PathFinder algorithm. By constraining the position of the diffusing species in each image, we reduce the degrees of freedoms available for relaxation as compared to traditional NEB, such that any error in the MEP geometry obtained from the PathFinder translates to an increase in the migration barrier. Nonetheless, just as the absolute error in the estimated MEP geometry remains within 0.2 \AA across all tested systems, the error in the migration barrier remains within 20 meV, which is a sufficiently small error margin for most high-throughput screening applications where we expect this method would be of greatest interest.

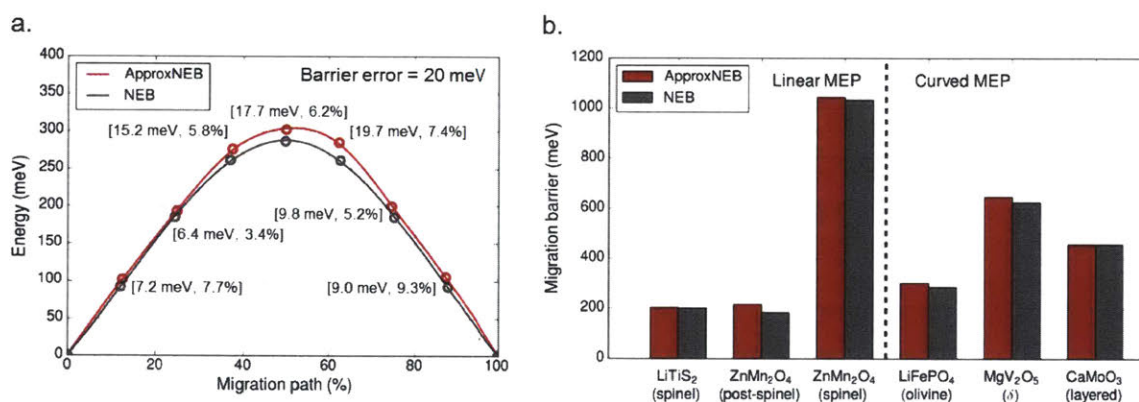


Fig 31. (a) Minimum energy path of LiFePO₄ obtained through NEB and ApproxNEB. The absolute and relative errors of each data point on the ApproxNEB path are labeled. (b) A comparison of migration barriers obtained through NEB and ApproxNEB demonstrating a consistent agreement between the two methods within a 20 meV error bound.

7.8 ApproxNEB v.s. NEB on Computational Resource Cost

It is important to note that the computational resources necessary for ApproxNEB are substantially lower than for traditional NEB, further justifying its use in high-throughput screening

applications. As can be seen in Fig. 32, for both linear and curved paths, ApproxNEB is systematically faster than the NEB method. Notably, we find that in the case of structures with curved MEP geometries, ApproxNEB yields a speedup by a factor of up to 5 with respect to linearly-initialized NEB, offering a significant improvement over even PathFinder-initialized NEB discussed earlier. The reason for this improvement lies in the decoupling of image calculations from one another. Decoupled images experience a much simpler potential field that remains quasi-static throughout the relaxation, enabling efficient minima-searching during ionic relaxation. Another issue is that of parallelization - in traditional NEB, because the position of the moving cation must be communicated among images to update spring forces, every image must be fixed to be at the same ionic relaxation step (see Fig. 30). This constraint hampers the progress of the calculation because when an image converges at a certain ionic step, it has to wait for all other images to converge before the next NEB step is taken, and some computational resources are wasted during this idle phase. Finally, error handling becomes much easier for ApproxNEB. For NEB, if a calculation fails due to a convergence problem with one specific image, the whole calculation has to be restarted. Given that in ApproxNEB each image is independent, only the failed image needs to be rerun. The improvements in both computation runtime and error handling make PathFinder and ApproxNEB suitable for scaling up to screen materials properties in a high-throughput fashion.

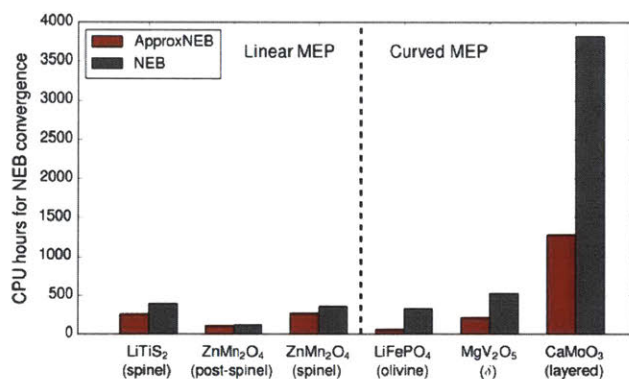


Figure 32. CPU hours consumed by ApproxNEB and NEB methods. For the NEB method, the band is initialized from linear interpolation. However, the performance gains of ApproxNEB are significantly higher than even PathFinder-initialized NEB shown in Fig. 28.

7.9 ApproxNEB Implementation

The key idea of ApproxNEB is to leverage the accurate paths predicted by PathFinder algorithm and decouple images into parallel calculations. The detailed implementation process, however, can be done in two different ways. As depicted in Fig. 33, one can either (a) start from applying PathFinder to un-relaxed start and final states and then include the calculation of two end point states in ApproxNEB, or (b) relax two end point states first, then apply the PathFinder and implement ApproxNEB at last.

Both workflows give the same reliable diffusion barrier and MEP. The CPU hours consumed by two workflows are however different. Applying two workflows to LiFePO₄ system, the CPU hours consumed by workflow (b) is substantially smaller than workflow (a) (~35%). This is understandable as in workflow (b), all intermediate images can take advantages of the well relaxed end point structures as they are interpolated from them. Note that all the data in Fig. 12 (in the manuscript) are thus obtained from workflow (b) implementation strategy.

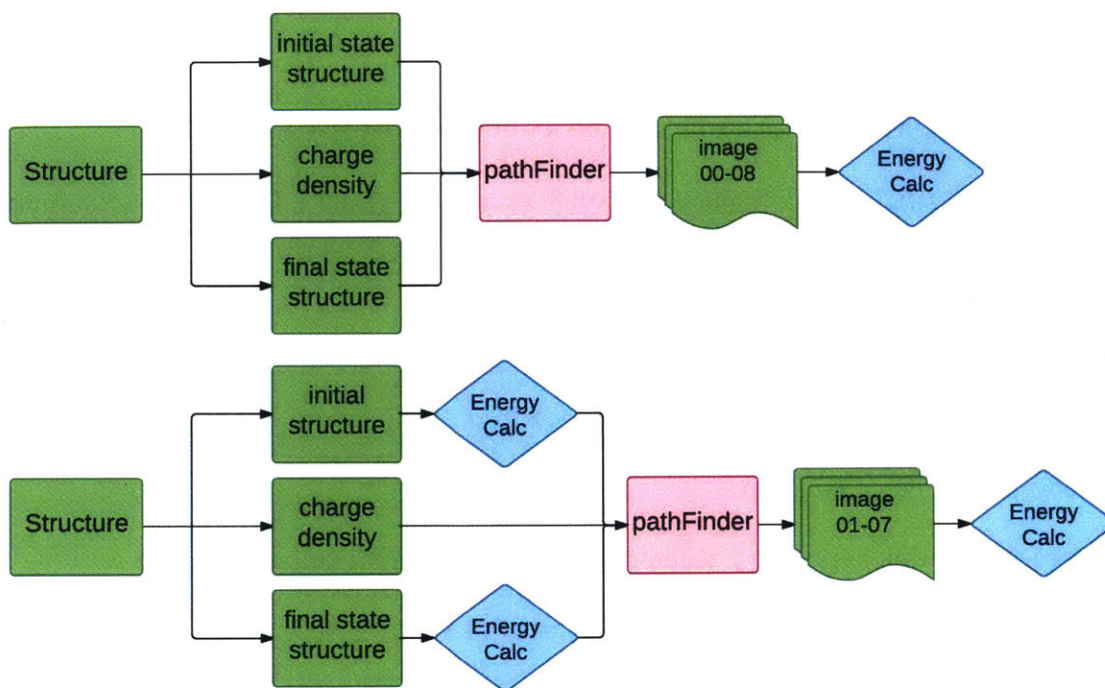


Fig 33. Different implementation strategy for ApproxNEB method. Note that as ApproxNEB method is indifferent to the specific first-principle software packages in use, we use “Energy Calc” in the graph to stand for the first-principle energy relaxation calculation carried out. (a) Apply PathFinder on un-relaxed structure, generate structure images including start and final states, and relax each image independently. (b) Firstly, relax start and final states, then apply PathFinder to the relaxed structures, and calculate the intermediate n images independently at last.

Chapter 8 High-throughput ApproxNEB and results

8.1 Error Handling

As we discussed, ApproxNEB has a huge edge over the traditional NEB method in high-throughput applications. Here we construct a simple estimate model to account for the mechanism. Assumptions below:

- For every material, ApproxNEB costs a of NEB time averagely ($a \sim 50\%$)

- Every calculation uses 7 images, every image costs the same computational power averagely.
- Every image, as itself, has a x failure rate for both ApproxNEB and NEB
- Apart from single image failure rate, NEB as a whole has a y failure rate (communication between images etc.)
- For every failure, assuming re-adjust parameters and redo can successfully converge the calculation. For ApproxNEB, we only need to redo the failure image, for NEB, we need to redo the whole calculation.

Then, for each material, assuming T is the computational time for doing NEB once.

$$T_{ApproxNEB} = aT(1 + x)$$

$$T_{NEB} = T[1 + 1 - (1 - x)^7 + y]$$

Depict these two functions in Fig. 34. From the graph, we can see that even though ApproxNEB only takes 1/2 of the time of NEB, but due to the fact that during error handling, ApproxNEB only needs to redo failure image while NEB needs to redo the whole calculations, ApproxNEB can save 2/3 of NEB time even at $x=10\%$

Computational Resources, ApproxNEB v.s. NEB

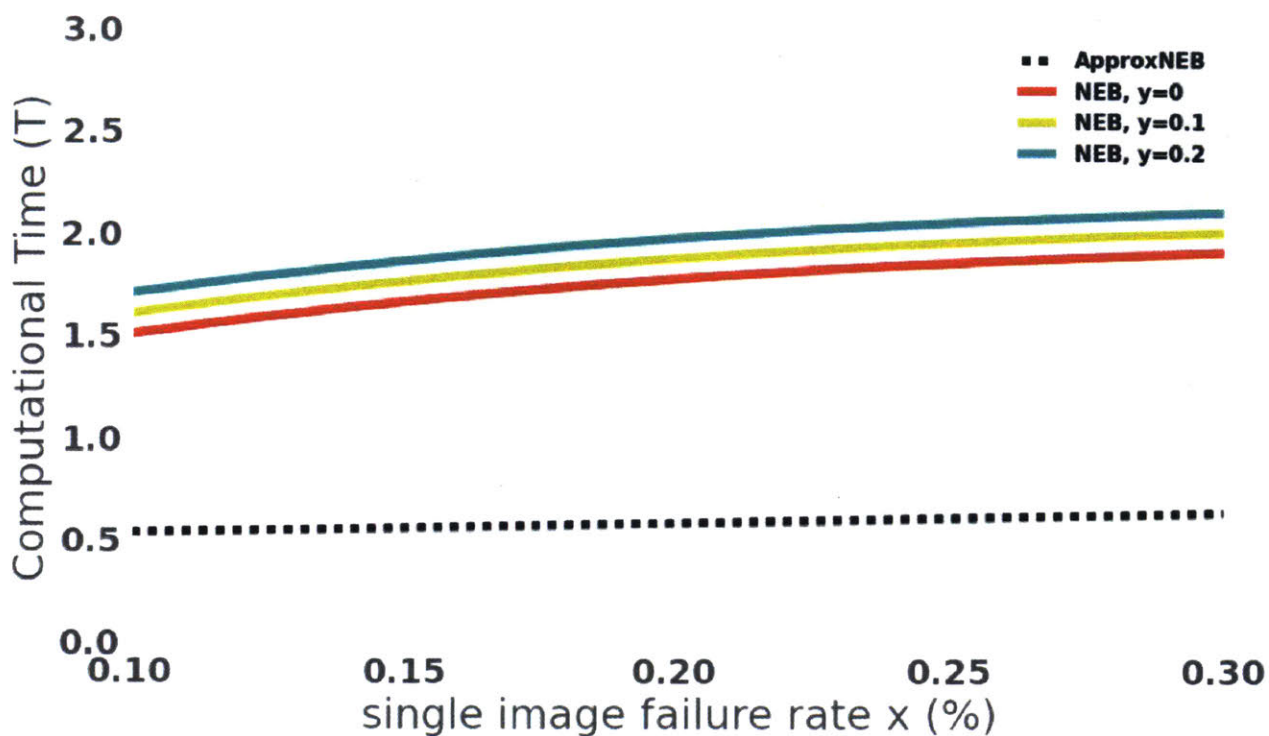


Fig. 34 Computational resources consumption, NEB v.s. ApproxNEB

8.2 EndPointFinder

A typical high-throughput application is a process shown in Fig. 35. The input database contains discharged structures, from which we know the site position of Mg in the host structures. Then we need a code module to identify the initial and final state (Fig. 33), i.e., we need a code module to automatically identify the migration starting point and ending point for a discharged Mg structure.

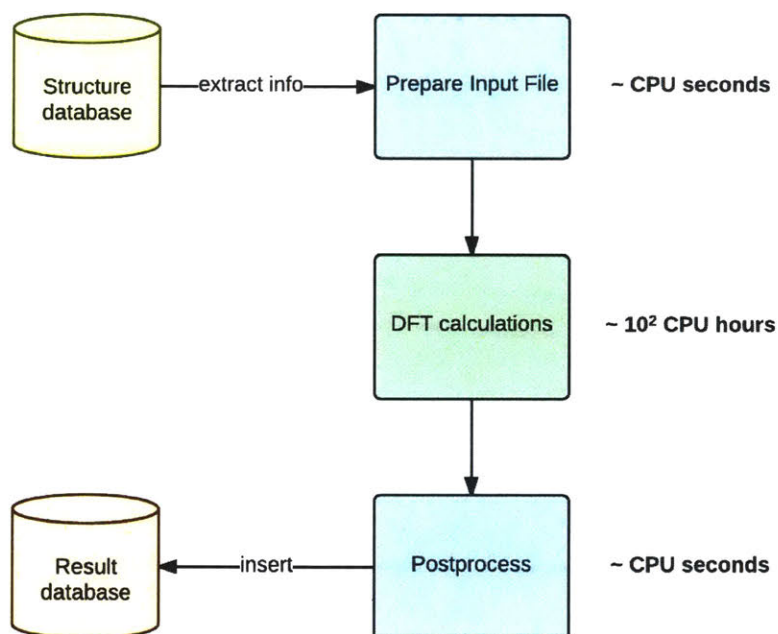


Fig.35, A typical Materials Science high-throughput job instance structure and associated computation time. The middle DFT calculation step usually contains one single DFT calculation.

We call this module *EndPointFinder*, it's an algorithm that takes a fully discharged Mg structure as input and output the migration initial structure, final structure and corresponding host structure for later *PathFinder* calculations. The algorithm workflow is shows as in Fig. 16. The basic idea is below:

- Step 1. Find all symmetrically identical Mg sties in the discharged structures
- Step 2. Calculate the pair-wise distance among all Mg atoms
- Step 3. Classify these distances based on the initial and final Mg site symmetry properties
- Step 4. Find the shortest distance in each class of Step 3.

- Step 5. If this distance is smaller than $1.25 \times \textit{shortest distance}$, then this is legal migration, and corresponding inputs for *PathFinder* algorithm will be generated for later calculations.

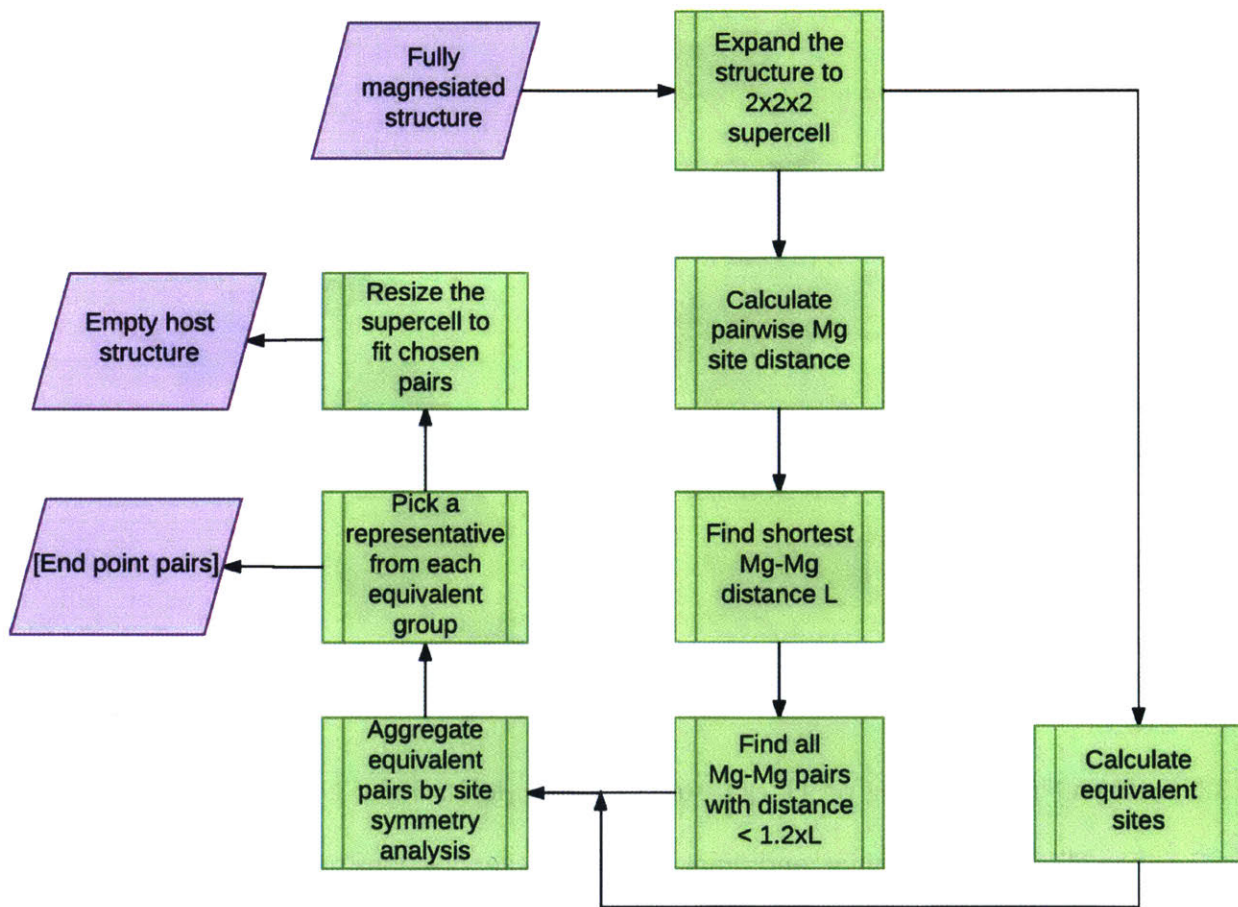


Fig 36. Algorithm workflow for EndPointFinder code module

Of course, to implement Step 1~5, we need to do some supercell scaling and shrinking, in case there is only Mg atom in a whole unit cell.

EndPointFinder turns out to be working really well, here we presented two testing examples.

Fig. 37 shows the example of LiCoO_2 , where *EndPointFinder* successfully identifies the inner layer migration pair. Fig. 38 demonstrates the example of LiFePO_4 , where *EndPointFinder* successfully identifies the Li migration path along b axis.

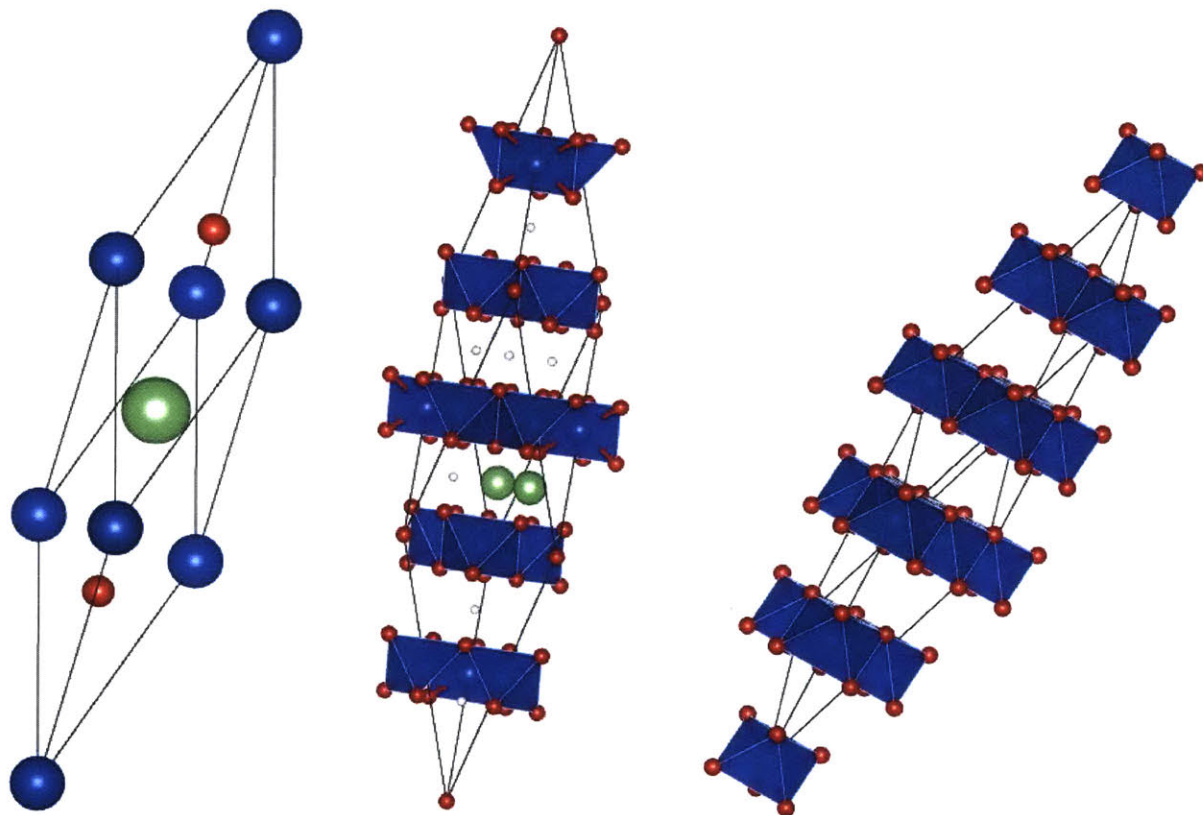


Fig 37. EndPointFinder working on LiCoO_2 structure, from left to right: LiCoO_2 unit cell; LiCoO_2 $2 \times 2 \times 2$ supercell, with the initial and final migration site positions identified; CoO_2 $2 \times 2 \times 1$ supercell, the corresponding smallest host structure for the migration.

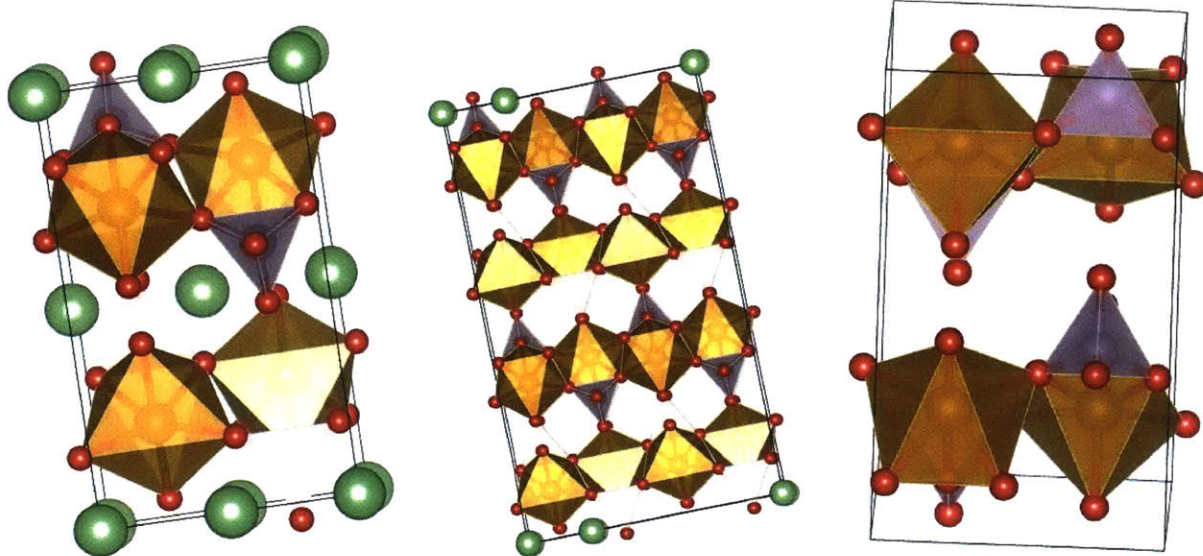


Fig 38. EndPointFinder working on LiFePO_4 structure, from left to right: LiFePO_4 unit cell, LiFePO_4 $2 \times 2 \times 2$ supercell, with the initial and final migration site positions identified; FePO_4 $1 \times 1 \times 1$ supercell, the corresponding smallest host structure for the migration.

8.3 Data Generation

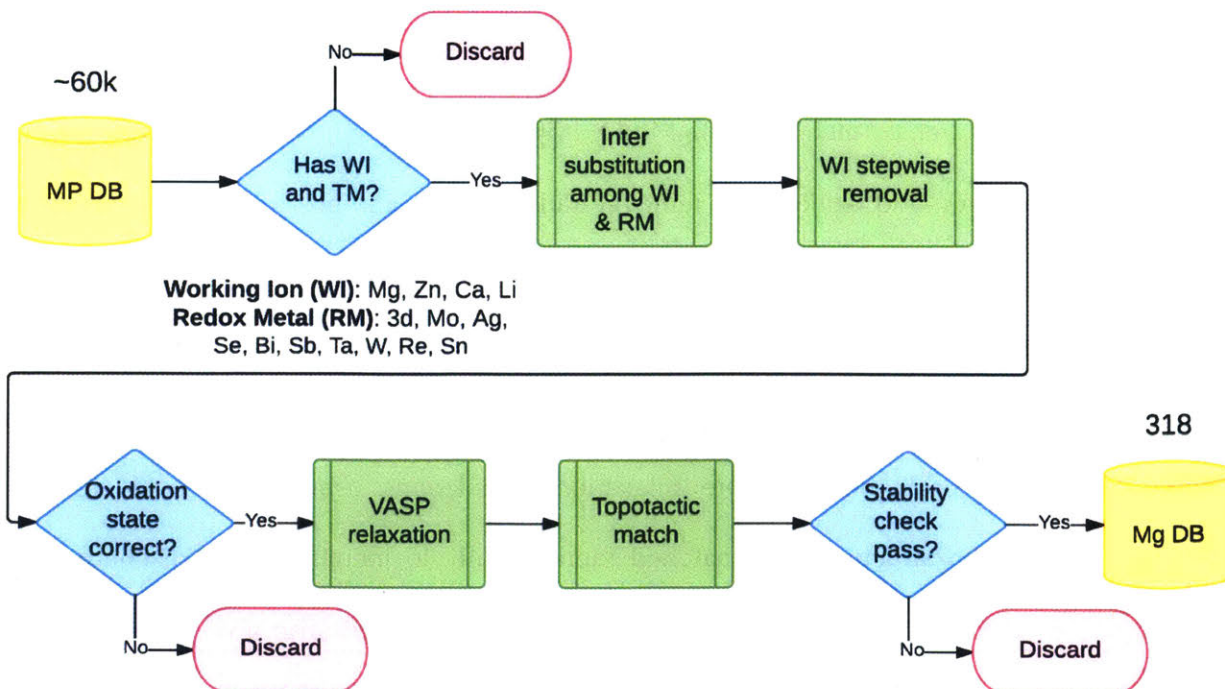


Fig 39. Generation process of the dataset for potential Mg cathode materials

To find a dataset where potential Mg-ion battery cathode materials may reside, we purposely screen and generate the Mg database starting from Materials Project (MP) Database²³⁹ with a workflow as described in Fig. 39. Started from around 60k materials entries in the MP database, we intend to find all possible discharged cathode structures and then derive new compounds and their charged duels through removing Mg. In order to extract/insert Mg from a material, an oxidizable metal has to be present in the compound to accommodate the redox reaction such as $\text{Mg}^{2+} + \text{TM}^{m+} \leftrightarrow \text{Mg} + \text{TM}^{(m+2)+}$. Hence, a cross-the board screening is performed over the MP database to obtain all structures that contain Mg and redox metal elements. The possible redox metal elements are all 3d transition metals plus Mo, Ag, Se, Bi, Sb, Ta, W, Re, Sn. In the spirit that a structure which is able to intercalate Li^+ , Na^+ , Ca^{2+} or Zn^{2+} is also potentially capable of intercalating Mg^{2+} and vice versa¹²⁴, we also collect the discharged cathode structures for other working ions using similar queries into the MP database. The next step is to inter substitute among redox metals and working ions in all the materials we obtained so far to expand the chemical space. Then to simulate Mg extraction process, every discharged structure we arrived at till now goes through a stepwise Mg removal transformation. For example, $\text{Mg}_2\text{Mo}_2\text{O}_5$ as the discharged structure is transformed into $[\text{Mg}_2\text{Mo}_2\text{O}_5, \text{MgMo}_2\text{O}_5, \text{Mo}_2\text{O}_5]$. Noticing not all materials derived from substitution and working ion removal transformation can possibly exist in nature, the sanity check is added to eliminate the compounds with unreasonable oxidation state of each element. For example, Ni^{5+} is not viable in nature, so compounds like Ni_2O_5 are removed at this step. We pass the newly created materials to Materials Project high-throughput computation machine to run first-principles structure relaxation calculations using VASP software^{114, 115}. Afterwards, the relaxed structures are matched topotactically to identify charge/discharge pairs using a structure matching algorithm²⁴⁰. The first-principles calculations also give us the energy of each relaxed structure, with which we are able to construct the phase diagrams using available

compounds in the Materials Project Database¹⁶² and evaluate their relative phase stabilities. In consideration for metastable materials that can be synthesizable in principle²⁴¹, we enforce a screening criteria that one of the charged and discharged structures must bear an energy above the energy hull below 100meV/atom and the other below 300meV/atom. The screened materials after the stability check construct the Mg database we seek, in which there are 318 charged/discharged pairs.

8.4 Workflow

In the HT machine we implemented, we used a set of new algorithms based upon NEB method developed earlier, which are more robust and computationally efficient for scaling up in HT environment, i.e., the PathFinder and ApproxNEB methods²⁴². To summarize, PathFinder algorithm provides an accurate diffusion path prediction with a simple static electronic charge density calculation of the host structure. The key idea is that when an atom migrates inside a host structure, it moves to avoid atoms or bonds. Consequently, non-reactive migration paths should avoid concentrations of electronic charge density. Thus the electronic charge density available from density function theory (DFT)²⁴³ calculations can be used as the potential landscape within which to estimate the MEP. ApproxNEB uses the predicted path from PathFinder and decouple the multiple-image NEB calculation into a single point relaxation image by image, through constraining several necessary degrees of freedom in relaxation.

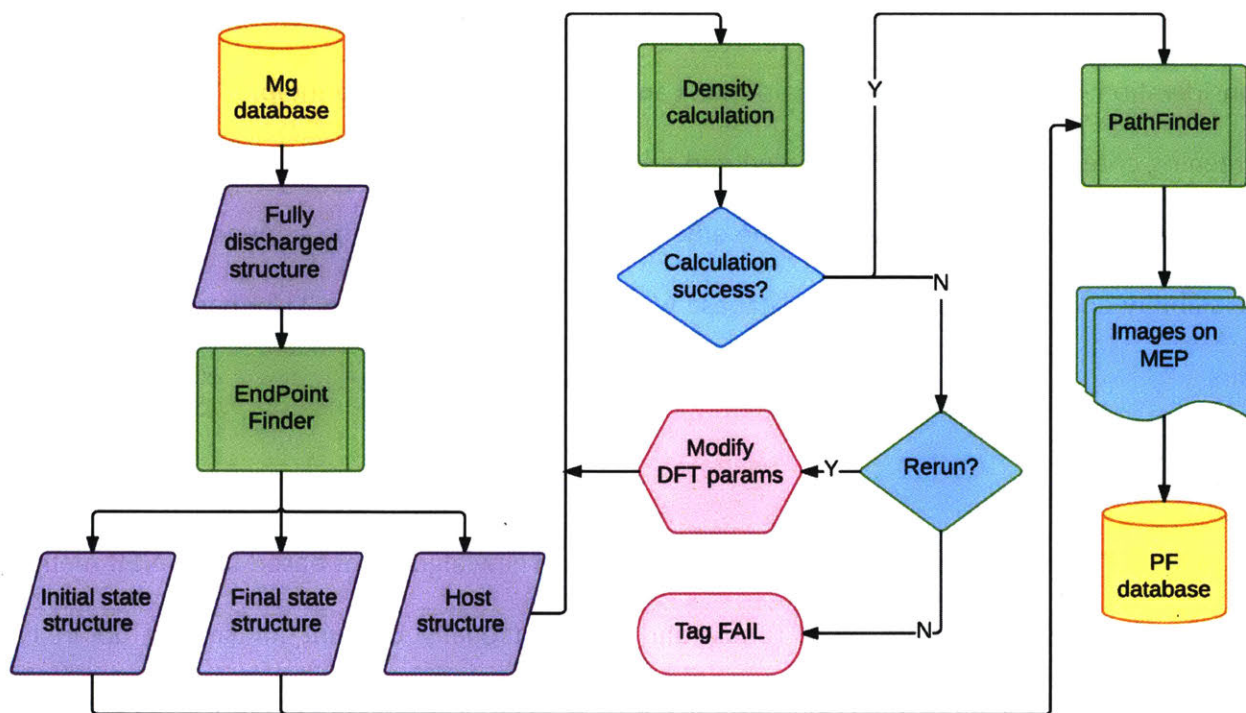


Fig 40. HT PathFinder calculation workflow scheme.

Figure 40 summarizes the PathFinder HT calculation workflow. We start from a fully magnesiated cathode structure drawn from the Mg database. It runs through the EndPointFinder module to identify all geometric unique diffusion paths. Each pair EndPointFinder picks relates to one path to be calculated by PathFinder HT machine. The host structure generated from EndPointFinder is the input discharged structure without any Mg atoms in it. Using Vienna Ab initio simulation package (VASP)^{244, 245}, a static calculation with Γ -point sampling of reciprocal space is performed to obtain the electronic charge density of the host structure. The charge density together with initial and final state structures of the diffusion are provided as input to the PathFinder algorithm. PathFinder algorithm interpolates the MEP and generates image structures. We use 21 images for the PathFinder interpolation and writes 7 image structures periodically into the PathFinder Database.

One discharged structure may generate several possible diffusion paths. These paths share the same host structure, and thus only one VASP calculation is necessary for all of them. If the VASP calculation fails to converge, we adjust the calculation parameters to use easier energy convergence criteria and redo the charge density calculation (more calculation details in Supplementary Materials). And if the calculation fails again, we tag all paths related to that host structure as FAIL in the database and stop pursuing with further calculations.

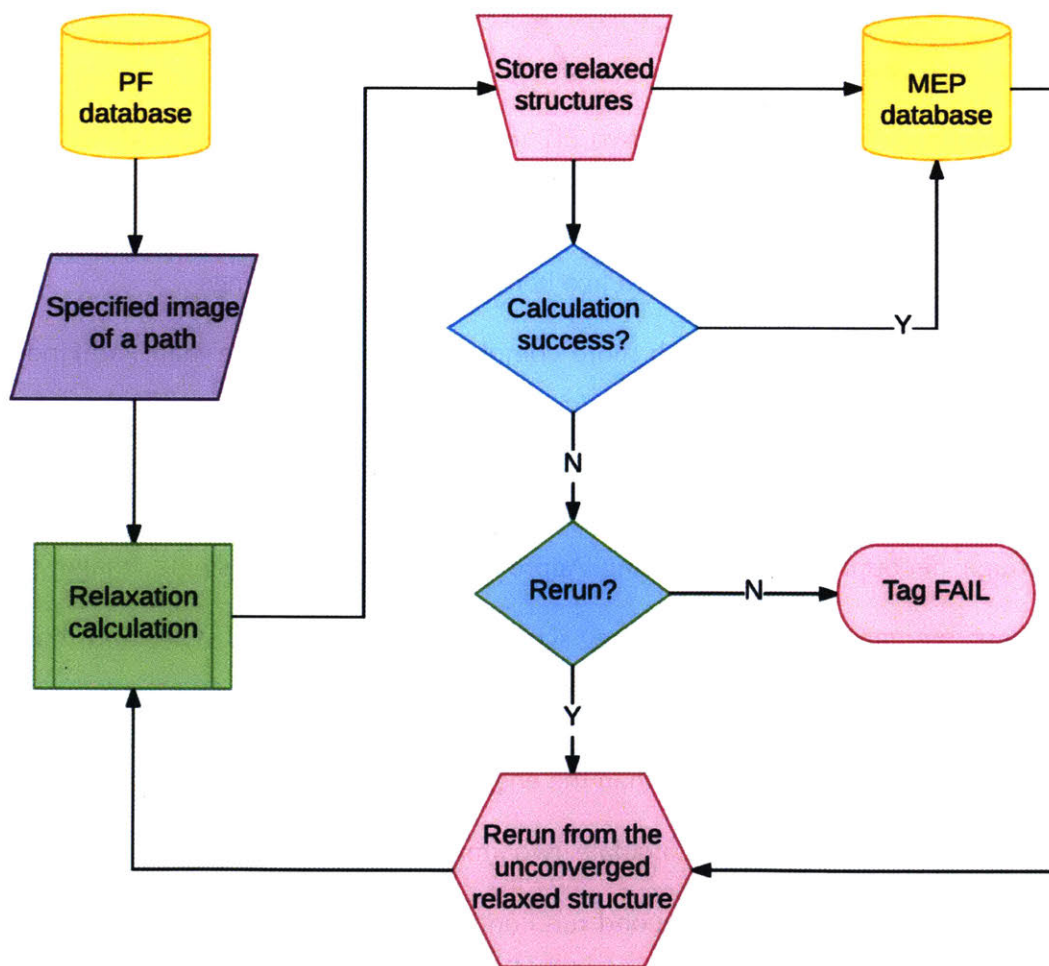


Fig 41. HT ApproxNEB calculation workflow scheme.

Figure 41 depicts the workflow of HT ApproxNEB machinery. Rather than calculating all images of a path to construct the MEP, we designed the workflow at a more atomic level. The HT ApproxNEB machine is able to calculate a designated image at a designated path with proper query into the PathFinder database. After the relaxation calculation job is finished, we store the structure of the last ionic relaxation iteration in the MEP database, no matter whether the calculation is converged or not. If the calculation is successful, the converged energy of the image is stored in MEP database, and if not, the system submits another relaxation job starting from the previous relaxed structure stored in MEP database. The system will tag the image as FAIL after 3 iterations of such repeated calculations.

Though we can integrate the above two HT machines into one unified workflow and obtain the Mg diffusion MEP for a cathode structure. We deliberately separate them with an intermediate PF database acting as the bridge. There are two benefits for this decoupling:

1. ApproxNEB calculation is much more computationally expensive than PathFinder. When two calculations vary a lot in terms computational complexity, it is generally a good idea to decouple them.
2. Through decoupling and designing ApproxNEB machine as a single image calculation process, we can do migration energy screening in a hierarchical style, and thus boosting the computational efficiency by neglecting unnecessary calculations. Because migration barrier has to be equal or larger than the energy difference between any two images on the diffusion path, we can just calculate two images for every path in the first run of HT ApproxNEB, and then in the second run continue to calculate all the other images only if the energy difference between those two images is smaller than the hard criterion, i.e., 600meV. In our case, we calculate the initial state image and the image in the middle of the path, i.e., image No. 0 and image No. 4. In such way, we save around 5/7 (~71.4%)

runtime for barriers we are not interested in, which is very beneficial for HT calculations. Note that in traditional NEB calculation scheme we are not able to do so because traditional NEB calculations relax all the images in parallel in one calculation.

8.5 Code Implementation and Dependencies

The HT computation environment is configured with the open-source project MPWorks (<https://github.com/materialsproject/MPWorks>). The VASP files I/O and PathFinder algorithm are part of the open-source code pymatgen¹⁵⁸ (<https://github.com/materialsproject/pymatgen>). The automation of the workflows as shown in Fig.2 and Fig.3 is powered by the open-source projects FireWorks²⁴⁶ (<https://github.com/materialsproject/fireworks>) and custodian¹⁵⁸ (<https://github.com/materialsproject/custodian>).

8.6 Data Structure

Results of these two HT machines are stored in Mongo databases. The key information stored is listed in Table 3 below. Keys like **mp_id**, **path_index**, **host_struct**, **cation_diff_start**, **cation_diff_end** relate to the EndPointFinder module, where it recognizes one or multiple diffusion paths within a host structure. **Chgcar_dir** and **PF_status** correspond to the VASP electronic charge density calculation. **Path** stores the MEP path interpolated by PathFinder, and we can reconstruct each image by inserting the site stored in **path** into **host_struct**. Only paths that went through HT ApproxNEB machine has a **MEP_energy** key, where it stores the calculation results of either 2 images or all the 7 images, depending on whether the diffusion path are filtered out in the first run. Each image calculation record has three pieces of information:

- **status** is either SUCCESS or FAIL. It records whether the ApproxNEB calculation for that image is successful.

- **energy** stores the energy of that image if the calculation is successful, which can be later used to construct the MEP.
- **file_path** stores the path to the calculation files.

Table 3. Database schema for storing the HT calculation results

Key	Datatype	Description
mp_id	string	ID for the discharged structure in Materials Project
path_index	number	Index number for each path within the same material identified by EndPointFinder, starts at 0
pretty_formula	string	Chemical formula
E_above_hull	number	Energy above the energy hull ²⁴⁷ for the discharged input structure, unit in meV/atom
chgcar_dir	string	File path where the VASP CHGCAR file of the host structure is stored
PF_status	string	SUCCESS or FAIL, a tag for recording the PathFinder machine calculation status for each path
host_struct	JSON	A pymatgen Structure dictionary for the host structure
cation_diff_start	JSON	A pymatgen PeriodicSite dictionary of the Mg site for the diffusion initial state
cation_diff_end	JSON	A pymatgen PeriodicSite dictionary of the Mg site for the diffusion final state
path	list	A list of pymatgen PeriodicSite dictionaries for the Mg sites of each image on the PathFinder predicted MEP
MEP_energy	list	A list of JSONs for the ApproxNEB calculation of each image

8.7 Results

There are 318 unique magnesiated structures in Mg DB. EndPointFinder identifies 551 diffusion paths, which are further calculated by PathFinder and ApproxNEB HT machines. Out of the first run of ApproxNEB HT machine, where only two images are calculated, 93 paths satisfy the 600 meV energy difference criterion. The second run of ApproxNEB HT calculation characterizes the MEPs of these 93 paths and gives 17 unique materials with Mg migration barriers below 600meV. These 17 materials are shown below in Table 4.

Table 4. List of promising Mg cathode structures

Formula	Space group	HT ApproxNEB barrier (meV)	NEB barrier (meV)
MgV ₂ O ₄	Pmnb	133	353
MgMo ₃ P ₃ O ₁₃	P2 ₁ /m	160	147
MgCr ₂ O ₄	Pmnb	174	479
MgMo ₂ P ₂ O ₉	Pmnc	251	359
MgW ₂ P ₂ O ₉	Pmnc	253	455
Mg ₃ Cr ₂ (GeO ₄) ₃	Ia $\bar{3}$ d	293	476
MgNiMoP ₂ O ₉	Pmnc	295	440
MgTi ₂ P ₂ O ₉	Pmnc	388	406
Mg ₃ Ge ₃ (MoO ₆) ₂	Ia $\bar{3}$ d	444	303
MgVNiP ₂ O ₉	Pmnc	450	481
Mg ₃ Fe ₂ (SiO ₄) ₃	Ia $\bar{3}$ d	466	576
MgNi ₂ O ₄	Pmnb	471	666
MgCr ₂ P ₂ O ₉	Pmnc	473	482
MgMn ₂ (PO ₄) ₂	C2/c	525	375
MgMn ₂ P ₂ O ₉	Pmnc	538	442
MgFe ₃ P ₃ O ₁₃	P2 ₁ /m	542	488
MgCrNiP ₂ O ₉	Pmnc	566	504

Firstly, we notice that except from MgMn₂(PO₄)₂ and Mg₃Ge₃(MoO₆)₂, all of the suggested candidates in Table 2 come from 4 structure prototypes. They are MgTM₂P₂O₉ (green), MgTM₃P₃O₁₃ (yellow), post-spinel Pmnb phase (blue) and Garnet phase (orange). The HT machinery consistently suggests materials of the same structural prototype agrees with previous studies which conclude host material structural topology plays an intrinsic part in governing Mg mobility¹²⁴. The reappearance of these 4 structural prototypes also asserts their importance in Mg cathode materials family and suggests further investigation. As a matter of fact, post-spinel phase has been studied and proposed as Mg battery cathode material before^{232, 248}, so is MgMo₃P₃O₁₃. Garnet phase has been previously investigated as a solid-state fast Li ion conductors for Li batteries.^{249, 250} The agreement with past literatures confirms the functionality of our HT tools for screening materials based on migration energy barriers. More detailed properties of these materials can be found on Materials Project Website (<https://www.materialsproject.org/>).

We further validate the HT results by recalculating the barriers using traditional NEB calculation scheme. 7 images are used in these NEB calculations, same as HT ApproxNEB. As shown in Table 2, though the HT ApproxNEB calculated barrier numbers have discrepancies with NEB results, we do find all materials in the list have relatively low NEB barriers. Apart from MgNi_2O_4 , all materials proposed by the HT screening process have barriers below the 600meV hard line. Mover, the differences between HT and NEB results grow smaller when barrier gets larger. We will discuss the reasons for these differences later.

8.8 Recheck Coordination Number Rules

Previous studies^{124, 190, 237, 251} have shown that coordination number (CN) of the Mg ion is a significant indicator for its mobility. In short, a small CN change along the migration path and a deviation from Mg's preferred coordinated environment in the migration initial and final sites are beneficial for Mg ion's mobility. However, these materials design rules are obtained through studying limited number of systems. With over 500 paths calculated, we are now in a position to investigate these simple rules from a much grander view perspective. Extracting results from the PF and MEP databases, we calculate the CN changes and stable site CN of all paths, as exhibited in Fig. 42. The effective CN is calculated through constructing a Voronoi polyhedron around Mg and weight the contribution of each coordinating atom with the solid angle subtended by the associated polyhedron face²⁵².

Mg Migration Path CN Distribution

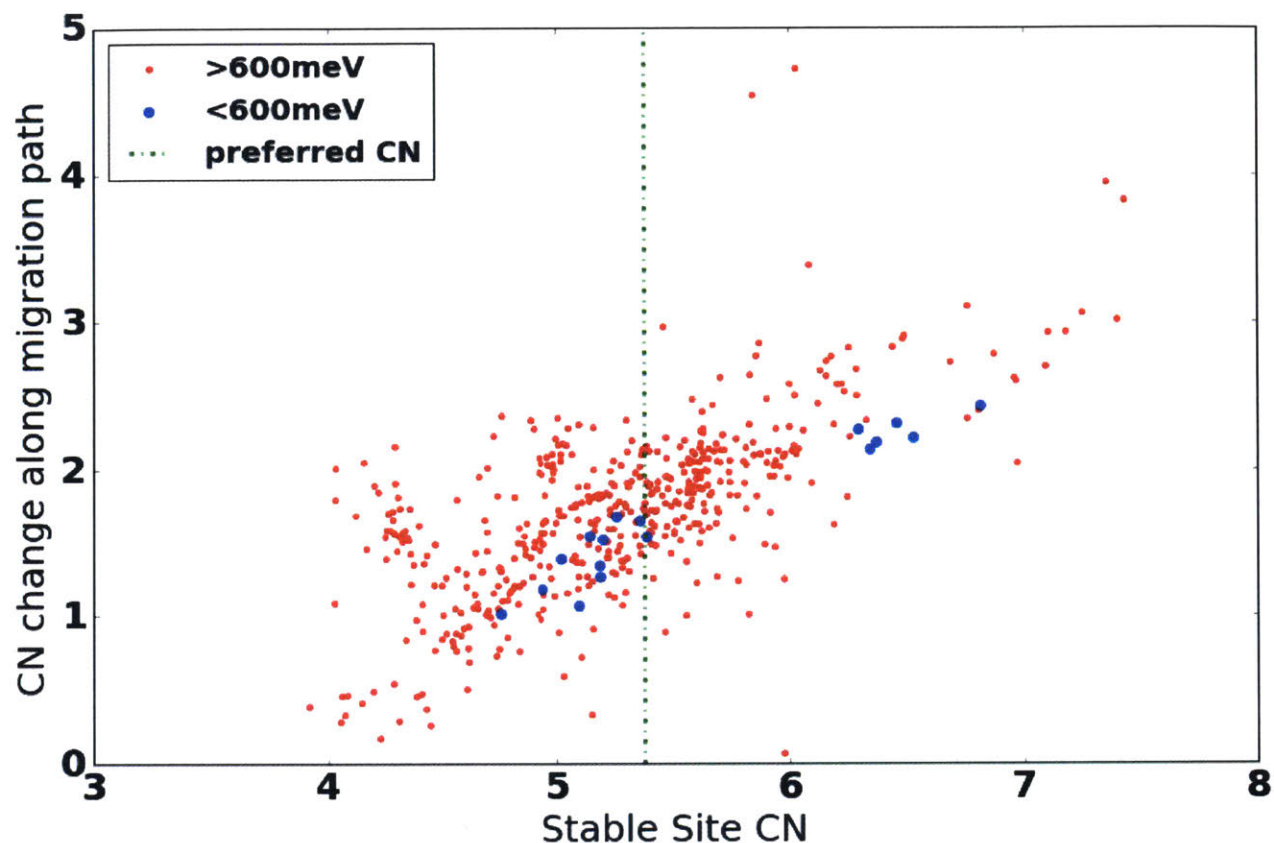


Fig 42. Distribution of stable site coordination numbers and the coordination number changes of all 551 migration paths. The 17 proposed materials' migration paths are highlighted in blue. The preferred coordination number of Mg is calculated through averaging the stable site coordination numbers of all paths.

From Fig. 42, we can see that materials design rules centering around CN are partially correct. Some of the proposed good materials have stable site CN largely deviated from the preferred CN while maintaining a relatively small CN change along the migration path (blue points with x in 6~7). The other proposed materials, though have stable site CN close the preferred CN, bear small CN changes along the paths. Nevertheless, the paths in the left bottom part of Fig. 42 don't present low migration barriers for Mg. And these paths are the ones whose stable site CN

deviate from preferred CN most and have very small CN changes. While the reasons why these paths don't follow coordination number design rules merit further studies, the results in Fig. 42 do show that even though the CN design rules are very effective in explaining the migration barriers in a large number of selected systems, they are not useful in screening for materials with low diffusion barriers for Mg^{2+} .

8.9 HT ApproxNEB errors

We here discuss the main reason that can be attributed for the discrepancies between HT ApproxNEB and NEB barriers. Though ApproxNEB method performs very well in closed pack structures such as olivine and spinel²⁴², its performance worsens in open structures. Because host structure atoms are allowed to relax freely in ApproxNEB calculation scheme, their positional continuity is not guaranteed between adjacent images. Whereas in NEB, though the movement of environmental atoms is negligible, the spring forces among them ensure the movement continuity. This error factor is more significant in open structures like $\text{MgTM}_3\text{P}_3\text{O}_{13}$, $\text{MgTM}_2\text{P}_2\text{O}_9$, Garnet and post-spinel pmb phases, where over half of the polyhedrons are corner-sharing connected, making the polyhedra easy to rotate alongside with Mg^{2+} in the diffusion process. Because host structure atoms' positions are not constrained by spring forces among images, ApproxNEB calculation scheme is not able to ensure that these polyhedral rotations are continual. As a matter of fact, open structures are more favorable for Mg migration as the polyhedron rotates along Mg^{2+} when it migrates and lower the migration energy barriers. From the perspective of counting the number of free relaxation dimensions, ApproxNEB has more freedom in relaxing the environmental atoms as NEB has it in the moving cation. Therefore, in rigid structures where environmental atoms do not move much along with the migrating cation, NEB algorithm has more degrees of freedom and relaxes the system the lower energy states and therefore ApproxNEB tends

to over-estimate the barriers²⁴². Whereas in open structures like MgV_2O_4 , ApproxNEB relaxes the system to a lower energy state and thus delivering an under-estimated barrier comparing to NEB. This error is intrinsic to the ApproxNEB calculation scheme due to the image decoupling and thus is a tradeoff for the runtime it saves. No doubt further work is necessary for improving the ApproxNEB estimation quality. However, considering the fact that materials selected by the HT machine do have low NEB barriers and the enormous amount of computational resources ApproxNEB method manages to save in HT applications, the method itself can be a decent tool in screening for materials with a low migration barrier for designated atoms.

To sum up, in this chapter, we presented a high-throughput migration energy screening framework and applied it to screen for Mg cathode materials with a low migration barrier for Mg^{2+} . One main contribution of this work is that we proposed 17 potentially promising Mg battery cathode materials. We also validate these 17 materials selected by the high-throughput approach indeed have low barriers with the traditional NEB calculations. Moreover, with the high-throughput calculation data of 551 migration paths, we investigate the coordination number rule for materials and find out that even though these rules are useful in explaining the migration barriers in a large number of systems, they are not particularly fit for screening materials with a low barrier. We also discuss the root of HT calculation errors present some ideas for future HT methodology development.

Chapter 9 Case Study: Fast Mg^{2+} Diffusion in $\text{Mo}_3(\text{PO}_4)_3\text{O}$ for Mg Batteries

In this chapter, we study a new possible phosphate compound $\text{Mo}_3(\text{PO}_4)_3\text{O}$ identified by the HT machinery, which is shown to exhibit ultra-fast Mg^{2+} diffusion and relatively high voltage based on

first-principles density functional theory (DFT) calculations. First-principles calculations have proven to be accurate and effective in studying the voltage and mobility of Li-ion^{167, 168, 213-216, 253, 254} and multivalent electrode materials^{124, 190, 237}. Our first-principles nudged elastic band (NEB) calculations^{122, 123, 242} predict that $\text{Mo}_3(\text{PO}_4)_3\text{O}$ has an unusually low Mg migration barrier of ~80 meV, which is lower than the values previously reported for spinel TiS_2 (~550 meV)⁸⁹ and Chevrel phases (~360 meV),²⁵¹ suggesting that this structure may enable very high Mg^{2+} diffusivity.

9.1 Voltages and Diffusivity, etc.

The crystal structure of $\text{MgMo}_3(\text{PO}_4)_3\text{O}$ is shown in Fig. 43. $\text{MgMo}_3(\text{PO}_4)_3\text{O}$ was derived from known compounds such as $\text{CaFe}_3(\text{PO}_4)_3\text{O}$ ²⁵⁵, $\text{SrFe}_3(\text{PO}_4)_3\text{O}$ ²⁵⁶ and $\text{Bi}_{0.4}\text{Fe}_3(\text{PO}_4)_3\text{O}$ ²⁵⁷ by substituting Fe by Mo and the other metal ion (Ca, Sr, Bi) by Mg. The structure is relaxed in both lattice parameters and atomic positions after direct substitutions. Apart from placing Mg in the Ca site in $\text{CaFe}_3(\text{PO}_4)_3\text{O}$ (site B in Fig. 1), we also investigated other possible sites for Mg to reside in the empty host structure $\text{Mo}_3(\text{PO}_4)_3\text{O}$. One site (site A in Fig. 1) is 9.8meV lower in energy than site B. As shown in Fig.1, there are one A site and two B sites in the unit cell, and site A and site B are too close to accommodate Mg cations simultaneously. Hence our calculations predicted that Mg resides in site A at $\text{Mg}_{0.5}\text{Mo}_3(\text{PO}_4)_3\text{O}$ composition and in site B in $\text{MgMo}_3(\text{PO}_4)_3\text{O}$. Chains composed of edge-sharing MoO_6 octahedra along the [010] direction form the backbone of the structure and are interconnected by predominantly corner-sharing MoO_5 trigonal bipyramids, MoO_4 tetrahedra, and PO_4 tetrahedra. Except for the $[\text{Mo}_6\text{O}_{28}]$ chains, there are only two edge-sharing links in the unit cell, which are between PO_4 tetrahedra and MoO_6 octahedra. All the other links between polyhedra are corner-sharing links, which enables the polyhedra to rotate slightly, creating an adaptive tunnel to facilitate Mg^{2+} diffusion. Similar to LiFePO_4 ,²⁰¹ the $\text{MgMo}_3(\text{PO}_4)_3\text{O}$

structure has a 1D diffusion channel along the b-axis, along which Mg^{2+} diffusion is expected to occur.

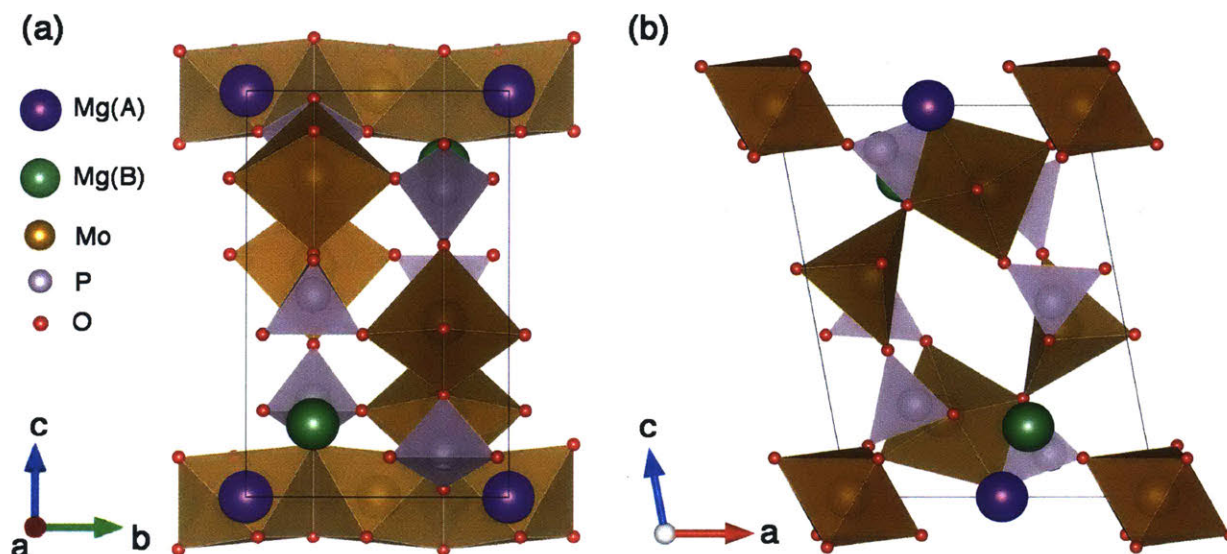


Fig. 43 Crystal structure of $MgMo_3(PO_4)_3O$ in (a) b–c and (b) a–c planes. The structure is built on $[Mo_6O_{28}]$ chains interconnected by predominantly corner-sharing polyhedra. Similar to $LiFePO_4$, a 1D diffusion channel exists along the b-axis for Mg^{2+} .

Fig. 44 shows the minimum energy paths for Mg^{2+} migration in $Mo_3(PO_4)_3O$, as calculated using the NEB method. Mg^{2+} can follow two paths for migration from one stable site to the nearest equivalent site, an inner- or inter-channel path. The inner-channel path involves migration along the **b**-axis direction and across the unit cell boundary (the unit cell is shown in **Fig. 43**), with a very low activation barrier of ~ 80 meV (**Fig. 44(a1, a2)**). The inter-channel path involves migration along the **c**-axis direction with a much higher activation barrier of ~ 1200 meV (**Fig. 44(b1, b2)**). Because diffusivity scales as the inverse exponential of

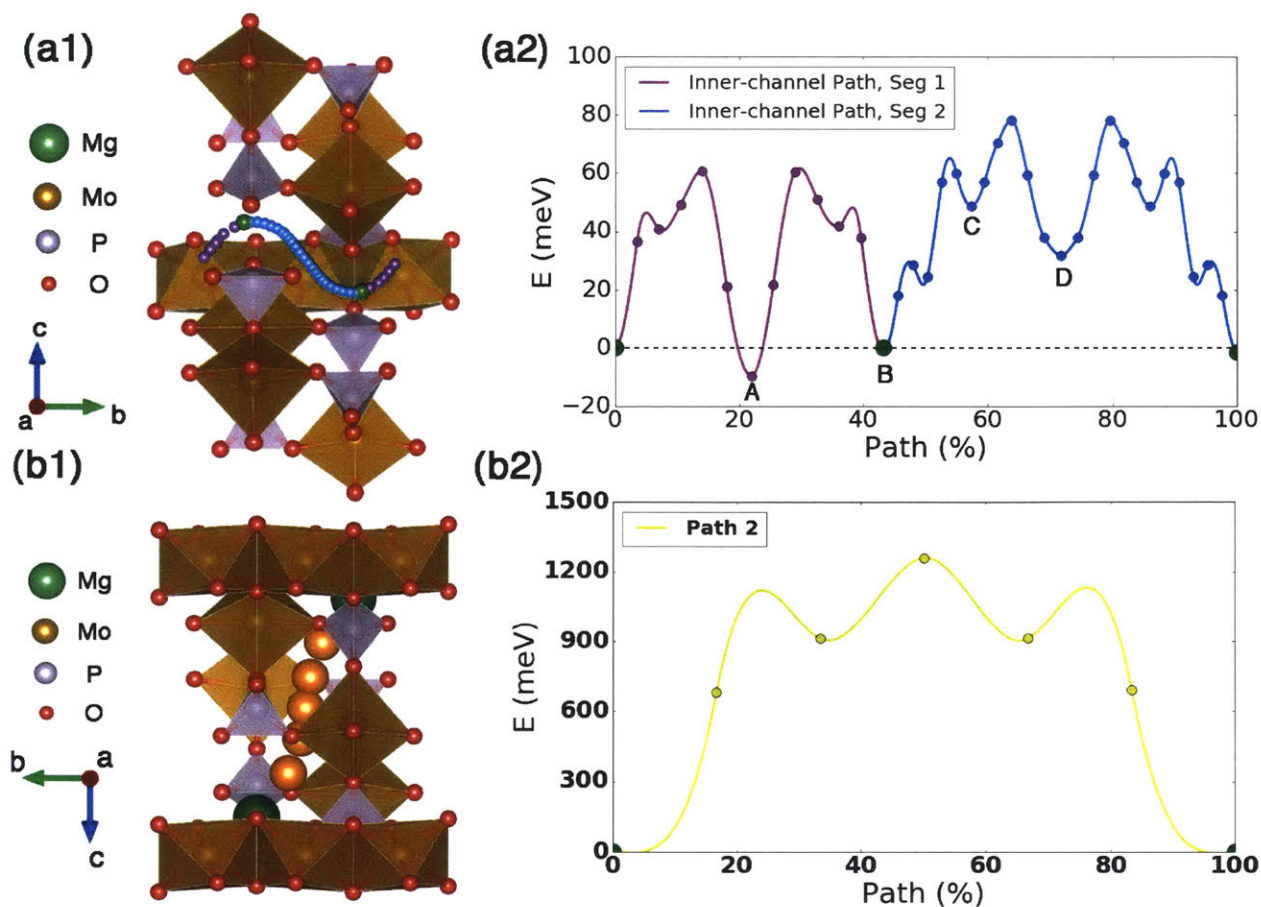


Fig 44. The minimum energy paths for Mg^{2+} migration in $Mo_3(PO_4)_3O$. (a1) Migration path and (a2) minimum energy path for inner-channel diffusion. (b1) Migration path and (b2) minimum energy path for inter-channel diffusion. A, B, C, and D in (a2) are markers for the migration processes. A and B corresponds to site A and B in Fig. 1. The inner-channel diffusion in (a1) and (a2) is the percolation channel for Mg^{2+} intercalation.

the activation barrier, migration along the inter-channel path is unlikely as at room temperature hopping along the c-direction should be $\sim 10^{18}$ times less frequent than along the inner-channel path (an increase of 60 meV in the migration barrier corresponds to a decrease of one order of magnitude in the diffusivity at room temperature)¹²⁴. The percolation channel for Mg^{2+} intercalation is therefore along the inner-channel path. The inner-channel path is divided into two

segments, as shown in **Fig. 44(a1)** and **(a2)**, with migration lengths and activation energies of 5.32 and 7.00 Å and ~80 and ~70 meV, respectively. Multiple minima exist along both paths because the PO₄ groups can easily rotate to accommodate the Mg at different positions. The flexibility of the PO₄ groups is a result of the corner-sharing connection between polyhedrons in the structure.

Table 5. Average voltages of MgMo₃(PO₄)₃O calculated using different levels of theory.

Functionals	Average Voltage	Specific Energy
GGA + U (Mo U=4.38 eV) ^{155, 159, 163}	1.98 V	173 Wh/kg
SCAN ²⁵⁸	1.52 V	133 Wh/kg
HSE06 ²⁵⁹	1.69 V	148 Wh/kg

Table 6. Thermodynamic electrochemical properties of MgMo₃(PO₄)₃O

Mo ₃ (PO ₄) ₃ O Energy Above Hull	MgMo ₃ (PO ₄) ₃ O Energy Above Hull	Volume Change in Charging/Discharging
42 meV/atom	36 meV/atom	2%
Volumetric Capacity	Energy Density	Gravimetric Capacity
330 Ah/L	651 Wh/L	87 mAh/g

Table 5 and Table 6 display the calculated thermodynamic electrochemical properties of MgMo₃(PO₄)₃O. The redox couple during charging and discharging is Mo³⁺/Mo⁴⁺. The average voltage calculated with the GGA(PBE) + U functional is 1.98 V, resulting in a specific energy of 173 Wh/kg. The voltage data and specific energy data were verified using SCAN²⁵⁸ and Heyd–Scuseria–Ernzerhof (HSE)²⁵⁹ functionals. An average voltage of 1.69 V was obtained using the HSE functional, which is generally recognized as the most reliable voltage assessment method²⁶⁰. The voltage from the SCAN functional was close to that of HSE.

Since MgMo₃(PO₄)₃O is a hypothetical compound derived by substituting ions in other compounds, we also evaluate its relative phase stability, by constructing the Mg–Mo–P–O phase diagram using available compounds in the Materials Project Database.¹⁶² Both the charged and

discharged structures are metastable, with a moderate energy above the energy hull of 42 and 36 meV/atom, respectively. These energies measure the driving force to decompose into other phases. A broad analysis of the known compounds in ICSD (Inorganic Crystal Structure Database) has indicated that this energy range for metastability is quite common, indicating the possibility that this compound may be synthesizable.²⁴¹ The charged material is unstable against decomposition to MoO_2 and $\text{Mo}_2\text{P}_3\text{O}_{11}$, and the discharged material is metastable with respect to MoO_2 , $\text{Mo}_2\text{P}_3\text{O}_{11}$, and $\text{Mg}_3(\text{PO}_4)_2$. Based on the energy above the hull for experimentally synthesized Chevrel phases, i. e., Mo_6S_8 (67 meV/atom) and $\text{Mg}_2\text{Mo}_6\text{S}_8$ (49 meV/atom), the stability of $\text{MgMo}_3(\text{PO}_4)_3\text{O}$ is considered reasonable for synthesis. Finally, the volume change during charging and discharging is very small ($\sim 2\%$), which is highly favorable for the reliability of electrodes.

9.2 Verification of the Migration Barrier

To understand the unusually high mobility of Mg^{2+} in this compound, and large difference in activation barriers between the inner- and inter-channel paths, we analyzed the coordination number for Mg^{2+} in every image of the two paths. Mg^{2+} almost always maintains 4-fold coordination along the inner-channel path, which differs greatly from its behavior along the inter-channel path, where Mg^{2+} experiences a coordination number change of $4 \rightarrow 2 \rightarrow 4$. A larger coordination number change has been previously shown to lead to larger site energy differences along the migration path and ultimately to a larger activation barrier.¹²⁴

Moreover, the corner-sharing connections of most of the polyhedra in the structure facilitate Mg^{2+} migration by enabling rotation to accommodate the presence of a local Mg ion. From this perspective, the inner-channel along the **b**-axis is more advantageous than the inter-channel along the **c**-axis because rotation of the MoO_6 octahedra along the edge-sharing [010] $[\text{Mo}_6\text{O}_{28}]$ chains is much easier around the **b**-axis than the **c**-axis. In addition, the void in the middle of the inter-

channel path is too open, and moderate polyhedral rotations cannot mediate the coordination number decrease.

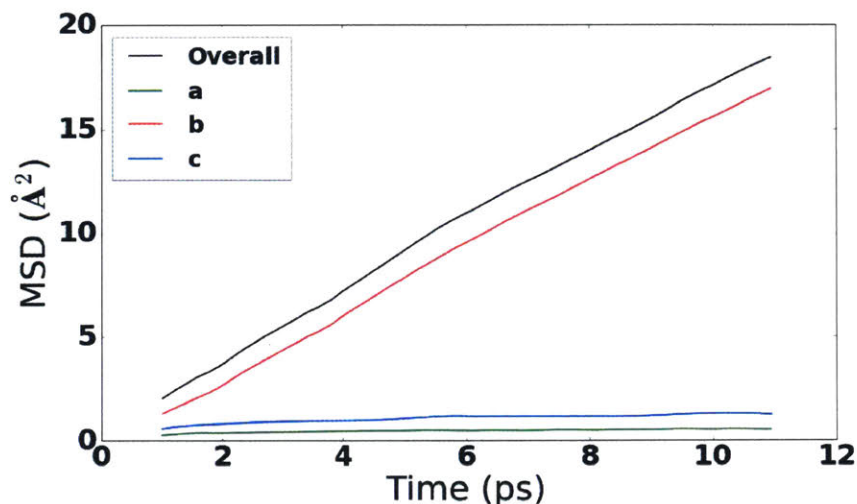


Fig. 45. MSD of Mg²⁺ at 650 K from AIMD simulations. The main contribution of the displacement is along b-axis, which shows a one-dimensional diffusion channel, as indicated by the inner-channel path in Fig. 2 (a1) and (a2).

To verify the migration barriers obtained from zero-K NEB calculations, we performed ab initio molecular dynamics (AIMD) simulations.^{114, 115} The mean square displacement (MSD) at 650 K is plotted in Fig. 45. The main contribution of the displacement is along the **b**-axis, which further confirms the 1D diffusion channel, as indicated by the inner-channel path. The diffusivity calculated using AIMD is $2.82 \times 10^{-5} \text{ cm}^2/\text{s}$.

For comparison, a kinetic Monte Carlo (kMC)^{261, 262} simulation was conducted based on the inner-channel path in Fig. 2 (a2). Hopping rates between local minima were calculated using harmonic transition state theory²⁶³:

$$k = \frac{\prod_{i=1}^{3N} v_i}{\prod_{i=1}^{3N-1} v_i^*} e^{-\Delta E/k_B T} \quad (1)$$

where N is the number of atoms; ν_i and ν_i^* are the positive normal mode frequencies at the local minimum and transition state, respectively; and ΔE is the energy barrier. The pre-factors $\left(\frac{\prod_{i=1}^{3N} \nu_i}{\prod_{i=1}^{3N-1} \nu_i^*}\right)$ and barriers between minima A, B, C, and D in Fig. 2 (a2) are listed in Table 7. The other half of the path is symmetrically equivalent to ABCD.

Table 7. Summary of hopping processes.

Process	Calculated Prefactor (THz)	Barrier (meV)
A→B	1.59	70.4
B→A	0.58	60.6
B→C	0.46	66.5
C→B	2.75	16.5
C→D	8.18	29.5
D→C	2.24	46.3

The diffusivity at 650 K determined using kMC is $13.70 \times 10^{-5} \text{ cm}^2/\text{s}$. The fact that the diffusivities from AIMD and kMC are within one order of magnitude confirms that the effective barrier of diffusion is low. The room temperature (300K) Mg diffusivity estimated using kMC is $4.68 \times 10^{-5} \text{ cm}^2/\text{s}$.

The key property for developing Mg battery cathode materials is the Mg^{2+} cation mobility in the host structure. In this chapter, we show that $\text{Mo}_3(\text{PO}_4)_3\text{O}$ exhibits extraordinarily fast Mg^{2+} cation mobility based on NEB (activation barrier $\sim 80 \text{ meV}$), AIMD (diffusivity $\sim 2.82 \times 10^{-5} \text{ cm}^2/\text{s}$ at 650K), and kMC (diffusivity $\sim 13.70 \times 10^{-5} \text{ cm}^2/\text{s}$ at 650K, $\sim 4.68 \times 10^{-5} \text{ cm}^2/\text{s}$ at 300K) simulations. This is to our knowledge the lowest migration barrier ever predicted for Mg^{2+} in an oxide. Its voltage is slightly higher than previously reported sulfides based on GGA+U (1.98 V), SCAN (1.52 V), and HSE06 (1.69 V) calculations, but the capacity of 91 mAh/g is relatively low. Our systematic first-principles studies indicate that $\text{Mo}_3(\text{PO}_4)_3\text{O}$ may be a promising 1D cathode material for Mg batteries and is worthy of possible experimental investigation. In addition, the

unusually high predicted mobility indicates that while Mg^{2+} diffusion in generally is slow in inorganic compounds, there may be notable exceptions.

Conclusion

In this thesis, we demonstrate the results and progress of developing a high-throughput migration energy calculation machinery and applying it in search for Mg battery cathode materials. We discuss the key challenge of developing functional Mg battery cathode, and propose to use NEB algorithm in high-throughput calculations to screen for materials with good Mg^{2+} diffusivity. However, though NEB algorithm performs quite well on individual systems, due to its very long run-time, it is difficult to be scaled up in high-throughput applications. Therefore, new algorithms are developed and implanted, and 17 potential Mg cathode materials are selected by the new high-throughput system. The main contributions of this thesis are: (1) developed new algorithms for NEB calculations in high-throughput environments; (2) implemented a functional software system for conducting high-throughput migration energy calculations, which can be further applied in other research areas like Ca batteries, Zn batteries, solid state conductors, etc.; (3) proposed new Mg cathode materials.

Reference

1. M. M. Thackeray, C. Wolverton and E. D. Isaacs, *Energy & Environmental Science*, 2012, **5**, 7854-7863.
2. R. Van Noorden, *Nature*, 2014, **507**, 26.
3. B. Nykvist and M. Nilsson, *Nature climate change*, 2015, **5**, 329.
4. B. Diouf and R. Pode, *Renewable Energy*, 2015, **76**, 375-380.
5. M. S. Whittingham, *Chemical reviews*, 2014, **114**, 11414-11443.

6. D. Andre, S.-J. Kim, P. Lamp, S. F. Lux, F. Maglia, O. Paschos and B. Stiaszny, *Journal of Materials Chemistry A*, 2015, **3**, 6709-6732.
7. C. Grey and J. Tarascon, *Nature materials*, 2017, **16**, 45-56.
8. E. Peled, A. Gorenshtein, M. Segal and Y. Sternberg, *Journal of Power Sources*, 1989, **26**, 269-271.
9. Z. Yang, J. Zhang, M. C. Kintner-Meyer, X. Lu, D. Choi, J. P. Lemmon and J. Liu, *Chemical reviews*, 2011, **111**, 3577-3613.
10. P. G. Bruce, S. A. Freunberger, L. J. Hardwick and J.-M. Tarascon, *Nature materials*, 2012, **11**, 19.
11. L. F. Nazar, M. Cuisinier and Q. Pang, *MRS Bulletin*, 2014, **39**, 436-442.
12. A. Manthiram, Y. Fu, S.-H. Chung, C. Zu and Y.-S. Su, *Chemical reviews*, 2014, **114**, 11751-11787.
13. D. Aurbach, Z. Lu, A. Schechter, Y. Gofer, H. Gizbar, R. Turgeman, Y. Cohen, M. Moshkovich and E. Levi, *Nature*, 2000, **407**, 724-727.
14. H. D. Yoo, I. Shterenberg, Y. Gofer, G. Gershinsky, N. Pour and D. Aurbach, *Energy & Environmental Science*, 2013, **6**, 2265-2279.
15. J. O. Besenhard and M. Winter, *ChemPhysChem*, 2002, **3**, 155-159.
16. A. Ponrouch, C. Frontera, F. Bardé and M. R. Palacín, *Nature materials*, 2016, **15**, 169.
17. D. Aurbach, *Journal of Power Sources*, 2000, **89**, 206-218.
18. D. Aurbach, E. Zinigrad, Y. Cohen and H. Teller, *Solid state ionics*, 2002, **148**, 405-416.
19. D. Larcher, S. Beattie, M. Morcrette, K. Edstroem, J.-C. Jumas and J.-M. Tarascon, *Journal of Materials Chemistry*, 2007, **17**, 3759-3772.
20. A. L. Lipson, S.-D. Han, B. Pan, K. A. See, A. A. Gewirth, C. Liao, J. T. Vaughey and B. J. Ingram, *Journal of The Electrochemical Society*, 2016, **163**, A2253-A2257.
21. N. Pour, Y. Gofer, D. T. Major and D. Aurbach, *Journal of the American Chemical Society*, 2011, **133**, 6270-6278.
22. D. Aurbach, G. S. Suresh, E. Levi, A. Mitelman, O. Mizrahi, O. Chusid and M. Brunelli, *Advanced Materials*, 2007, **19**, 4260-4267.
23. O. Mizrahi, N. Amir, E. Pollak, O. Chusid, V. Marks, H. Gottlieb, L. Larush, E. Zinigrad and D. Aurbach, *Journal of the Electrochemical Society*, 2008, **155**, A103-A109.
24. H. S. Kim, T. S. Arthur, G. D. Allred, J. Zajicek, J. G. Newman, A. E. Rodnyansky, A. G. Oliver, W. C. Boggess and J. Muldoon, *Nature communications*, 2011, **2**, 427.
25. J. Muldoon, C. B. Bucur, A. G. Oliver, T. Sugimoto, M. Matsui, H. S. Kim, G. D. Allred, J. Zajicek and Y. Kotani, *Energy & Environmental Science*, 2012, **5**, 5941-5950.
26. Y.-s. Guo, F. Zhang, J. Yang, F.-f. Wang, Y. NuLi and S.-i. Hirano, *Energy & Environmental Science*, 2012, **5**, 9100-9106.
27. Y. Guo, F. Zhang, J. Yang and F. Wang, *Electrochemistry Communications*, 2012, **18**, 24-27.
28. R. E. Doe, R. Han, J. Hwang, A. J. Gmitter, I. Shterenberg, H. D. Yoo, N. Pour and D. Aurbach, *Chemical communications*, 2014, **50**, 243-245.
29. C. J. Barile, E. C. Barile, K. R. Zavadil, R. G. Nuzzo and A. A. Gewirth, *The Journal of Physical Chemistry C*, 2014, **118**, 27623-27630.
30. C. J. Barile, R. Spatney, K. R. Zavadil and A. A. Gewirth, *The Journal of Physical Chemistry C*, 2014, **118**, 10694-10699.
31. P. Canepa, G. S. Gautam, R. Malik, S. Jayaraman, Z. Rong, K. R. Zavadil, K. Persson and G. Ceder, *Chemistry of Materials*, 2015, **27**, 3317-3325.
32. K. A. See, K. W. Chapman, L. Zhu, K. M. Wiaderek, O. J. Borkiewicz, C. J. Barile, P. J. Chupas and A. A. Gewirth, *Journal of the American Chemical Society*, 2015, **138**, 328-337.
33. T. J. Carter, R. Mohtadi, T. S. Arthur, F. Mizuno, R. Zhang, S. Shirai and J. W. Kampf, *Angewandte Chemie International Edition*, 2014, **53**, 3173-3177.
34. S. H. Lapidus, N. N. Rajput, X. Qu, K. W. Chapman, K. A. Persson and P. J. Chupas, *Physical Chemistry Chemical Physics*, 2014, **16**, 21941-21945.

35. N. N. Rajput, X. Qu, N. Sa, A. K. Burrell and K. A. Persson, *Journal of the American Chemical Society*, 2015, **137**, 3411-3420.
36. J. Song, E. Sahadeo, M. Noked and S. B. Lee, *The journal of physical chemistry letters*, 2016, **7**, 1736-1749.
37. J. Muldoon, C. B. Bucur, A. G. Oliver, J. Zajicek, G. D. Allred and W. C. Boggess, *Energy & Environmental Science*, 2013, **6**, 482-487.
38. J. Muldoon, C. B. Bucur and T. Gregory, *Chemical reviews*, 2014, **114**, 11683-11720.
39. C. B. Bucur, T. Gregory, A. G. Oliver and J. Muldoon, *J. Phys. Chem. Lett.*, 2015, **6**, 3578-3591.
40. C. B. Bucur, T. Gregory and J. Muldoon, in *Rechargeable Batteries*, Springer, 2015, pp. 611-635.
41. J. H. Ha, B. Adams, J.-H. Cho, V. Duffort, J. H. Kim, K. Y. Chung, B. W. Cho, L. F. Nazar and S. H. Oh, *Journal of Materials Chemistry A*, 2016, **4**, 7160-7164.
42. N. Sa, B. Pan, A. Saha-Shah, A. A. Hubaud, J. T. Vaughey, L. A. Baker, C. Liao and A. K. Burrell, *ACS applied materials & interfaces*, 2016, **8**, 16002-16008.
43. E. N. Keyzer, H. F. Glass, Z. Liu, P. M. Bayley, S. E. Dutton, C. P. Grey and D. S. Wright, *Journal of the American Chemical Society*, 2016, **138**, 8682-8685.
44. G. A. Giffin, *Journal of Materials Chemistry A*, 2016, **4**, 13378-13389.
45. M. Salama, I. Shterenberg, H. Gizbar, N. N. Eliaz, M. Kosa, K. Keinan-Adamsky, M. Afri, L. J. Shimon, H. E. Gottlieb and D. T. Major, *The Journal of Physical Chemistry C*, 2016, **120**, 19586-19594.
46. O. Tutusaus, R. Mohtadi, N. Singh, T. S. Arthur and F. Mizuno, *ACS Energy Letters*, 2016.
47. Z. Lu, A. Schechter, M. Moshkovich and D. Aurbach, *Journal of Electroanalytical Chemistry*, 1999, **466**, 203-217.
48. T. D. Gregory, R. J. Hoffman and R. C. Winterton, *Journal of The Electrochemical Society*, 1990, **137**, 775-780.
49. D. Aurbach, H. Gizbar, A. Schechter, O. Chusid, H. E. Gottlieb, Y. Gofer and I. Goldberg, *Journal of The Electrochemical Society*, 2002, **149**, A115-A121.
50. Y. Shao, T. Liu, G. Li, M. Gu, Z. Nie, M. Engelhard, J. Xiao, D. Lv, C. Wang and J.-G. Zhang, *Scientific reports*, 2013, **3**.
51. O. Tutusaus, R. Mohtadi, T. S. Arthur, F. Mizuno, E. G. Nelson and Y. V. Sevryugina, *Angewandte Chemie International Edition*, 2015, **54**, 7900-7904.
52. R. Mohtadi, M. Matsui, T. S. Arthur and S. J. Hwang, *Angewandte Chemie International Edition*, 2012, **51**, 9780-9783.
53. E. Peled, *Journal of The Electrochemical Society*, 1979, **126**, 2047-2051.
54. D. Aurbach, R. Skaletsky and Y. Gofer, *Journal of The Electrochemical Society*, 1991, **138**, 3536-3545.
55. L. F. Wan, B. R. Perdue, C. A. Apblett and D. Prendergast, *Chemistry of Materials*, 2015, **27**, 5932-5940.
56. F. Wu, H. Zhou, Y. Bai, H. Wang and C. Wu, *ACS applied materials & interfaces*, 2015, **7**, 15098-15107.
57. S. Terada, T. Mandai, S. Suzuki, S. Tsuzuki, K. Watanabe, Y. Kamei, K. Ueno, K. Dokko and M. Watanabe, *The Journal of Physical Chemistry C*, 2016, **120**, 1353-1365.
58. G. Gershinsky, H. D. Yoo, Y. Gofer and D. Aurbach, *Langmuir*, 2013, **29**, 10964-10972.
59. A. Baskin and D. Prendergast, *The Journal of Physical Chemistry C*, 2016, **120**, 3583-3594.
60. J. G. Connell, B. Genorio, P. P. Lopes, D. Strmcnik, V. R. Stamenkovic and N. M. Markovic, *Chemistry of Materials*, 2016, **28**, 8268-8277.
61. N. Sa, N. N. Rajput, H. Wang, B. Key, M. Ferrandon, V. Srinivasan, K. A. Persson, A. K. Burrell and J. T. Vaughey, *RSC Advances*, 2016, **6**, 113663-113670.
62. N. Kumar and D. J. Siegel, *The journal of physical chemistry letters*, 2016, **7**, 874-881.

63. T. Watkins, A. Kumar and D. A. Buttry, *J. Am. Chem. Soc.*, 2016, **138**, 641-650.
64. M. Park, X. Zhang, M. Chung, G. B. Less and A. M. Sastry, *Journal of Power Sources*, 2010, **195**, 7904-7929.
65. B. Wang, J. Bates, F. Hart, B. Sales, R. Zuhr and J. Robertson, *Journal of The Electrochemical Society*, 1996, **143**, 3203-3213.
66. R. Amin, P. Balaya and J. Maier, *Electrochemical and solid-state letters*, 2007, **10**, A13-A16.
67. A. Van der Ven, J. Bhattacharya and A. A. Belak, *Accounts of chemical research*, 2012, **46**, 1216-1225.
68. A. Van der Ven and G. Ceder, *Electrochemical and Solid-State Letters*, 2000, **3**, 301-304.
69. K. Kang and G. Ceder, *Physical Review B*, 2006, **74**, 094105.
70. D. Morgan, A. Van der Ven and G. Ceder, *Electrochemical and solid-state letters*, 2004, **7**, A30-A32.
71. M. S. Islam, D. J. Driscoll, C. A. Fisher and P. R. Slater, *Chemistry of Materials*, 2005, **17**, 5085-5092.
72. M. S. Islam and C. A. Fisher, *Chemical Society Reviews*, 2014, **43**, 185-204.
73. E. Levi, M. Levi, O. Chasid and D. Aurbach, *Journal of electroceramics*, 2009, **22**, 13-19.
74. W. McKinnon and J. Dahn, *Physical Review B*, 1985, **31**, 3084.
75. K. Kganyago, P. Ngoepe and C. Catlow, *Physical Review B*, 2003, **67**, 104103.
76. E. Levi, E. Lancry, A. Mitelman, D. Aurbach, G. Ceder, D. Morgan and O. Isnard, *Chemistry of materials*, 2006, **18**, 5492-5503.
77. E. Levi, G. Gershinsky, D. Aurbach and O. Isnard, *Inorganic chemistry*, 2009, **48**, 8751-8758.
78. T. Kaewmaraya, M. Ramzan, J. Osorio-Guillen and R. Ahuja, *Solid State Ionics*, 2014, **261**, 17-20.
79. A. Mitelman, M. Levi, E. Lancry, E. Levi and D. Aurbach, *Chemical Communications*, 2007, 4212-4214.
80. E. Levi, A. Mitelman, D. Aurbach and M. Brunelli, *Chemistry of Materials*, 2007, **19**, 5131-5142.
81. P. Saha, P. H. Jampani, M. K. Datta, C. U. Okoli, A. Manivannan and P. N. Kumta, *Journal of The Electrochemical Society*, 2014, **161**, A593-A598.
82. E. Lancry, E. Levi, Y. Gofer, M. Levi, G. Salitra and D. Aurbach, *Chemistry of materials*, 2004, **16**, 2832-2838.
83. R. Schöllhorn, M. Kümpers and J. Besenhard, *Materials Research Bulletin*, 1977, **12**, 781-788.
84. Y. Cheng, L. R. Parent, Y. Shao, C. Wang, V. L. Sprenkle, G. Li and J. Liu, *Chemistry of Materials*, 2014, **26**, 4904-4907.
85. E. Levi, G. Gershinsky, D. Aurbach, O. Isnard and G. Ceder, *Chemistry of Materials*, 2009, **21**, 1390-1399.
86. M. Levi, E. Lancry, H. Gizbar, Z. Lu, E. Levi, Y. Gofer and D. Aurbach, *Journal of the Electrochemical Society*, 2004, **151**, A1044-A1051.
87. S.-H. Choi, J.-S. Kim, S.-G. Woo, W. Cho, S. Y. Choi, J. Choi, K.-T. Lee, M.-S. Park and Y.-J. Kim, *ACS applied materials & interfaces*, 2015, **7**, 7016-7024.
88. S.-G. Woo, J.-Y. Yoo, W. Cho, M.-S. Park, K. J. Kim, J.-H. Kim, J.-S. Kim and Y.-J. Kim, *RSC Advances*, 2014, **4**, 59048-59055.
89. X. Sun, P. Bonnicksen, V. Duffort, M. Liu, Z. Rong, K. A. Persson, G. Ceder and L. F. Nazar, *Energy & Environmental Science*, 2016, **9**, 2273-2277.
90. A. Emly and A. Van der Ven, *Inorganic chemistry*, 2015, **54**, 4394-4402.
91. H. Rietveld, *Journal of applied Crystallography*, 1969, **2**, 65-71.
92. W. Weppner and R. A. Huggins, *Journal of The Electrochemical Society*, 1977, **124**, 1569-1578.
93. P. Lightfoot, F. Krok, J. L. Nowinski and P. G. Bruce, *Journal of Materials Chemistry*, 1992, **2**, 139-140.

94. I. E. Castelli, D. D. Landis, K. S. Thygesen, S. Dahl, I. Chorkendorff, T. F. Jaramillo and K. W. Jacobsen, *Energy & Environmental Science*, 2012, **5**, 9034-9043.
95. I. E. Castelli, T. Olsen, S. Datta, D. D. Landis, S. Dahl, K. S. Thygesen and K. W. Jacobsen, *Energy & Environmental Science*, 2012, **5**, 5814-5819.
96. L. Yu and A. Zunger, *Physical review letters*, 2012, **108**, 068701.
97. K. Yang, W. Setyawan, S. Wang, M. B. Nardelli and S. Curtarolo, *Nature materials*, 2012, **11**, 614.
98. C. Ortiz, O. Eriksson and M. Klintonberg, *Computational Materials Science*, 2009, **44**, 1042-1049.
99. W. Setyawan, R. M. Gaume, S. Lam, R. S. Feigelson and S. Curtarolo, *ACS combinatorial science*, 2011, **13**, 382-390.
100. L.-C. Lin, A. H. Berger, R. L. Martin, J. Kim, J. A. Swisher, K. Jariwala, C. H. Rycroft, A. S. Bhowm, M. W. Deem and M. Haranczyk, *Nature materials*, 2012, **11**, 633.
101. R. Armiento, B. Kozinsky, M. Fornari and G. Ceder, *Physical Review B*, 2011, **84**, 014103.
102. S. Wang, Z. Wang, W. Setyawan, N. Mingo and S. Curtarolo, *Physical Review X*, 2011, **1**, 021012.
103. S. Curtarolo, W. Setyawan, S. Wang, J. Xue, K. Yang, R. H. Taylor, L. J. Nelson, G. L. Hart, S. Sanvito and M. Buongiorno-Nardelli, *Computational Materials Science*, 2012, **58**, 227-235.
104. J. Greeley, T. F. Jaramillo, J. Bonde, I. Chorkendorff and J. K. Nørskov, *Nature materials*, 2006, **5**, 909.
105. S. V. Alapati, J. K. Johnson and D. S. Sholl, *The Journal of Physical Chemistry B*, 2006, **110**, 8769-8776.
106. J. Lu, Z. Z. Fang, Y. J. Choi and H. Y. Sohn, *The Journal of Physical Chemistry C*, 2007, **111**, 12129-12134.
107. J. C. Kim, C. J. Moore, B. Kang, G. Hautier, A. Jain and G. Ceder, *Journal of the Electrochemical Society*, 2011, **158**, A309-A315.
108. H. Chen, G. Hautier, A. Jain, C. Moore, B. Kang, R. Doe, L. Wu, Y. Zhu, Y. Tang and G. Ceder, *Chemistry of Materials*, 2012, **24**, 2009-2016.
109. A. Jain, G. Hautier, C. Moore, B. Kang, J. Lee, H. Chen, N. Twu and G. Ceder, *Journal of The Electrochemical Society*, 2012, **159**, A622-A633.
110. G. Hautier, A. Jain, H. Chen, C. Moore, S. P. Ong and G. Ceder, *Journal of Materials Chemistry*, 2011, **21**, 17147-17153.
111. H. Chen, G. Hautier and G. Ceder, *Journal of the American Chemical Society*, 2012, **134**, 19619-19627.
112. P. Pechukas, *Annual Review of Physical Chemistry*, 1981, **32**, 159-177.
113. D. G. Truhlar, B. C. Garrett and S. J. Klippenstein, *The Journal of physical chemistry*, 1996, **100**, 12771-12800.
114. G. Kresse and J. Hafner, *Physical Review B*, 1993, **47**, 558.
115. G. Kresse and J. Hafner, *Physical Review B*, 1993, **48**, 13115.
116. K. J. Laidler, *J. Chem. Educ*, 1984, **61**, 494.
117. H. Eyring, *The Journal of Chemical Physics*, 1935, **3**, 107-115.
118. E. Wigner, *Transactions of the Faraday Society*, 1938, **34**, 29-41.
119. T. Clark, *Advanced Materials*, 1994, **6**, 88-88.
120. H. Jónsson, G. Mills and K. W. Jacobsen, 1998.
121. G. Henkelman, G. Jóhannesson and H. Jónsson, in *Theoretical Methods in Condensed Phase Chemistry*, Springer, 2002, pp. 269-302.
122. G. Mills and H. Jónsson, *Physical review letters*, 1994, **72**, 1124.
123. G. Mills, H. Jónsson and G. K. Schenter, *Surface Science*, 1995, **324**, 305-337.
124. Z. Rong, R. Malik, P. Canepa, G. Sai Gautam, M. Liu, A. Jain, K. Persson and G. Ceder, *Chemistry of Materials*, 2015, **27**, 6016-6021.

125. B. J. Berne, G. Ciccotti and D. F. Coker, *Classical and quantum dynamics in condensed phase simulations*, World Scientific, 1998.
126. B. P. Uberuaga, M. Leskovar, A. P. Smith, H. Jónsson and M. Olmstead, *Physical review letters*, 2000, **84**, 2441.
127. W. Windl, M. Bunea, R. Stumpf, S. Dunham and M. Masquelier, *Physical review letters*, 1999, **83**, 4345.
128. R. Stumpf, C.-L. Liu and C. Tracy, *Physical Review B*, 1999, **59**, 16047.
129. T.-C. Shen, J. Steckel and K. D. Jordan, *Surface science*, 2000, **446**, 211-218.
130. M. Villarba and H. Jónsson, *Surface science*, 1994, **317**, 15-36.
131. M. Villarba and H. Jónsson, *Surface science*, 1995, **324**, 35-46.
132. M. R. Sørensen, K. W. Jacobsen and H. Jónsson, *Physical review letters*, 1996, **77**, 5067.
133. T. Rasmussen, K. W. Jacobsen, T. Leffers, O. B. Pedersen, S. Srinivasan and H. Jonsson, *Physical Review Letters*, 1997, **79**, 3676.
134. R. Elber and M. Karplus, *Chemical Physics Letters*, 1987, **139**, 375-380.
135. R. E. Gillilan and K. R. Wilson, *The Journal of chemical physics*, 1992, **97**, 1757-1772.
136. G. Henkelman, B. P. Uberuaga and H. Jónsson, *The Journal of chemical physics*, 2000, **113**, 9901-9904.
137. G. Henkelman and H. Jónsson, *The Journal of chemical physics*, 2000, **113**, 9978-9985.
138. P. Maragakis, S. A. Andreev, Y. Brumer, D. R. Reichman and E. Kaxiras, *The Journal of chemical physics*, 2002, **117**, 4651-4658.
139. D. Sheppard, P. Xiao, W. Chemelewski, D. D. Johnson and G. Henkelman, *The Journal of chemical physics*, 2012, **136**, 074103.
140. R. Crehuet and M. J. Field, *The Journal of chemical physics*, 2003, **118**, 9563-9571.
141. D. Sheppard, R. Terrell and G. Henkelman, *The Journal of chemical physics*, 2008, **128**, 134106.
142. J.-W. Chu, B. L. Trout and B. R. Brooks, *The Journal of chemical physics*, 2003, **119**, 12708-12717.
143. M. Thackeray, W. David, P. Bruce and J. Goodenough, *Materials Research Bulletin*, 1983, **18**, 461-472.
144. M. M. Thackeray, *Progress in Solid State Chemistry*, 1997, **25**, 1-71.
145. Y. Terada, K. Yasaka, F. Nishikawa, T. Konishi, M. Yoshio and I. Nakai, *Journal of Solid State Chemistry*, 2001, **156**, 286-291.
146. K. Amine, H. Tukamoto, H. Yasuda and Y. Fujita, *Journal of The Electrochemical Society*, 1996, **143**, 1607-1613.
147. H. Kawai, M. Nagata, H. Kageyama, H. Tukamoto and A. R. West, *Electrochimica acta*, 1999, **45**, 315-327.
148. D. Liu, Y. Lu and J. B. Goodenough, *Journal of the Electrochemical Society*, 2010, **157**, A1269-A1273.
149. N. N. Sinha and N. Munichandraiah, *Electrochemical and Solid-State Letters*, 2008, **11**, F23-F26.
150. C. Xu, H. Du, B. Li, F. Kang and Y. Zeng, *Electrochemical and Solid-State Letters*, 2009, **12**, A61-A65.
151. C. Yuan, Y. Zhang, Y. Pan, X. Liu, G. Wang and D. Cao, *Electrochimica Acta*, 2014, **116**, 404-412.
152. F. Zhou, M. Cococcioni, C. A. Marianetti, D. Morgan and G. Ceder, *Physical Review B*, 2004, **70**, 235121.
153. J. Zhou, Q. Wang, Q. Sun, X. Chen, Y. Kawazoe and P. Jena, *Nano letters*, 2009, **9**, 3867-3870.
154. G. Kresse and D. Joubert, *Physical Review B*, 1999, **59**, 1758.
155. Z. Wu and R. E. Cohen, *Physical Review B*, 2006, **73**, 235116.
156. J. P. Perdew, K. Burke and M. Ernzerhof, *Physical review letters*, 1996, **77**, 3865.
157. A. Jain, S. P. Ong, G. Hautier, W. Chen, W. D. Richards, S. Dacek, S. Cholia, D. Gunter, D. Skinner and G. Ceder, *Apl Materials*, 2013, **1**, 011002.

158. S. P. Ong, W. D. Richards, A. Jain, G. Hautier, M. Kocher, S. Cholia, D. Gunter, V. L. Chevrier, K. A. Persson and G. Ceder, *Computational Materials Science*, 2013, **68**, 314-319.
159. L. Wang, T. Maxisch and G. Ceder, *Physical Review B*, 2006, **73**, 195107.
160. M. Aydinol and G. Ceder, *Journal of the Electrochemical Society*, 1997, **144**, 3832-3835.
161. M. Aydinol, A. Kohan, G. Ceder, K. Cho and J. Joannopoulos, *Physical Review B*, 1997, **56**, 1354.
162. S. Ping Ong, L. Wang, B. Kang and G. Ceder, *Chemistry of Materials*, 2008, **20**, 1798-1807.
163. A. Jain, G. Hautier, S. P. Ong, C. J. Moore, C. C. Fischer, K. A. Persson and G. Ceder, *Physical Review B*, 2011, **84**, 045115.
164. S. P. Ong, A. Jain, G. Hautier, B. Kang and G. Ceder, *Electrochemistry Communications*, 2010, **12**, 427-430.
165. L. Wang, T. Maxisch and G. Ceder, *Chemistry of materials*, 2007, **19**, 543-552.
166. J. P. Perdew, J. A. Chevary, S. H. Vosko, K. A. Jackson, M. R. Pederson, D. J. Singh and C. Fiolhais, *Physical Review B*, 1992, **46**, 6671.
167. S. P. Ong, V. L. Chevrier, G. Hautier, A. Jain, C. Moore, S. Kim, X. Ma and G. Ceder, *Energy & Environmental Science*, 2011, **4**, 3680-3688.
168. G. K. P. Dathar, D. Sheppard, K. J. Stevenson and G. Henkelman, *Chemistry of Materials*, 2011, **23**, 4032-4037.
169. H. Lin, Y. Wen, C. Zhang, L. Zhang, Y. Huang, B. Shan and R. Chen, *Solid State Communications*, 2012, **152**, 999-1003.
170. B. Xu and S. Meng, *Journal of Power Sources*, 2010, **195**, 4971-4976.
171. K. Amine, H. Tukamoto, H. Yasuda and Y. Fujita, *Journal of Power Sources*, 1997, **68**, 604-608.
172. J. Bhattacharya and C. Wolverton, *Physical Chemistry Chemical Physics*, 2013, **15**, 6486-6498.
173. E. Gocke, R. Schöllhorn, G. Aselmann and W. Müller-Warmuth, *Inorganic Chemistry*, 1987, **26**, 1805-1812.
174. M. Morita, N. Yoshimoto, S. Yakushiji and M. Ishikawa, *Electrochemical and Solid-State Letters*, 2001, **4**, A177-A179.
175. S. Wang, Z. Lu, D. Wang, C. Li, C. Chen and Y. Yin, *Journal of Materials Chemistry*, 2011, **21**, 6365-6369.
176. K. H. Seng, J. Liu, Z. P. Guo, Z. X. Chen, D. Jia and H. K. Liu, *Electrochemistry Communications*, 2011, **13**, 383-386.
177. A. Van der Ven, C. Marianetti, D. Morgan and G. Ceder, *Solid State Ionics*, 2000, **135**, 21-32.
178. J. Lee, A. Urban, X. Li, D. Su, G. Hautier and G. Ceder, *Science*, 2014, **343**, 519-522.
179. C. Marianetti, D. Morgan and G. Ceder, *Physical Review B*, 2001, **63**, 224304.
180. G. Hautier, S. P. Ong, A. Jain, C. J. Moore and G. Ceder, *Physical Review B*, 2012, **85**, 155208.
181. G. Bergerhoff, I. Brown and F. Allen, *International Union of Crystallography, Chester*, 1987, **360**, 77-95.
182. J. Bhattacharya and A. Van der Ven, *Physical Review B*, 2010, **81**, 104304.
183. G. Hautier, A. Jain, S. P. Ong, B. Kang, C. Moore, R. Doe and G. Ceder, *Chemistry of Materials*, 2011, **23**, 3495-3508.
184. G. Hautier, A. Jain, T. Mueller, C. Moore, S. P. Ong and G. Ceder, *Chemistry of Materials*, 2013, **25**, 2064-2074.
185. R. Zhang, X. Yu, K.-W. Nam, C. Ling, T. S. Arthur, W. Song, A. M. Knapp, S. N. Ehrlich, X.-Q. Yang and M. Matsui, *Electrochemistry Communications*, 2012, **23**, 110-113.
186. W. Song, T. S. Arthur, C. Bucur, M. Matsui, J. Muldoon, N. Singh and R. Zhang, *Journal*, 2012.
187. J. K. Burdett, G. D. Price and S. L. Price, *Journal of the American Chemical Society*, 1982, **104**, 92-95.
188. C. Kim, P. J. Phillips, B. Key, T. Yi, D. Nordlund, Y. S. Yu, R. D. Bayliss, S. D. Han, M. He and Z. Zhang, *Advanced materials*, 2015, **27**, 3377-3384.

189. P. Canepa, S. Jayaraman, L. Cheng, N. N. Rajput, W. D. Richards, G. S. Gautam, L. A. Curtiss, K. A. Persson and G. Ceder, *Energy & Environmental Science*, 2015, **8**, 3718-3730.
190. M. Liu, Z. Rong, R. Malik, P. Canepa, A. Jain, G. Ceder and K. A. Persson, *Energy & Environmental Science*, 2015, **8**, 964-974.
191. Y. Liang, R. Feng, S. Yang, H. Ma, J. Liang and J. Chen, *Advanced Materials*, 2011, **23**, 640-643.
192. Y. Liang, H. D. Yoo, Y. Li, J. Shuai, H. A. Calderon, F. C. Robles Hernandez, L. C. Grabow and Y. Yao, *Nano letters*, 2015, **15**, 2194-2202.
193. Z.-L. Tao, L.-N. Xu, X.-L. Gou, J. Chen and H.-T. Yuan, *Chemical communications*, 2004, 2080-2081.
194. M. Thackeray, L. De Picciotto, A. De Kock, P. Johnson, V. Nicholas and K. Adendorff, *Journal of power sources*, 1987, **21**, 1-8.
195. S. Okamoto, T. Ichitsubo, T. Kawaguchi, Y. Kumagai, F. Oba, S. Yagi, K. Shimokawa, N. Goto and E. Matsubara, *Advanced Science*, 2015, **2**.
196. M. Thackeray, A. De Kock, M. Rossouw, D. Liles, R. Bittihn and D. Hoge, *Journal of The Electrochemical Society*, 1992, **139**, 363-366.
197. J. C. Kim, X. Li, C. J. Moore, S.-H. Bo, P. G. Khalifah, C. P. Grey and G. Ceder, *Chemistry of Materials*, 2014, **26**, 4200-4206.
198. L. Pauling, *Journal of the american chemical society*, 1929, **51**, 1010-1026.
199. I. Brown, *Acta Crystallographica Section B: Structural Science*, 1988, **44**, 545-553.
200. F. Beck and P. Rüetschi, *Electrochimica Acta*, 2000, **45**, 2467-2482.
201. R. Malik, D. Burch, M. Bazant and G. Ceder, *Nano letters*, 2010, **10**, 4123-4127.
202. H. Gwon, S.-W. Kim, Y.-U. Park, J. Hong, G. Ceder, S. Jeon and K. Kang, *Inorganic chemistry*, 2014, **53**, 8083-8087.
203. J. Wu, G. Gao, G. Wu, B. Liu, H. Yang, X. Zhou and J. Wang, *RSC Advances*, 2014, **4**, 15014-15017.
204. R. Tressler, F. Hummel and V. Stubican, *Journal of the American Ceramic Society*, 1968, **51**, 648-651.
205. V. Bodenez, L. Dupont, L. Laffont, A. Armstrong, K. Shaju, P. G. Bruce and J.-M. Tarascon, *Journal of Materials Chemistry*, 2007, **17**, 3238-3247.
206. J. Carrasco, *The Journal of Physical Chemistry C*, 2014, **118**, 19599-19607.
207. B. Zhou, H. Shi, R. Cao, X. Zhang and Z. Jiang, *Physical Chemistry Chemical Physics*, 2014, **16**, 18578-18585.
208. W. Jost, *The Journal of Chemical Physics*, 1933, **1**, 466-475.
209. S. M. Fortier and B. J. Giletti, *Science*, 1989, **245**, 1481-1485.
210. S. Adams, *Solid State Ionics*, 2000, **136**, 1351-1361.
211. J. B. Brady and D. J. Cherniak, *Reviews in mineralogy and geochemistry*, 2010, **72**, 899-920.
212. D. Sheppard and G. Henkelman, *Journal of computational chemistry*, 2011, **32**, 1769-1771.
213. Y. Mo, S. P. Ong and G. Ceder, *Chemistry of Materials*, 2014, **26**, 5208-5214.
214. T. Song, H. Cheng, H. Choi, J.-H. Lee, H. Han, D. H. Lee, D. S. Yoo, M.-S. Kwon, J.-M. Choi and S. G. Doo, *Acs Nano*, 2011, **6**, 303-309.
215. K.-S. Park, P. Xiao, S.-Y. Kim, A. Dylla, Y.-M. Choi, G. Henkelman, K. J. Stevenson and J. B. Goodenough, *Chemistry of Materials*, 2012, **24**, 3212-3218.
216. D. A. Tompsett and M. S. Islam, *Chemistry of Materials*, 2013, **25**, 2515-2526.
217. G. Amatucci, F. Badway, A. Singhal, B. Beaudoin, G. Skandan, T. Bowmer, I. Plitz, N. Pereira, T. Chapman and R. Jaworski, *Journal of The Electrochemical Society*, 2001, **148**, A940-A950.
218. P. Novák, R. Imhof and O. Haas, *Electrochimica Acta*, 1999, **45**, 351-367.
219. G. Mills and W. Jacobsen, 1998.
220. M. Wenger and T. Armbruster, *European Journal of Mineralogy*, 1991, 387-400.
221. A. Navrotsky and O. Kleppa, *Journal of Inorganic and Nuclear Chemistry*, 1967, **29**, 2701-2714.
222. R. Malik, F. Zhou and G. Ceder, *Nature materials*, 2011, **10**, 587-590.

223. R. t. Shannon, *Acta crystallographica section A: crystal physics, diffraction, theoretical and general crystallography*, 1976, **32**, 751-767.
224. K. Kang, Y. S. Meng, J. Bréger, C. P. Grey and G. Ceder, *Science*, 2006, **311**, 977-980.
225. N. A. Chernova, M. Roppolo, A. C. Dillon and M. S. Whittingham, *Journal of Materials Chemistry*, 2009, **19**, 2526-2552.
226. Z. Popović, M. Konstantinović, R. Gajić, V. Popov, M. Isobe, Y. Ueda and V. Moshchalkov, *Physical Review B*, 2002, **65**, 184303.
227. E. Weinan, W. Ren and E. Vanden-Eijnden, *Physical Review B*, 2002, **66**, 052301.
228. E. Vanden-Eijnden and M. Heymann, *Journal*, 2008.
229. H.-C. Yu, C. Ling, J. Bhattacharya, J. C. Thomas, K. Thornton and A. Van der Ven, *Energy & Environmental Science*, 2014, **7**, 1760-1768.
230. J. Bhattacharya and A. Van der Ven, *Physical Review B*, 2011, **83**, 144302.
231. S. Åsbrink, A. Waškowska, L. Gerward, J. S. Olsen and E. Talik, *Physical Review B*, 1999, **60**, 12651.
232. C. Ling and F. Mizuno, *Chemistry of Materials*, 2013, **25**, 3062-3071.
233. K. Hoang and M. Johannes, *Chemistry of Materials*, 2011, **23**, 3003-3013.
234. R. Malik, A. Abdellahi and G. Ceder, *Journal of The Electrochemical Society*, 2013, **160**, A3179-A3197.
235. S. P. Ong, V. L. Chevrier and G. Ceder, *Physical Review B*, 2011, **83**, 075112.
236. G. S. Gautam, P. Canepa, R. Malik, M. Liu, K. Persson and G. Ceder, *Chemical Communications*, 2015, **51**, 13619-13622.
237. G. Sai Gautam, P. Canepa, A. Abdellahi, A. Urban, R. Malik and G. Ceder, *Chemistry of Materials*, 2015, **27**, 3733-3742.
238. C. Delmas, H. Cognac-Auradou, J. Cocciantelli, M. Menetrier and J. Doumerc, *Solid State Ionics*, 1994, **69**, 257-264.
239. S. P. Ong, S. Cholia, A. Jain, M. Brafman, D. Gunter, G. Ceder and K. A. Persson, *Computational Materials Science*, 2015, **97**, 209-215.
240. Y. Wang, W. D. Richards, S. P. Ong, L. J. Miara, J. C. Kim, Y. Mo and G. Ceder, *Nature materials*, 2015.
241. W. Sun, S. T. Dacek, S. P. Ong, G. Hautier, A. Jain, W. D. Richards, A. C. Gamst, K. A. Persson and G. Ceder, *Science Advances*, 2016, **2**, e1600225.
242. Z. Rong, D. Kitchaev, P. Canepa, W. Huang and G. Ceder, *The Journal of Chemical Physics*, 2016, **145**, 074112.
243. W. Kohn and L. J. Sham, *Physical review*, 1965, **140**, A1133.
244. G. Kresse and J. Furthmüller, *Computational Materials Science*, 1996, **6**, 15-50.
245. G. Kresse and J. Furthmüller, *Physical review B*, 1996, **54**, 11169.
246. A. Jain, S. P. Ong, W. Chen, B. Medasani, X. Qu, M. Kocher, M. Brafman, G. Petretto, G. M. Rignanese and G. Hautier, *Concurrency and Computation: Practice and Experience*, 2015, **27**, 5037-5059.
247. D. Morgan, G. Ceder and S. Curtarolo, *Measurement Science and Technology*, 2004, **16**, 296.
248. D. C. Hannah, G. S. Gautam, P. Canepa, Z. Rong and G. Ceder, *Chemical Communications*, 2017.
249. V. Thangadurai, S. Narayanan and D. Pinzaru, *Chemical Society Reviews*, 2014, **43**, 4714-4727.
250. R. Murugan, V. Thangadurai and W. Weppner, *Angewandte Chemie International Edition*, 2007, **46**, 7778-7781.
251. M. Liu, A. Jain, Z. Rong, X. Qu, P. Canepa, R. Malik, G. Ceder and K. A. Persson, *Energy & Environmental Science*, 2016, **9**, 3201-3209.
252. M. O'Keeffe, *Acta Crystallographica Section A: Crystal Physics, Diffraction, Theoretical and General Crystallography*, 1979, **35**, 772-775.
253. A. Urban, D.-H. Seo and G. Ceder, *npj Computational Materials*, 2016, **2**, 16002.

254. A. Jain, Y. Shin and K. A. Persson, *Nature Reviews Materials*, 2016, **1**, 15004.
255. M. Hidouri and M. Ben Amara, *Acta Crystallographica Section E: Structure Reports Online*, 2009, **65**, i66-i66.
256. V. Morozov, K. Pokholok, B. Lazoryak, A. Malakho, A. Lachgar, O. Lebedev and G. Van Tendeloo, *Journal of Solid State Chemistry*, 2003, **170**, 411-417.
257. A. Benabad, K. Bakhous, F. Cherkaoui and E. M. Holt, *Acta Crystallographica Section C: Crystal Structure Communications*, 2000, **56**, 1292-1293.
258. D. A. Kitchaev, H. Peng, Y. Liu, J. Sun, J. P. Perdew and G. Ceder, *Physical Review B*, 2016, **93**, 045132.
259. J. Heyd, G. E. Scuseria and M. Ernzerhof, *The Journal of Chemical Physics*, 2003, **118**, 8207-8215.
260. G. Ceder, *Mrs Bulletin*, 2010, **35**, 693-701.
261. A. Chatterjee and D. G. Vlachos, *Journal of computer-aided materials design*, 2007, **14**, 253-308.
262. G. Henkelman and H. Jónsson, *The Journal of Chemical Physics*, 2001, **115**, 9657-9666.
263. A. F. Voter and J. D. Doll, *The Journal of chemical physics*, 1984, **80**, 5832-5838.